University of Milano-Bicocca

Department of Physics "G. Occhialini"

PhD Program in Physics and Astronomy, 38th cycle

Astrophysics Curriculum

Characterisation of the electromagnetic emission and dynamical evolution of Massive Black Hole Binaries

---

Candidate:
Fabiola Cocchiararo

Registration Number:
800327

Tutor:
Prof. Davide Gerosa

Supervisor:
Prof. Alberto Sesana

Co-supervisors:
Dr.ssa Alessia Franchini
Dr. Alessandro Lupi

Coordinator of the PhD Board of Professors for the Physics Department:
Prof. Stefano Ragazzi

Academic Year 2024/2025

UNIVERSITY OF MILANO-BICOCCA

Summary

Department of Physics "G. Occhialini"

PhD program in Physics and Astronomy

Characterisation of the electromagnetic emission and dynamical evolution of Massive Black Hole Binaries

by Fabiola Cocchiararo

Observational evidence has confirmed the presence of a massive black hole at the centre of most galaxies. Massive black holes (MBH) are compact objects with mass between $10^6\,\mathrm{M}_\odot$ and $10^{10}\,\mathrm{M}_\odot$. During their evolution, galaxies can merge and their respective black holes can bond in a massive black hole binary (MBHB). The stages through which the binary can efficiently shrink and coalesce are currently under debate. As a result of the interaction with the gaseous environment in which they reside, MBHBs are expected to produce distinctive observational electromagnetic (EM) signatures. Although known candidates at sub-parsec separation have been proposed based on their EM emission, convincing evidence that these sources are indeed MBHBs is still missing.

MBHBs are among the main targets of current and future gravitational wave (GW) experiments. The upcoming space-based Laser Interferometer Space Antenna will probe the milli-hertz GW band, observing the late inspiral and merger of MBHBs with masses between $10^4 - 10^7\,M_\odot$, across the Universe. At lower frequencies, in the nano-hertz regime, Pulsar Timing Arrays (PTAs) experiments can detect GWs from more massive MBHBs at milli-parsec separations. Although GWs are essential for a definitive detection of MBHBs, identifying unique EM counterparts is crucial for constraining the properties of these systems, opening the era of low-frequency multi-messenger astronomy. The importance of understanding the EM emission of

MBHBs has become even more compelling following the recent detections of a signal compatible with a GW background (GWB) reported by all the PTA collaborations across the globe, possibly hinting at the presence of a MBHB population.

In this thesis, we investigate the dynamics, the spectral and time variability of accreting MBHBs at milli-parsec separations, focusing on the interplay between the binary and its gaseous circumbinary disc. We present the first synthetic spectral energy distributions (SEDs) and Light Curves (LCs) from 3D hyper-Lagrangian hydrodynamical simulations of MBHBs surrounded by circumbinary discs. Using the 3D code GIZMO in its meshless finite mass version, we simulate live milli-parsec binaries with total mass $10^6\,\mathrm{M}_\odot$, exploring different mass ratios and eccentricities. We let these binaries evolve within a circumbinary disc described by an adiabatic equation of state, including the disc self-gravity and assuming gas cooling to occur via black body radiation.

We find significant variability of the SED, especially at high energies, which translates into LCs displaying distinctive modulations of a factor of ≈ 2 in the optical and of ≈ 10 in UV and X-rays. We analyse in detail the flux variability in the optical bands that will be probed by the Vera Rubin Observatory. When considering the Rubin Observatory flux limit and nominal survey duration, we find that equal-mass, circular binaries are unlikely to be identified, due to the lack of prominent peaks in their Fourier spectra. Conversely, unequal-mass and/or eccentric binaries can be singled out up to $z \approx 0.5$.

A critical aspect that has often been neglected in previous studies is the role of radiation pressure in the hydrodynamics evolution of the circumbinary disc. At sub-parsec scales, discs around MBHBs are likely dominated by radiation pressure; therefore, including this additional term in the hydrodynamics equations is very important in order to advance the theoretical modelling of the MBHB-disc interaction. We implement the contribution of the radiation pressure in our 3D numerical simulations, in order to evaluate its impact on both the evolution of the binary and its circumbinary disc and the EM signatures. We find that the radiation pressure significantly alters the vertical and thermal structure of the disc, resulting in a geometrically thinner, therefore colder configuration. This leads to a reduced accretion rate onto the binary and suppresses cavity eccentricity growth and precession in circular equal mass binaries.

The emission from the mini-discs shifts from the optical towards UV frequencies and with a peak luminosity orders of magnitude higher, while the circumbinary disc becomes colder and dimmer as a result of its geometrically thinner configuration. Temporal variability is affected as well: near UV and soft-X ray fluxes are higher and more variable. Crucially, radiation pressure suppresses the characteristic "lump" formation in equal-mass circular systems, while a lump is formed for higher eccentricities without imprinting any modulation on the flux.

This thesis is organised as follows. Chapter 1 introduces the dynamics of massive black hole binaries, covering all the main steps of the binary formation, evolution and coalesce. We also report the current and future methods for detect these systems through both the gravitational wave and the electromagnetic channels. Chapter 2 describes the physical setup we adopt in this work. We here describe the properties of circumbinary discs, including the emission model we use to produce the SEDs and the LCs. Chapter 3 focuses on the simulations framework, reviewing the different numerical techniques commonly adopted to study MBHBs, comparing previous results on binary-disc interactions and EM signatures. We discuss the numerical setup, disc physics, parameter space explored, the implementation of radiation pressure and other details of our simulations. In Chapter 4 we present the expected SEDs and LCs obtained from our 3D simulations. In Chapter 5 we explore how radiation pressure affects the binary dynamics and the circumbinary disc evolution. In Chapter 6 we investigate how radiation pressure modifies the electromagnetic emission and the resulting observational signatures of these systems. Finally, the final chapter presents a discussion of the main results of this thesis and prospectives for future work.

Contents

Summary iii

I Introduction 1

1 Introduction 3

1.1 Dynamics of massive black hole binaries . . . 3

1.1.1 Dynamical friction . . . 4

1.1.2 Stellar and gas hardening . . . 7

Stellar hardening . . . 7

Gas hardening . . . 9

1.1.3 GWs emission . . . 11

1.2 Detection of massive black hole binaries signatures . . . 13

1.2.1 Gravitational waves channel . . . 13

1.2.2 Electromagnetic channel . . . 16

Binary candidates . . . 17

II Physical setup 21

2 Physical setup 23

2.1 Accretion Disc . . . 23

2.1.1 Viscosity and turbulent transport . . . 28

2.1.2 Gravitational stability and self-regulation . . . 30

2.1.3 Emission: Spectral Energy Distribution and Light Curve . . . 33

Non-thermal emission . . . 37

III Simulations framework **39**

3 Simulations framework **41**

3.1 Numerical techniques . . . 42

3.2 Overview of previous MBHBs simulations . . . 43

3.2.1 Binary-disc interaction and orbital evolution . . . 43

3.2.2 Periodic modulations of EM emission . . . 46

3.3 Methodology adopted in this work . . . 47

3.3.1 Numerical setup and initial conditions . . . 47

3.3.2 Disc physics . . . 47

3.3.3 Parameters space . . . 48

3.3.4 Thermal and non-thermal emission model . . . 49

3.3.5 Implementation of radiation pressure in GIZMO . . . 51

IV Results **53**

4 Electromagnetic signatures from accreting massive black hole binaries in time domain photometric surveys **55**

4.1 Disc and binary evolution . . . 56

4.2 Analysis of the electromagnetic counterparts . . . 59

4.2.1 Spectral energy distributions . . . 59

4.2.2 Light Curves . . . 64

4.2.3 Periodicity identification in the Vera Rubin Observatory survey 67

4.3 Summary of the main results . . . 70

5 The role of radiation pressure in accreting massive black hole binaries **75**

5.1 Disc evolution . . . 76

5.2 Binary evolution . . . 80

5.3 Interplay between disc shape and binary preferential accretion . . . 85

5.4 Summary of the main results . . . 92

6 Suppressed "lump" EM signature in radiation pressure dominated accreting massive black hole binaries **95**

6.1 Spectral energy distributions . . . 97

6.2 Light curves . . . 102

6.3 Periodic signal identification in Rubin Observatory survey 106
6.4 Summary of the main results 110

Conclusions **113**

Bibliography **124**

Somewhere, something incredible
is waiting to be known.
- Carl Sagan

Part I

Introduction

Chapter 1

Introduction

1.1 Dynamics of massive black hole binaries

Massive black holes (MBHs) are astronomical objects whose existence is predicted by the theory of General Relativity. They are characterised by an intense gravitational field and defined by an event horizon, i.e., a spherical surface which defines the region of spacetime that can not communicate with the external universe [1]. Observations provide compelling evidence that most galaxies host a massive black hole at their centre, with masses between $10^6 M_\odot$ and $10^{10} M_\odot$ [2]. Within the hierarchical model of structure formation [3, 4], galaxies can grow via accretion of gas from the intergalactic medium and mergers with other galaxies. The fate of MBHs following galaxy mergers was first described by [5], where the authors identified three stages of the evolution of the system. When two galaxies merge, their respective massive black holes are expected to migrate toward the centre, owing to *dynamical friction*, a drag force acting on each black holes moving through a background of stars and gas [6]. If dynamical friction is efficient, the two MBHs form a gravitationally bound binary, i.e. they reach a separation of the order of 1 parsec. This newly formed binary can further evolve via *stellar and gas hardening*: the interaction with stars within a nuclear star cluster (NCS) and a gaseous circumbinary disc continues to remove energy and angular momentum from the bound binary, causing its separation to decrease over time. The stellar hardening process is similar to the dynamical friction against stars but on smaller scales, i.e. the bound binary interacts with small masses that pass in its very vicinity instead of experiencing weak interactions with stars that are distant as in the case of dynamical friction. The binary can then exchange angular momentum with a gaseous disc through resonances and this process is commonly

referred to as gas-hardening. Eventually, when the separation becomes small enough, *gravitational wave emission* takes over, driving the two black holes to coalescence and forming a more massive MBH. These three different phases of the binary evolution are discussed in detail in the following paragraphs.

1.1.1 Dynamical friction

Early stages of massive black hole pairing have been observed during galaxy mergers [e.g., 7, 8] At this time, the systems is formed by two separate but gravitationally bound galaxies, that can be identified at separations of approximately 100 kpc [9, 10] As the merger progresses and the galaxies coalesce, dynamical friction acting on both stars and gas causes the MBHs to gradually move toward the centre of the forming remnant galaxy. During this process, the separation between the two MBHs decreases from tens of kpc down to a few kpc. This initial stage is governed by the *dynamical friction* [6]. As each black hole moves through the stellar background, it gravitationally interacts and perturbs the surrounding stars. In particular, each star with mass m moving in the potential of the MBH with velocity $v_{\rm m}$, exerts a drag on it, extracting energy and angular momentum from the system. As a consequence of the interaction with stars, the MBH velocity changes as:

$$\frac{d\vec{V}_{\rm M}}{dt} = -16\pi^2 \log\Lambda m G^2 (M+m) \frac{\vec{V}_{\rm M}}{V_{\rm M}^3} \int_0^{V_{\rm M}} f(v_m) v_m^2 dv_m \tag{1.1}$$

where M is the mass of the single black hole (i.e., M_1 or M_2), $f(v_{\rm m})$ is the interacting stellar velocity distribution function, Λ is the ratio between the maximum impact parameter $b_{\rm max}$ (a typical value of $b_{\rm max}$ is the dimension of stellar bulge ~ 10 kpc) and minimum impact parameter $b_{\rm min}$ for which the star experiences a 90° deflection with respect to the initial direction. We can define the fraction of interacting stars with velocity lower than MBH velocity $v_{\rm m} < V_{\rm M}$ as:

$$F(V_{\rm M}) = \frac{\int_0^{V_{\rm M}} f(v_{\rm m}) v_{\rm m}^2 dv_{\rm m}}{\int_0^{\infty} f(v) v^2 dv}. \tag{1.2}$$

If all the stars are isotropically distributed, the denominator is $n/4\pi$ and we can express the integral in Eq. 1.1 as:

$$\int_0^{V_{\rm M}} f(v_{\rm m}) v_{\rm m}^2 dv_{\rm m} = \frac{nF(V_{\rm M})}{4\pi} \tag{1.3}$$

If the MBH is assumed to move within an isothermal sphere, the stellar density profile can be related to the stars dispersion velocity σ and to the radial distance r:

$$\rho(r) = \frac{\sigma^2}{2\pi G r^2}. \tag{1.4}$$

In this configuration, the circular velocity $v_{\rm circ}$ is given by:

$$v_{\rm circ} = \sqrt{\frac{GM(r)}{r}} = \sqrt{\frac{G2\sigma^2 r}{Gr}} = \sqrt{2}\sigma. \tag{1.5}$$

Combining Eq. 1.1, 1.3, 1.4, and 1.5 is it possible to obtain the force acting on a MBH moving in a circular orbit as:

$$F = M\frac{d\vec{V_{\rm M}}}{dt} = -\frac{4\pi \log\Lambda G^2 M^2 \rho}{2\sigma^2} F(V_{\rm M}). \tag{1.6}$$

This force originates from dynamical friction and depends on the square of the MBH mass. As a result, the greater the mass of a black hole, the more effective the dynamical friction becomes in slowing it down.

The specific angular momentum of the MBH on an orbit of radius r and velocity v is given by $l = vr$. It varies over time according to:

$$\frac{dl}{dt} = \frac{dv}{dt}r + v\frac{dr}{dt}. \tag{1.7}$$

If the black hole is assumed to follow a circular orbit, its orbital velocity remains constant while the orbital radius gradually decreases over time. By combining Eq. 1.6 and Eq. 1.7 it is possible to determine the characteristic timescale $t_{\rm f}$ over which a massive object inspirals into the centre of the bulge:

$$t_{\rm f} = \frac{19\,{\rm Gyr}}{\log\Lambda}\left(\frac{r_{\rm i}}{5\,{\rm kpc}}\right)^2 \frac{\sigma}{200\,{\rm km\,s^{-1}}}\frac{10^8\,M_\odot}{M} \tag{1.8}$$

where r_i is the MBH initial position.

As dynamical friction efficiently brings the two MBHs towards the centre of the newly formed galaxy, the self-gravity of the two MBHs is no longer negligible and they can form a bound binary. This happens at separation given by:

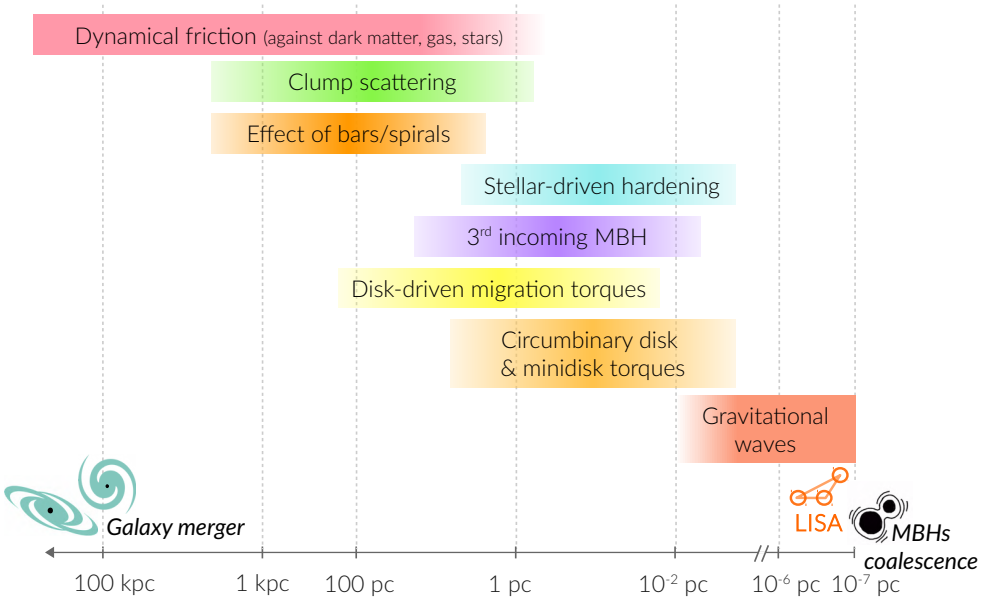

FIGURE 1.1: The picture shows a schematic overview of the main physical processes that occur during the evolution of the binary and the typical spatial scales involved. Picture from [11].

$$a_{\rm B} \sim \frac{GM_{\rm B}}{2\sigma} \sim 0.2 \left(\frac{M_{\rm B}}{10^6_{\odot}}\right) \left(\frac{\sigma}{100\,{\rm km\,s^{-1}}}\right)^{-2} {\rm pc} \tag{1.9}$$

with σ the velocity dispersion of the host galaxy, $M_{\rm B} = M_1 + M_2$ the total mass of the binary, and M_1 and M_2 are the mass of the primary and secondary black hole, respectively.

However, at these scales dynamical friction becomes inefficient and the binary continues to evolve through interactions with the surrounding stars and gas.

In gas-rich mergers, the dynamical friction experienced by the two black holes is not only due to the stellar environment, but also to the large amount of cold gas driven toward the remnant galaxy. Numerical simulations have shown that, during the advanced stages of the merger, the MBHs can become embedded in a dense, rotationally supported circumnuclear disc of gas. This structure is often the most massive and dense structure in the remnant nucleus [12–15] , providing a very efficient medium for MBHs orbital decay. In this scenario, the binary can form on relatively short timescales, $\lessapprox 10^6\,{\rm yr}$, reaching separation of $\sim 1\,{\rm pc}$. At this point, the mass of gas enclosed within the binary orbit becomes lower than the MBHB mass itself,

making the gaseous dynamical friction inefficient.

Gravitational waves (GWs) emission only becomes efficient at a separation of $a_{\rm GW} \sim 10^{-4} - 10^{-3}$ pc for equal mass binaries with total mass $M_{\rm B} \sim 10^6 - 10^7\, M_\odot$ [11]. Thus, both in the case of dense stellar and gas-rich environment, we need to invoke one or more astrophysical mechanisms to shrink the binary up to the point where GWs can efficiently drive the merger, as shown in Fig. 1.1. The most explored ones involve the interaction with either the stellar background or a gaseous circumbinary disc, which effects are discussed in the next section Sec. 1.1.2

1.1.2 Stellar and gas hardening

In the merger remnant, the newly formed MBHB can be once again surrounded by stars and gas. The main mechanisms through which the binary can lose angular momentum and energy are the *stellar hardening* and the *gas hardening*.

Stellar hardening

The presence of a nuclear star cluster (NSC) in the central regions of the merger remnant can facilitate the MBHB inspiral. The binding energy of the binary $E_{\rm b}$ on a Keplerian orbit is given by:

$$E_{\rm B} = -\frac{G\mu M_{\rm B}}{2a_{\rm B}}\,, \tag{1.10}$$

where $M_{\rm B} = M_1 + M_2$ is the total mass and $\mu = M_1 M_2 / M_{\rm B}$ is the reduced mass of the binary. Stars passing within a few times the binary separation can undergo a three-body interactions with the binary itself, through a process known as *gravitational slingshot*. During these encounters, stars are ejected at infinity with velocities comparable to the relative velocity of the two MBHs $v_{\rm ejec} \sim V_{\rm B,rel}$ [16]. Different three-body scattering experiments [17, 18] have shown that each ejected stars carries away energy and angular momentum from the binary and, as a consequence, the binary shrinks. The rate at which the semi-major axis of the binary decreases can be written as [19]:

$$\frac{da_{\rm B}}{dt} = -H\frac{G\rho}{\sigma}a_{\rm B}^2 \tag{1.11}$$

where H is the dimensionless hardening rate, which is approximately constant ($H \sim 15$) once the binary enters the hard regime. This regime occurs when $a_{\rm B} < GM_2/(4\sigma^2)$ and corresponds to the point at which the binary binding energy exceeds the typical kinetic energy of surrounding stars, making each stellar interaction highly effective at shrinking the binary. It is important to notice that, once the binary is in the hard regime, the hardening rate does not depend on the total mass and only very weakly on mass ratio and eccentricity, with H confined in the range 15-20. Eq. 1.11 is valid for a uniform stellar background of density ρ. However, [20] found that the equation can be applied to galactic nuclei by evaluating ρ at the radius of influence $r_{\rm inf}$, i.e., the region within the inclosed stellar mass is comparable to the binary mass, considering $\rho_{\rm inf}$. Similarly, the stellar velocity dispersion σ is constant throughout the bulge, but for more general stellar density profiles, σ varies with radius, and it is taken at $r_{\rm inf}$, $\sigma(r_{\rm inf}) = \sigma_{\rm inf}$. Since in Eq. 1.11 $da_{\rm B} \propto -a_{\rm B}^2$, the binary shrinks more slowly as its separation decreases, until gravitational waves emission eventually dominates.

By combining Eq. 1.10 and Eq. 1.11, it is possible to compute the rate at which the binary binding energy increases:

$$\frac{dE_b}{dt} = H\frac{G^2M^2\rho}{8\sigma}\,. \tag{1.12}$$

The mass of stars ejected during the hardening process is:

$$\frac{dm_*}{da_{\rm B}} = \frac{dm_*}{dt}\frac{dt}{da_{\rm B}} = m\frac{dN}{dt}\frac{dt}{da_{\rm B}} = \frac{2\pi}{H}\frac{M_{\rm B}}{a_{\rm B}}\,, \tag{1.13}$$

and the mass expelled per logarithmic interval of semi-major axis is:

$$\frac{dm_*}{d\log(a_{\rm B})} = \frac{2\pi}{H}M_{\rm B} = JM_{\rm B}\,, \tag{1.14}$$

where J is the mass ejection rate and, according to numerical simulations (for example [21]), its value is ~ 0.5, meaning that approximately half of the binary mass is expelled as stars during the hardening phase. Integrating over the change in semi-major axis from the beginning to the end of the hardening phase, the total mass of ejected stars is:

$$\Delta m_* = \frac{2\pi}{H} M_{\rm B} \int_{a_{\rm B,i}}^{a_{\rm B,f}} d\log(a_{\rm B}) = \frac{2\pi}{H} M_{\rm B} \log\left(\frac{a_{\rm B,i}}{a_{\rm B,f}}\right) , \tag{1.15}$$

where $a_{\rm B,i}$ and $a_{\rm B,f}$ are the semi-major axis at the beginning and end of the hardening phase, respectively. This result, physically, quantifies the total "stellar mass budget" carried out during the hardening phase, which is crucial for driving the binary to coalesce. However, this simple treatment does not take into consideration the loss cone depletion: only a small fraction of stars can interact with the MBHB and, once ejected, the loss cone is depleted. Thus, binary evolution depends on the rate at which new stars enter the loss cone. In typical spherical stellar systems, the mass in stars within the binary loss cone is not sufficient to lead the binary to reach the GWs emission phase, originating the so called *'last parsec problem'*. However, in more realistic scenarios, the triaxial and rotating nature of the stellar distribution promotes efficient loss cone refilling, allowing the binary to coalesce on a time scale of $\sim 10^8$ yr [22].

Beyond the stellar mass budget, the orbital eccentricity of the binary also plays an important role. Scattering experiments and simulations [17, 19] show that while the nearly circular, equal mass binaries tend to remain fairly circular, unequal-mass or eccentric systems can become very eccentric (i.e., $e_{\rm B} \sim 0.9$). Since highly eccentric binaries emit gravitational waves more efficiently, the eccentricity growth is crucial to transit to the coalescence phase more rapidly [23, 24].

Gas hardening

In gas-rich galactic nuclei, mergers drive significant inflows of cold gas toward the centre of the remnant galaxy. Eventually, this gas can accumulate on sub-parsec scales, forming a gaseous circumbinary disc around the MBHB, which becomes the main driver of orbital evolution. Since the binary is rotating, it has a strong quadrupole moment that torques the gas of the disc. As a consequence, it carves out a low-density cavity of size $\sim 2a_{\rm B}(1 - e_{\rm B})$ with $e_{\rm B}$ the binary eccentricity, forming a *gap* (or a *cavity*) [25].

The transfer of angular momentum from the binary to the gas causes the binary to shrink. This exchange occurs through gas streams that enter the central cavity and feed the two black holes at a rate $\dot{m} = dm/dt$, while they carry out angular

momentum from the system. The angular momentum of a gas element with mass m at the cavity edge $r_{\rm gap}$ is $L = mvr = m\sqrt{GM_B r_{\rm gap}}$. Thus, the angular momentum carried away by the inflowing gas changes at a rate:

$$\frac{dL}{dt} = -\dot{m}\sqrt{GMr_{gap}}\,. \tag{1.16}$$

For simplicity, assuming a circular binary orbit with angular momentum equal to $L_{\rm B} = \mu\sqrt{GMa_{\rm B}}$, the angular momentum change rate is given by:

$$\frac{dL_{\rm B}}{dt} = \mu\sqrt{GM_{\rm B}}\frac{1}{2\sqrt{a_{\rm B}}}\frac{da_{\rm B}}{dt}\,. \tag{1.17}$$

Since the angular momentum gained by the gas must be equal to the amount lost by the binary, by comparing Eq.1.16 and Eq.1.17 we can obtain the rate at which the binary shrinks thanks to the interaction with the gaseous circumbinary disc as:

$$\frac{da}{dt} = -2\sqrt{2}\frac{\dot{m}}{M}\frac{(1+q)^2}{q} \tag{1.18}$$

where $q = M_2/M_1$ is the binary mass ratio. This relation can be used to find the characteristic gas-hardening timescale:

$$\frac{dt}{d\log a_{\rm B}} \simeq \frac{M}{\dot{m}}\frac{1}{2\sqrt{2}}\frac{q}{(q+1)^2}\,. \tag{1.19}$$

If the accretion rate is approximated by the Eddington value:

$$\dot{m} \simeq \frac{L_{\rm edd}}{\epsilon c^2} \tag{1.20}$$

$$L_{\rm Edd} = \frac{4\pi G M_{\rm B} m_{\rm p} c}{\sigma_{\rm T}} \propto M_{\rm B} \tag{1.21}$$

then 1.19 becomes independent of the mass of the binary and yields a nearly constant value of order $\sim 10^7$ yr.

However, this treatment provides only a zero-order estimate. In reality, the interaction between the binary and its circumbinary disc is far more complex. The binary does not simply transfer angular momentum uniformly; rather, the quadrupolar nature of its gravitational potential generates discrete gas streams that enter the cavity and

are flung back to the edge of the disc. These ballistic streams mediate the angular momentum exchange in a way that is neither uniform nor trivial to predict a priori. As a result, these equations capture a general idea of what happens during the hardening phase, the actual evolution of the semi-major axis of the binary can depend on the structure, thermodynamics and viscosity of the disc. For these reasons, to have a more accurate understanding of what happens during this phase of the binary evolution, numerical simulations are required.

The transfer of angular momentum from the binary to the disc is not uniform: the binary interacts with the circumbinary disc at discrete resonant locations, where the orbital frequencies of the binary and the disc satisfy an integer or rational ratio [25–28]. These resonances are characterised by a pair of integers (m, l) and can be classified into the co-rotation and Lindblad resonances, located at $R_{\rm C} = (m/l)^{(2/3)} a_{\rm B}$ and $R_{\rm L} = ((m \pm 1)/l)^{(2/3)} a_{\rm B}$, respectively. The $\pm$ sign correspond to the outer and inner Lindblad resonances, respectively. These resonances arise because the gravitational potential of the rotating binary periodically perturbs the disc. Gas elements at these resonant locations experiences torques that can either extract or add angular momentum from the binary. Indeed, the exact effect of the gaseous disc on the orbital evolution of the binary remains an active area of research and debate. Recent hydrodynamical simulations have shown that the binary may shrink or expand, depending on the properties of the circumbinary disc [29–38]. However, high-resolution 3D simulations have found that the dominant outcome is generally a decrease of the binary semi-major axis. In particular, while relative warm discs with aspect ratio around ~ 0.1 can promote an expansion, colder and less viscous circumbinary discs tend to drive efficient semi-major axis decrease. This complex interplay between the binary and the circumbinary disc has been investigated in the context of this thesis. In Section 3.2, we discuss how different numerical and physical setups can lead different outcomes in simulations, while in Chapter 4 and Chpter 5 we present and discuss the results obtained from our own simulations.

1.1.3 GWs emission

The final phase of massive black hole binaries evolution is driven by gravitational waves. GWs are perturbations of space-time that carry energy and angular momentum away from the system, allowing the binary to coalesce into a single MBH. During this last phase, the evolution of the orbit is described by [39]:

$$\frac{da_{\rm B}}{dt} = -\frac{64}{5}\frac{G^3}{c^5}\frac{M_1 M_2 (M_1+M_2)}{a_{\rm B}^3} F(e_{\rm B})\,, \tag{1.22}$$

where the function $F(e_{\rm B})$ encodes the dependence of the binary eccentricity e:

$$F(e_{\rm B}) = (1-e^2)^{-7/2}\left(1+\frac{73}{24}e^2+\frac{37}{96}e^4\right)\,. \tag{1.23}$$

The orbital evolution also involves the energy emission given by

$$\frac{dE_{\rm B}}{dt} = -\frac{32}{5}\frac{G^4}{c^5}\frac{M_1 M_2 (M_1+M_2)}{a_{\rm B}^5} F(e_{\rm B})\,, \tag{1.24}$$

and the loss of angular momentum at rate:

$$\frac{dL_{\rm B}}{dt} = -\frac{32}{5}\frac{G^{7/2}}{c^5}\frac{M_1^2 M_2^2 (M_1+M_2)^{1/2}}{a_{\rm B}^{7/2}} g(e_{\rm B})\,, \tag{1.25}$$

with $g(e_{\rm B})$ defined as:

$$g(e_{\rm B}) = (1-e^2)^{-2}\left(1+\frac{7}{8}e^2\right)\,. \tag{1.26}$$

For circular orbits $e = 0$, by comparing Eq. 1.24 and Eq. 1.25 we can see that the only difference between the two is $\Omega_{\rm B}$, thus $\dot{E} = \Omega\dot{L}$. Since in the Newtonian limit the orbital energy and angular momentum are related by $E_{\rm B} = \Omega L_{\rm B}$, this proportionality is preserved as the system loses energy and angular momentum to gravity waves. This means that circular binaries remain circular during their inspiral phase. However, for eccentric binaries, the rate at which the eccentricity evoles is given by:

$$\frac{de}{dt} = -\frac{304}{15}\frac{G^3 M_1 M_2 (M_1+M_2)}{c^5 a^4}\frac{e}{(1-e^2)^{5/2}}\left(1+\frac{121}{304}e^2\right)\,. \tag{1.27}$$

Since in Eq. 1.27 there is a minus in front of only positive terms, it means that eccentric binaries, emitting GWs, tend to circularise over time.

The binary eccentricity plays a crucial role during this phase. Higher eccentricity significantly enhances the emission of GWs, accelerating the semi-major axis decrease and reducing the coalescence timescale $t_{\rm c}$:

$$t_{\rm c} = 0.25\,{\rm Gyr}\left(\frac{M_1 M_2 (M_1+M_2)^{-1}}{10^{8.3} M_\odot}\right)\left(\frac{a_{\rm B}}{1\,{\rm mpc}}\right)^4 F(e_{\rm B})^{-1}. \tag{1.28}$$

Moreover, the eccentricity induces multiple harmonics in the GW signal, providing a direct observational signature of the inspiral of the binary.

In conclusion, the dynamical evolution of a MBHBs is given by a sequence of distinct and interconnected phases. The efficiency of each phase depends on the properties of the host galaxy, the surrounding stellar and gaseous environments, and the orbital properties of the binary. Understanding these processes in detail is crucial not only for detecting gravitational wave signals but also for interpreting observation counterparts of galaxy nuclei. In the following section, we discuss the detection of massive black hole binaries signatures.

1.2 Detection of massive black hole binaries signatures

1.2.1 Gravitational waves channel

The existence of GWs is predicted by general relativity [40] and GWs were observed for the first time in 2015 by the Laser Interferometer Gravitational-Wave Observatory (LIGO) and Virgo interferometers [41]. To date, numerous additional detections have followed. Notably, in 2017, the GW signal of an inspiralling neutron star binary was detected and, for the first time, associated with an EM transient: a short γ-ray burst recorded by Fermi-GBM only 1.7 seconds after the coalescence [42]. In the following weeks, observations across the entire EM spectrum confirmed the multi-messenger nature of this detection. Very recently, on 23 November 2023, the two LIGO observatories both detected GW231123, a GW signal consistent with the merger of two black holes with masses $\sim 137\,M_\odot$ and$\sim 101 M_\odot$, being the most massive black hole collision ever detected.

Ground-based interferometers currently in operations, including LIGO Livingston (USA), LIGO Hanford (USA), Virgo (Italy), and KAGRA (Japan) are based on the Michelson interferometer configuration. In this setup, a monochromatic light beam is split by a beam splitter into two components travelling along perpendicular arms, each with a length of a few kilometres. At the end of each arm there is a mirror that

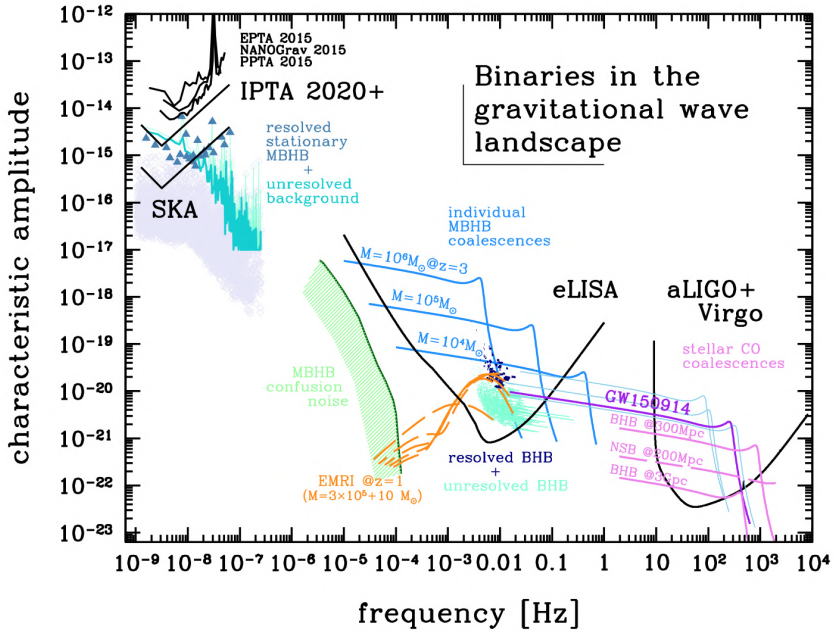

FIGURE 1.2: Sensitivity curves for PTA, eLISA, and LIGO/Virgo. Reproduced from [43]. Courtesy of A. Sesana.

reflects the beams back toward the splitter, where they are recombined. As space-time perturbations caused by a GW passage slightly alter the arm lengths and the light travels different distances in the two arm, producing a shift in the relative phases of the laser beams when they recombine at the beam splitter. This shift in the phase modifies the interference pattern of the output beam, probing a measurable signal that indicates a possible passage of a GW. For instance, LIGO interferometers have 4 km long arms and they measure differential displacements of $\Delta L(t) = \delta L_{\rm x} - \delta L_{\rm y} = h(t)L$, where $h(t)$ denotes the GW strain amplitude [41]. For a typical stellar-mass binary of $M_{\rm B} \sim 10\,M_{\odot}$ at a distance of $d \sim 1\,$Mpc, the expected strain amplitude is of the order $h \sim 10^{-22}$.

The final inspiral phase of a binary system ends when the binary has evolved to the Innermost Stable Circular Orbit (ISCO). The GW emission frequency at $R_{\rm ISCO} = 6GM_{\rm B}/c^2$ is given by:

$$f_{\rm ISCO} = \frac{1}{\pi}\sqrt{\frac{GM_{\rm B}}{R_{\rm ISCO}^3}} \propto \frac{1}{M_{\rm B}}\,, \tag{1.29}$$

which implies that more massive systems emit at lower GW frequencies. Therefore, to detect GWs from a binary system composed by massive BHs interferometers with longer arms are required, capable of detecting wave signals with a lower frequency and a longer wavelength. The future space-based Laser Interferometer Space Antenna

(LISA), scheduled for launch around 2034 by the European Space Agency, will be able to probe GWs in the 0.1 mHz $-$ 1 Hz frequency band [11, 44] emitted by systems with masses in the range $M \sim 10^4 - 10^8\,\mathrm{M}_\odot$. LISA will consist of three spacecrafts, forming an equilateral triangle with arm lengths of 2.5 million km, which will effectively operate as two Michelson interferometers rotated by 45°. GWs emitted by more massive systems ($M_\mathrm{B} \gtrsim 10^8\,M_\odot$) will be detected by Pulsar Timing Arrays (PTAs) [45]. PTAs exploit the extraordinary regularity of millisecond pulsars, which act as highly stable cosmic clocks. Pulsars are rapidly spinning neutron stars with rotation periods as short as a few milliseconds and strong magnetic fields of order 10^{12} G. The presence of such magnetic fields collimates a beam of high-energy particles which is emitted from the magnetic pole regions. In particular, the accelerated electrons produce curvature radiation that through complex physical interactions yet to be completely understood, cascades all the way to the radio wavelength, causing two beams of radio photons to be emitted from the magnetic poles. Since those are misaligned with the rotation axis of the pulsar, the net effect is that of a lighthouse. If one of the radio beams intercept the line of sight to the Earth during the rotation, we receive very regular radio pulses separated by the period of rotation period of the pulsar. A retarded or anticipated signal from a pulsar can be associated to the passage of a GW crossing the pulsar-Earth line. Figure 1.2 shows the sensitivity curves of different GW detectors, including PTAs, LISA (and its earlier design eLISA), and ground-based interferometers.

MBHB binaries are expected to populate the frequency bands accessible to LISA and PTAs, making them primary targets for future multi-messenger astronomy. In this context, a detection of a signal compatible with a stochastic gravitational-wave background (GWB), has been reported by the European and Indian PTA [EPTA+InPTA, 46–51], the North American Nanohertz Observatory for Gravitational Waves PTA [NANOGrav, 52–56], Parkes PTA [PPTA, 57], Chinese PTA [CPTA 58] and MeerKAT PTA [MPTA, 59]. While the properties of the signal are broadly consistent with expectations from a cosmic population of MBHBs, its origin cannot yet be observationally established from the GW data alone. Identifying EM counterparts will therefore be crucial to confirm the nature of the GWB and to constrain the underlying binary population.

In the next decades, the next gravitational waves detectors, both ground and lunar

based will significantly expand the current observational window. The planned third generation ground-based Einstein Telescope [60] in Europe and Cosmic Explorer [61] in the United States will have a better sensitivity compared to current detectors, potentially allowing the observation of compact binary mergers up to redshift $z \sim 100$. Looking further ahead, lunar-based interferometers such as the Laser Interferometer Lunar Antenna [62] and the Lunar Gravitational-Wave Antenna [63] aim to make the best use of the unique geophysical environment of the Moon (e.g., the absence of seismic activity) to access the intermediate $0.1 - 10\,\mathrm{Hz}$ frequency band emitted by binaries with mass between $10^2 - 10^6\,M_\odot$, providing the most definite understanding of their link to the growth of supermassive black holes. These future telescopes will detect previously inaccessible sources, improving the multi-messenger studies of massive black hole binaries across cosmic history.

1.2.2 Electromagnetic channel

Electromagnetic signatures from accreting MBHBs can arise before, during, and after the merger. In this work, I focus on the late inspiral phase, when the binary separation is of order $\sim 10^{-4}\,\mathrm{pc}$ and the orbital period is $\sim 1\,\mathrm{yr}$. Figure 1.3 shows a schematic representation of the system before the merger: the binary is surrounded by a gaseous circumbinary disc, whose inner edge is truncated by the torque exerted by the binary, creating a cavity. Gas from the circumbinary disc accretes onto the binary through accretion streams, which feed the two binary components, and form a mini-disc around them. In unequal-mass systems, accretion is preferentially directed toward the secondary black hole as it orbits closer to the inner edge of the circumbinary disc [64].

Mini-discs are considered the main source of variability in MBHBs. Since each BH, periodically, passes near the inner edge of the cavity and accretes gas through the streams, mini-disc accretion is modulated over the orbital period of the binary. This results in a periodic enhancement of the accretion rate, which translates into characteristic luminosity fluctuations if the residence time of matter in the mini-discs is short compared to the modulation period [65, 66]. Moreover, the feeding mechanism can generate some shocks in the gas that are modulated on the same timescale, as these shocks are expected to arise when the inflow of material impacts the outer edge of the mini-discs, producing hard-X ray emission [45, 67]. Furthermore, the two mini-discs may exchange material, generating additional shocks over different timescales,

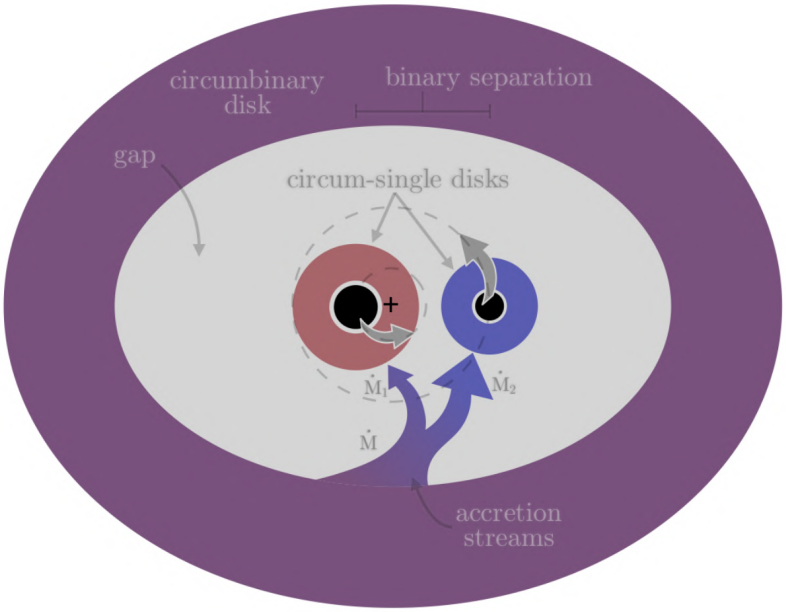

FIGURE 1.3: Simplified representation of a MBHB binary. The binary is surrounded by a circumbinary disc. Each BH is periodically fed by streams of gas which carry material from the circumbinary disc to the cavity, forming two mini-disc around each binary component. Reproduced from [82]. Courtesy of A. Sesana.

enhancing the local luminosity and introducing further periodic flux modulations [68]. As different numerical simulation show [36, 64, 68–74], part of the streams of gas that enters the cavity is flown back to the disc, creating shocks at the inner edge of the cavity wall that affect both the geometry and the emission of the disc. The disc aspect ratio H/R increases, and an over-density region forms at the cavity edge, orbiting with a period a few times longer than the binary orbital period, as reported in different numerical simulations [64, 65, 68, 71–79]. This region, called 'lump', represents one of the most promising electromagnetic signatures of MBHBs. It is expected to be stronger in equal-mass systems, with decreasing amplitude for lower mass ratios. At first, it was considered a feature of only circular binaries [74], but in Chapter 4 we discuss how it can be a potential smoking-gun signature of equal-mass systems. However, its persistence in realistic physical conditions is still under debate: radiation pressure has been shown to alter the disc structure and suppress the lump development, as shown in [80, 81] and further discussed in Chapter 5.

Binary candidates

The expected population of MBHBs can be related to the observed quasar population through analytic models of binary formation and evolution (e.g., [83–86]). In these

models, the fraction of quasars hosting a MBHB depends primarily on the binary residence time at a given orbital frequency and on the characteristic quasar lifetime. This relation can be expressed as

$$f_{\rm bin} \sim \eta_{\rm bin} \frac{\langle t_{\rm res} \rangle}{t_{\rm Q}} \tag{1.30}$$

where $\eta_{\rm bin}$ is the fraction of quasars triggered by galaxy mergers that eventually form a MBHB within the quasar lifetime $t_{\rm Q}$ and $t_{\rm res} \equiv f/\dot{f}$ is the residence time of a binary at orbital frequency f (i.e, the time that the binary spends at a given orbital period) [87]. For binaries whose orbital evolution is dominated by GW emission, the residence time decreases steeply with decreasing binary separation ($t_{\rm res} \propto a^4$). Thus, sub-parsec systems result to be intrinsically rare within the total AGN population. For instance, assuming circular binaries with total mass $M \sim 10^9\, M_\odot$, orbital period $P \sim 5\,{\rm yr}$ and typical quasar lifetimes $t_{\rm Q} \sim 10^8\,{\rm yr}$, the expected fraction of quasars hosting such binaries is

$$\frac{N_{\rm bin}}{N_{\rm Q}} \sim 10^{-3} \eta_{\rm bin} \tag{1.31}$$

indicating that fewer than 0.1% of quasars are expected to host sub-parsec binaries with orbital period of a few years [83]. Consequently, detecting a sample of ~ 100 MBHBs would require monitoring at least $> 10^5/\eta_{\rm bin}$ quasars over timescales comparable to orbital period of the binaries [84, 87].

Identifying accreting MBHBs requires observational signatures that distinguish them from individual MBHs. Binaries have remained undetected because it is hard to distinguish their behavior from the typical AGN. Indeed, as discussed in previous sections, the binary carves a cavity in the gaseous circumbinary disc and the accretion onto the binary is expected to produce periodic variability. Additionally, the formation of an over-density region at the edge of the cavity (the lump) can modulate the flow of accreted material, further enhancing period emission [e.g., as reported in 64, 78, 79, 88, 89]. Moreover, if the binary is inclined close to the line of sight, the light emitted by each mini-disc can be gravitational lensed by the companion one per orbit. This produces lensing-induced variations in the observed flux, such as periodic flares, providing unique signatures of a binary system. Finally, as a mini-disc moves toward or away the observer along the line of sight, its emission appears periodically brighter (and bluer) [90].

There are different but complementary methods to search for MBHBs. These include spectroscopic signatures (e.g., velocity shifts or double-peaked emission lines), photometric variability in time-domain surveys and periodicities in jet structure at radio or γ-ray frequency bands. For example, spectroscopic methods aim to detect how a binary system dynamically influence the surrounding gas. Spectroscopic searches for MBHBs rely on the assumption that a fraction of binaries at sub-parsec orbital separations reside in emission regions comparable in size to the broad line regions (BLRs) of single AGNs. Thus, the dynamical perturbation of a BLR by the binary gravitational potential can in principle be reflected in the low ionization broad emission-line profiles [e.g., 91–93], producing distinctive features in the low-ionisation broad emission lines, such as H$\alpha\,\lambda\,6563$, H$\beta\,\lambda\,4861$ and Mg II$\lambda\,2798$. In particular, the orbital motion of the binary can induce the Doppler shift of broad emission lines in the spectrum of a MBHB host. The spectral emission lines are assumed to be associated with the mini-disc that form around each binary component [94]. Moreover, in unequal-mass binaries, preferential accretion onto the secondary component may make it more luminous than the primary [25, 64, 70, 72], so that a fraction of MBHBs may appear as single-line spectroscopic binaries. This effect led to the discovery of MBHB candidates based on the criterion that the sources exhibit broad optical lines offset with respect to the rest frame of the host galaxy [e.g., 95–97]. Another potential signature arises when each binary component hosts its own BLR, producing a double-peaked broad emission lines. In this scenario, each peak corresponds to the Doppler shift emission from one of the BLRs, reflecting the orbital motion of the binary along the line of sight. Even though no MBHB sources have been definitely confirmed, several promising systems have been identified through their quasi-periodic variability in the observed flux. Systematic searches in time-domain surveys have revealed a number of candidates whose LCs show periodic modulation consistent with cavity-induced accretion, Doppler-boost effects and self-lensing flares [e.g., 98]. For instance, in the optical band, PG 1302-102 was the first candidate discovered in systematic searches and has been extensively followed up in the attempt to confirm its binary nature [99]. Other notable candidates include OJ 287, a blazar showing quasi-periodic outburst every $\sim$ 12 yr likely caused by an eccentric, unequal-mass binary [100] and SDSS J0159+0105, a candidate that exhibits two different periodicities consistent with the 2:1 ratio predicted by simulations ([101] and further simulation results are discussed in Chapter 4).

However, confirming true MBHBs among candidates is non trivial due to the presence of intrinsic variability in single MBHs, often referred to as 'red noise'. This stochastic variability can mimic quasi-periodic signals in LCs, making it difficult to distinguish genuine periodic emission from true MBHBs from just random fluctuations. Therefore, it is crucial to develop data analysis techniques able to distinguish true MBHBs emission from false positives. For instance, this kind of approach includes the use of Gaussian Processes, as demonstrated in [102]. Moreover, multi-wavelength observations can also provide complementary constraints. Finally, combining EM data with future GW observations from LISA and PTAs offers a promising approach to robustly identify MBHBs, as recently explored in [103].

Part II

Physical setup

Chapter 2

Physical setup

2.1 Accretion Disc

One of the properties of accretion discs is that they are often thin (i.e., $H/R \ll 1$). The thin-disc approximation results in a specific ordering of the velocities. It can be shown that requiring the disc to be geometrically thin corresponds to requiring the sound speed to be smaller than the rotational velocity, i.e. thin discs are very supersonic. Since the accretion process occurs on a long timescale and therefore the radial velocity v_{R} turns out to be smaller than both the sound speed c_{s} and the rotational speed v_ϕ. We therefore have the following ordering:

$$v_{\mathrm{R}} \ll c_{\mathrm{s}} \ll v_\phi \tag{2.1}$$

where v_ϕ is the rotational velocity component and c_s is the sound speed.

The dynamics of a fluid accretion disc can be understood through the fundamental conservation laws of fluid dynamics: the continuity equation and the Navier-Stokes equations. By assuming the thin disc approximation, the continuity equation for rotating and axisymmetric disc integrated in the vertical direction in cylindrical polar coordinates is given by:

$$\frac{\partial \Sigma}{\partial t} + \frac{1}{R}\frac{\partial}{\partial R}(R\Sigma v_{\mathrm{R}}) = 0 \tag{2.2}$$

where Σ is the disc surface density obtained integrating the 3D density ρ over the vertical extension of the disc $\Sigma = \int_{-z}^{z} \rho \mathrm{dz}$ and v_{R} is the radial velocity component.

Moreover, the Navier-Stokes momentum equation can be written as:

$$\rho\left[\frac{\partial \mathbf{v}}{\partial t} + (\mathbf{v}\cdot\nabla)\mathbf{v})\right] = -(\nabla P - \nabla\cdot\sigma) - \rho\nabla\Phi \tag{2.3}$$

where $P = P(R)$ is the pressure, $\rho = \rho(R)$ is the density, Φ is the gravitational potential. The first term on the right hand side describes the effect of viscous forces through the stress tensor σ, whose only non-zero component is the Rϕ one, where ϕ is the azimuthal angle, which determine the transport of angular momentum:

$$\sigma_{R\phi} = \eta R\frac{d\Omega}{dR} \tag{2.4}$$

where $\Omega = v_\phi/R$ is the angular velocity, v_ϕ the azimuthal velocity, and η is the shear viscosity coefficient. Moreover, for discs where self-gravity is relevant (i.e., the gravitational interaction between the gas particles cannot be neglected), it is possible to obtain the potential associated with the gas surface density Σ by solving the Poisson's equation. In case of geometrically thin-discs, the distribution of mass can be assumed to be confined to the midplane, leading to the simplified equation:

$$\nabla^2\Phi_{\rm sg} = 4\pi\Sigma\delta(z) \tag{2.5}$$

where $\Phi_{\rm sg}$ refers to the self-gravity gravitational potential and $\delta(z)$ is the Delta-function which specifies that the disc is confined to the midplane.

Equation 2.3 has a radial, vertical and azumuthal component.

Considering the *radial* component of equation Eq. 2.3, the first term on the left-hand side which is proportional to the radial velocity v_R, is negligible with respect to the second term which describes the centrifugal acceleration v_ϕ^2/R. On the right-hand side, the contribution from the viscous forces is negligible at first order and the pressure term can be obtained using the equation of state. The sound speed can be expressed as:

$$c_{\rm s}^2 = \frac{dP}{d\rho} \tag{2.6}$$

and thus the corresponding radial pressure gradient becomes:

$$\frac{1}{\rho}\frac{\partial P}{\partial R} = \frac{c_s^2}{\rho}\frac{\partial \rho}{\partial R} \sim \frac{c_s^2}{R}. \tag{2.7}$$

Given the velocity hierarchy reported in 2.1, also the term 2.7 is negligible compared to the centrifugal acceleration. Therefore, at the first order, the only term in the right hand side that can balance the centrifugal force is therefore gravity. Thus, the radial momentum balance reduces to:

$$\frac{v_\phi^2}{R} \simeq \frac{\partial \Phi}{\partial R}\,. \tag{2.8}$$

Both the central compact object and the accretion disc contribute to the total gravity field as follows:

$$\frac{\partial \Phi}{\partial R} = \frac{GM}{R^2} \tag{2.9}$$

$$\frac{\partial \Phi_{\rm disc}}{\partial R} = 2\pi G\Sigma \tag{2.10}$$

where M is the mass of the central object, G is the gravitational constant, and $\Phi_{\rm disc}$ is the gravitational potential of the disc. By comparing these two equations, the disc contribution is comparable with the central object one when $M_{\rm disc} \sim M$.

We here consider the *vertical* component of Eq. 2.3. Since the velocity in the vertical direction is very small, we can neglect the left-hand side of the equation. Thus, in the thin-disc approximation, Eq. 2.3 is reduced to two terms that describe how the gradient of vertical pressure is balanced by gravity through the 'hydrostatic equation':

$$\frac{1}{\rho}\frac{\partial P}{\partial z} = -\frac{\partial \Phi}{\partial z}. \tag{2.11}$$

For a non self-gravitating disc, where the gravitational potential is dominated by the central object, the vertical component of gravity can be approximated by:

$$-\frac{GMz}{r^3} \sim -\frac{GMz}{R^3} \tag{2.12}$$

where r is the spherical radius and the approximation is valid for small z. Thus, the hydrostatic equation Eq. 2.11 can be re-written:

$$\frac{c_s^2}{\rho}\frac{\partial \rho}{\partial z} = -\frac{GMz}{R^3}. \tag{2.13}$$

If the sound speed is constant along the z component, the vertical density profile turns out to be a Gaussian:

$$\rho(z) = \rho_0 \exp\left[-\frac{GMz^2}{2R^3 c_s^2}\right] = \rho_0 \exp\left[-\frac{z^2}{2H_{nsg}^2}\right] \tag{2.14}$$

where ρ_0 is the midplane density and H_{nsg} is the thickness of the non-self-gravitating disc, defined as $H_{nsg} = c_s/\Omega_K$, where $\Omega_K = \sqrt{GM/R^3}$ is the Keplerian angular velocity. The disc aspect ratio is then:

$$\frac{H_{nsg}}{R} = \frac{c_s}{v_K}. \tag{2.15}$$

In the self-gravitating case, where the gravity of the disc cannot be neglected and dominates compared to the gravity of the object at the centre, the right-hand-side of equation 2.13 has to be replaced with the force produced by a circular ring of gas with surface density Σ. Since our aim is to identify the effect of the disc self-gravity on the vertical structure, we can neglect the contribution of the central object and, if the slab is radially homogeneous we can write:

$$\frac{c_s^2}{\rho}\frac{\partial \rho}{\partial z} = -2\pi G\Sigma(z) \tag{2.16}$$

where $\Sigma(z) = \int_{-z}^{z} \rho(z')dz'$. In this case, the solution of the hydrostatic balance is more difficult to compute but it can be done analytically in the case of constant sound speed is constant, The solution is not Gaussian, but is given by:

$$\rho(z) = \rho_0 \frac{1}{\cosh^2(z/H_{sg})} \tag{2.17}$$

where H_{sg} is the thickness of the self-gravitating case, defined as $H_{sg} = \frac{c_s^2}{\pi G\Sigma}$.

Comparing the gravitational field contribution from the disc and from the central object along the vertical direction, we can notice that the disc self-gravity in reality

affects the disc vertical structure even when the disc mass is smaller than the central object mass:

$$\frac{M_{\rm disc}}{M} \approx \frac{H_{\rm nsg}}{R} \ll 1. \tag{2.18}$$

The condition above can also be re-written by comparing the two expression for the disc thickness defined above:

$$\frac{H_{\rm sg}}{H_{\rm nsg}} = \frac{c_s \Omega_K}{\pi G \Sigma}. \tag{2.19}$$

The two expressions become comparable when the right-hand factor reaches the value of 1, thus when $M_{\rm disc}/M \sim H_{\rm nsg}/R$.

Finally, in the *azimuthal* direction, viscosity plays a key role in the angular momentum distribution. Integrating the Navier-Stokes equations 2.3 in the vertical direction, it becomes:

$$\Sigma \left(\frac{\partial \mathbf{v}}{\partial t} + (\mathbf{v} \cdot \nabla)\mathbf{v} \right) = -(\nabla P - \nabla \cdot T) - \rho \nabla \Phi \tag{2.20}$$

where T is the vertical integral of the stress tensor reported in Eq. 2.4, whose only non-zero component is:

$$T_{R\phi} = \nu \Sigma R \frac{d\Omega}{dR}. \tag{2.21}$$

with $d\Omega/dR$ the 'differential rotation', due to the fact that disc elements at different radii rotate with distinct angular velocities and ν is the kinematic viscosity obtained from the vertical integral of the shear viscosity η:

$$\nu = \frac{1}{\Sigma} \int_{-\infty}^{\infty} \eta dz. \tag{2.22}$$

By considering both Eq. 2.2 and Eq. 2.20, it is possible to obtain the expression for the angular momentum conservation for a viscous disc as:

$$\frac{\partial}{\partial t}(\Sigma R v_\phi) + \frac{1}{R}\frac{\partial}{\partial R}(R v_{\rm R} \Sigma R v_\phi) = \frac{1}{R}\frac{\partial}{\partial R}\left(\nu \Sigma R^3 \frac{d\Omega}{dR} \right) \tag{2.23}$$

where the left-hand side represents the Lagrangian derivative of angular momentum per unit mass $\Sigma R v_\phi$, while the right-hand side is the torque from viscous stresses. By comparing this equation again with equation 2.3, it is possible to solve for the radial velocity inflow:

$$v_{\mathrm{R}} = \frac{1}{R\Sigma(R^2\Omega)'}\frac{\partial}{\partial R}(\nu\Sigma R^3\Omega') \tag{2.24}$$

where the symbol $'$ indicates the total derivative of a quantity with respect to the radius R. The radial velocity equation can be combined again with Eq. 2.3 to finally obtain the disc evolution equation:

$$\frac{\partial\Sigma}{\partial t} = -\frac{3}{R}\frac{\partial}{\partial R}\left[R^{1/2}\frac{\partial}{\partial R}(\nu\Sigma R^{1/2})\right]. \tag{2.25}$$

2.1.1 Viscosity and turbulent transport

In the evolution of accretion discs, viscosity plays a central role, as it governs the transport of angular momentum, allowing matter to inspiral while angular momentum is transferred outward. However, in order to properly understand how this transport occurs, it is necessary to examine the physical processes that can generate dissipation.

One possible mechanism in this respect is the standard collision between gas molecules, arising from the random thermal motion of particles, typically characterised by the sound speed c_{s}. Comparing the timescale for viscous transport due to collisions, t_ν, with the characteristic dynamical timescale $t_{\mathrm{dyn}} = \Omega^{-1}$, leads to:

$$\frac{t_\nu}{t_{\mathrm{dyn}}} = \frac{R^2\Omega}{\nu}. \tag{2.26}$$

This dimensionless ratio is commonly known as the 'Reynolds number' Re, which provides a measure of the flow regime: at low Re the fluid motion is laminar while at high Re turbulence becomes significant. The mean free path of gas molecules, λ, can be estimated as the inverse of the product of the number density n and the collisional cross-section σ_{coll}:

$$\lambda = \frac{1}{n\sigma_{\mathrm{coll}}} = \frac{\mu m_{\mathrm{p}}}{\rho\sigma_{\mathrm{coll}}} = \left(\frac{2\mu m_{\mathrm{p}}}{\Sigma\sigma_{\mathrm{coll}}}\right)H \tag{2.27}$$

where $m_{\rm p} = 1.67 \cdot 10^{-24}$g is the proton mass and μ is the average molecular weight. By substituting $\nu = \lambda c_{\rm s}$ in the Reynolds number equation Eq. 2.26 gives:

$$\frac{t_\nu}{t_{\rm dyn}} = \left(\frac{\Sigma\sigma_{\rm coll}}{2\mu m_{\rm p}}\right)\left(\frac{H}{R}\right)^{-2} . \tag{2.28}$$

For typical disc parameters (i.e. cross section of the order of the size of a hydrogen molecule $\sigma_{coll} \approx 10^{-16}\,{\rm cm}^2$, $\Sigma \simeq 10^5\,{\rm g/cm}^2$ and $H/R \simeq 0.01$), this ratio is very long, comparable to the Hubble time. As a consequence, we can conclude that collisions are not efficient enough to explain the angular momentum transport, and that the process responsible for the actual viscosity has to be different. Indeed, the high Reynolds number suggests that the flow in the accretion discs should be highly turbulent. In this regime, angular momentum is transferred through the mixing of fluid elements, a mechanism far more efficient than simple molecular collisions. The specific underlying mechanism is usually modelled by defining a dimensionless parameter α, introduced by Shakura & Sunyaev in 1973 [104]. The stress tensor has the physical dimension of a pressure, therefore the simplest assumption is to take the stress tensor to be proportional to the vertically integrated pressure $\Sigma c_{\rm s}^2$, the constant of proportionality being α:

$$T_{R\phi} = \frac{d\ln\Omega}{d\ln R}\alpha\Sigma c_{\rm s}^2 \sim -\frac{3}{2}\alpha\Sigma c_{\rm s}^2 . \tag{2.29}$$

Another way of expressing this α-prescription is through the kinematic viscosity. Eq. (2.29) is equivalent to:

$$\nu = \alpha c_{\rm s} H . \tag{2.30}$$

In this picture, the magnitude of turbulent viscosity can be estimated as $\nu \sim \hat{v}l$, with l the typical size of a single vortex and $\hat{v}$ the turbulent velocity. Since turbulence dissipates energy through shocks, the velocity $\hat{v}$ is lower than the sound speed $c_{\rm s}$, while the maximum vortex size can not exceed the vertical disc scale H. Both these considerations imply that $\alpha < 1$. The $\alpha-$prescription provides a very effective framework to capture the effect of turbulence on angular momentum transport in accretion discs, connecting macroscopic disc dynamics to the microscopic turbulent processes.

2.1.2 Gravitational stability and self-regulation

The $\alpha-$prescription is not a theory of viscosity in accretion discs, but rather a simple framework to describe turbulent stresses. Angular momentum can also be transported by non-local mechanisms. Among the proposed sources of angular momentum transport are magneto-rotational instabilities (MRI) [105] and gravitational instabilities (GI) [106, 107]. By combining the continuity equation 2.2, the Navier-Stokes momentum equation 2.3, the Poisson's equation 2.5 and the equation of state 2.6 it is possible derive the dispersion relation that describes the propagation of density waves in the disc:

$$(\omega - m\Omega)^2 = c_{\rm s}^2 k^2 - 2\pi G\Sigma|k| + \kappa^2 \tag{2.31}$$

where k and m are the radial and azimuthal wave numbers, respectively, ω is the perturbation frequency, and κ is the epicyclic frequency defined as:

$$\kappa^2 = \frac{2\Omega}{R}\frac{d(\Omega R^2)}{dR} \tag{2.32}$$

with $\kappa \sim \Omega$. For axisymmetric perturbations ($m = 0$), the sign of ω determines the stability: if $\omega^2 > 0$ the perturbation is stable and it propagates as a classical wave, meanwhile if $\omega^2 < 0$ a exponentially growing perturbation emerges and the perturbation is unstable. A stable disc requires $\omega^2 > 0$, which is satisfied when:

$$Q = \frac{c_{\rm s} k}{\pi G\Sigma} > 1\,. \tag{2.33}$$

The dimensionless parameter Q is known as the 'Toomre parameter' [108]. When $Q \approx 1$, the disc self-gravity becomes significant and contributes to vertical hydrostatic equilibrium. The Toomre parameter can also be written as:

$$Q = f\frac{M}{M_{\rm d}}\frac{H}{R} \tag{2.34}$$

where f is a numerical factor, usually of order unity.

Although a value of $Q > 1$ indicates local stability, the disc is not necessarily quiescent: it can still develop instabilities and evolve towards a self-regulated state.

In particular, in the absence of heating or angular momentum transport, the disc gradually cools via radiative cooling until eventually $Q \approx 1$. At this point, gravitational instabilities arise, typically in the form of spiral structures inside the disc. The resulting compression and shocks efficiently dissipate energy, increasing the disc temperature and stabilising the system. If this process perseveres, the variations of the parameter Q will be very small and $Q \sim \bar{Q}$, with $\bar{Q}$ a constant of the order of unit.

This self-regulation mechanism can be formalised in steady-state models of self-gravitating accretion discs. In the steady-state approximation, the continuity equation 2.2 simplifies to:

$$\dot{M} = -2\pi R v_{\mathrm{R}} \Sigma \tag{2.35}$$

where $\dot{M}$ is the mass accretion rate. The negative sign indicates that an inward radial velocity (i.e.,the disc gas moves inward along the radial direction) corresponds to a positive accretion rate. Conservation of angular momentum together with the condition that the viscous torque vanishes at the inner disc radius R_{in}, allows to relate $\dot{M}$ and the effective viscosity ν:

$$\dot{M} = 3\pi\nu\Sigma \left(1 - \sqrt{\frac{R_{\mathrm{in}}}{R}}\right). \tag{2.36}$$

At large radii, this reduces to:

$$\dot{M} = \left|\frac{d\ln\Omega}{d\ln R}\right| 2\pi\nu\Sigma. \tag{2.37}$$

In the self-gravitating regime, where H is set by the balance of pressure and self-gravity (Eq. 2.36), it is possible to use the α-prescription to write the accretion rate as:

$$\dot{M} = 2\alpha \frac{{c_{\mathrm{s}}}^3}{G} \left|\frac{d\ln\Omega}{d\ln R}\right| \tag{2.38}$$

showing that the accretion rate in a steady state self-gravitating disc only depends on the turbulent efficiency parameter α and on the local sound speed c_s. Under the self-regulation condition given by:

$$Q = \frac{c_s \kappa}{\pi G \Sigma} = \bar{Q} \approx 1, \tag{2.39}$$

the sound speed can be expressed directly as a function of the accretion rate:

$$c_s = \left(\frac{G\dot{M}}{2\alpha} \right)^{1/3} . \tag{2.40}$$

Moreover, self-regulating condition requires that the disc cools on a timescale t_{cool} longer than the dynamical timescale $t_{dyn} = \Omega$, which can be expressed through the dimensionless cooling parameter β_{cool} [109]:

$$\beta_{cool} = \Omega t_{cool} \gg 1 \tag{2.41}$$

Similarly to the Q parameter, the β_{cool} parameter affects the disc evolution. The vast majority of existing numerical simulations that consider the disc self-gravity [35, 67, 75, 109, 110] make use of this simple cooling prescription to model the disc cooling. However, as discussed in Section 3.1, throughout the contest of this thesis, we adopt a more realistic radiative cooling in the form of black-body radiation.

Finally, if the disc is in thermal equilibrium, the viscosity parameter α is related to the cooling time as follows [111, 112]:

$$\alpha = \frac{4}{9} \frac{1}{\gamma(\gamma - 1)\beta_{cool}} , \tag{2.42}$$

linking the turbulent transport efficiency to the thermodynamics of the disc.

Finally, turbolence in accretion disc might arise from magneto-hydrodynamical instabilities, in particular from the MRI [105]. The condition for the MRI to take place, in the regime of ideal magnetohydrodynamics (MHD) and well-ionised discs, is that the angular velocity decreases outward, i.e., $\partial \Omega^2 / \partial R < 0$. This condition is generally satisfied in accretion disc, provided that the gas is perfectly coupled with the magnetic field.

2.1.3 Emission: Spectral Energy Distribution and Light Curve

The luminosity of an accretion disc is due to the dissipation of gravitational potential energy as matter moves towards the innermost part of the disc, losing angular momentum under the action of viscous forces. These forces exert a torque on each annulus of the disc, so that the difference between the torque at the inner and outer edges of each annulus determines the rate of energy dissipation. The power dissipated per unit area depends on viscosity, surface density, and orbital dynamics as:

$$D(R) = \nu\Sigma(R\Omega')^2 = \left|\frac{d\ln\Omega}{d\ln R}\right|^2 \nu\Sigma\Omega^2 \approx \left|\frac{d\ln\Omega}{d\ln R}\right| \frac{\dot{M}}{2\pi}\Omega^2 \,. \tag{2.43}$$

In a Keplerian non-self-gravitating disc, the potential is dominated by the central object and $D(R) \propto R^{-3}$, while in a self-gravitating disc $D(R) \propto R^{-2}$ and this results in higher energy dissipation than in the first case.

If the disc is optically thick, each element of the disc is assumed to emit as a black body at the disc surface with temperature equal to the effective temperature $T_{\rm eff}$. The effective temperature is given by the radiant emittance $j = 2\sigma_{\rm SB}T_{\rm eff}^4$ with $\sigma_{\rm SB}$ the Stefan-Boltzmann constant and the factor 2 accounts for the contribution from the two sides of the disc. In a steady disc, it is assumed that all the energy dissipated by viscous forces, $D(R)$, is radiated locally, so that $D(R) = j$. This allows us to compute $T_{\rm eff}$ as follows:

$$T_{\rm eff}(R) = \left(\frac{\dot{M}}{4\pi\sigma_{\rm SB}}\left|\frac{d\ln\Omega}{d\ln R}\right|\Omega^2\right)^{1/4} = \left\{\frac{3GM\dot{M}}{8\pi\sigma_{\rm SB}R^3}\left[1-\left(\frac{R_{\rm in}}{R}\right)^{1/2}\right]\right\}^{1/4} \tag{2.44}$$

with $R_{\rm in}$ the radius of the inner edge of the disc.

The effective temperature scales with the radius as $\propto R^{-3/4}$, meaning that the disc is characterised by a continuum of temperatures ranging from the higher values at the innermost radii to the cool outer regions. The black body emission follows the Plank's Law:

$$B_\nu\, d\nu(R) = \frac{2h\nu^3}{c^2}\,\frac{d\nu}{\exp(\frac{h\nu}{k_B T(R)})-1}\,, \tag{2.45}$$

where h is the Planck's constant, k_B is the Boltzmann constant and c is the light speed. The total spectrum emitted by a disc is called *multicolour black body* and is a superposition of many black body spectra, each corresponding to a different distance from the central object and thus to a different temperature according to Eq. 2.44. The total Spectral Energy Distribution (SED) emitted by a face-on disc is given by integrating the Planck's Spectrum over the disc surface as follows:

$$L(\nu)d\nu = 4\pi^2 \int_{R_{\rm in}}^{R_{\rm out}} RB_\nu d\nu dR\,, \tag{2.46}$$

with $R_{\rm out}$ is the maximum disc extension.

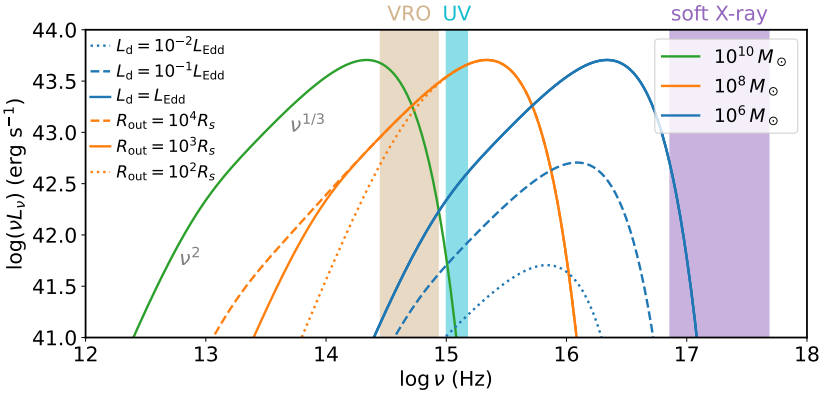

FIGURE 2.1: Spectral Energy Distribution of an accretion disc for different black hole masses, accretion rates (i.e., luminosities) and outer radii, as labelled in figure, computed in the rest frame of the sources. The vertical coloured bands correspond to the Rubin Observatory (optical), near-UV and soft X-ray frequency bands we will use in the context of this thesis work.

In figure 6.1 I show a few examples of a standard accretion disc emitting black-body radiation from its surface. By considering a logarithmic diagram $\log(\nu L_\nu) - \log(\nu)$, the total SED has three different asymptotic shapes [113]:

- **Low frequencies**: considering Eq. 2.44, the radiation is dominated by the outermost, coldest region and the Plank spectrum reduces to the Rayleigh-Jeans distribution:

$$h\,\nu \ll k\;T(R_{\rm out}) \Longrightarrow L_\nu \propto \nu^2 \tag{2.47}$$

- **Middle frequencies**: the total spectrum is given by the superposition of black body emission from several annuli and the asymptotic relation is the following:

$$kT(R_{\rm out})/h \ll \nu \ll kT(R_{\rm in}) \Longrightarrow L_\nu \propto \nu^{1/3} \tag{2.48}$$

  This spectral slope follows from the disc temperature profile $T(R) \propto R^{-3/4}$. More generally, the disc temperature decreases as a power low $T \propto R^{-q}$, then the intermediate spectral slope can be shown to follow $L\nu \propto \nu^{2/q-4}$ [114]. For a typical Shakura & Sunyaev disc, where $q = 3/4$, we have $L_\nu \propto \nu^{1/3}$, which represents the characteristic shape of a standard accretion disc. Deviation from this slope may reveal alternative temperature structures, for instance in discs governed by self-gravity or non-standard viscosity phenomena. Thus, the shape of the observed SED at intermediate frequencies strongly depends on the physics processes of angular momentum transport and energy dissipation.

- **High frequencies**: only the innermost, hottest zones contribute, the emission is exponentially suppressed according to the Wien approximation, producing a steep cut-off:

$$h\,\nu \gg k\;T(R_{\rm out}) \Longrightarrow L_\nu \propto \exp\left(-\frac{h\nu}{kT(R_{\rm in})}\right) \tag{2.49}$$

The specific shape of a multicolour black body spectrum is mainly determined by three parameters: the outer radius of the disc ($R_{\rm out}$), the accretion rate ($\dot{M}$) which is related to the disc luminosity ($L_{\rm d}$), and the black hole mass ($M_{\rm BH}$). Variations in any of these parameters modify the spectrum, while the asymptotic behaviours remain unchanged.

- For fixed $R_{\rm out}$ and assuming the BH accetes at a fixed fraction of the Eddington limit (so that $\dot{M} \propto M_{\rm BH}$), altering the black hole mass results in a rigid shift of the entire spectrum along the frequency axis. This occurs because the disc temperature depends on the black hole mass, according to the relation $T \propto M_{\rm BH}^{-1/4}$ (see Eq. 2.44), which determines the position of the blackbody spectrum. Figure 6.1 shows three examples: the spectra for $M_{\rm BH} = 10^6\,10^8, 10^{10}\,M_\odot$ are reported in blue, orange, and green line, respectively.

- For a fixed $R_{\rm out}$ and $M_{\rm BH}$, changing the accretion rate effects the temperature according to $T \propto \dot{M}^{1/4} \propto L_{\rm d}^{1/4}$ (see Eq. 2.44). Higher accretion rates increase the luminosity emitted by the disc. In Figure 6.1, are reported the spectra for a black hole of mass $10^6\, M_\odot$ with $L_{\rm d} = L_{\rm Edd}$, $L_{\rm d} = 10^{-1} L_{\rm Edd}$, and $L_{\rm d} = 10^{-2} L_{\rm Edd}$ using solid, dashed and dotted blue lines, respectively.

- Finally, $R_{\rm out}$ defines the maximum distance from the centre where the disc still emits significant radiation. Since this region corresponds to the coldest part of the disc, for fixed $\dot{M}$ and $M_{\rm BH}$, increasing the outer radius extends the intermediate-frequency branch of the spectrum, shifting the slope to lower frequencies. Thus, larger outer radii produce a longer low-frequency tail and modify the spectral slope as shown in Figure 6.1. The dashed, continue and dotted orange lines represent the blackbody spectra with $R_{\rm out} = 10^4$, 10^3, $10^2\, R_{\rm s}$ respectively, with $R_{\rm s}$ the Schwarzchild radius.

Assuming isotropic emission, the observed flux of a source located at redshift z within a given frequency range (ν_1,ν_2) is given by integrating the observed specific flux $f_\nu(\nu_0)$ as follows:

$$F = \int_{\nu_1}^{\nu_2} f_\nu(\nu_0)\, d\nu_0 = \int_{\nu_1}^{\nu_2} \frac{L_\nu(\nu_{\rm e})}{4\pi d_{\rm L}^2}(1+z)\, d\nu_0, \tag{2.50}$$

where $l_\nu(\nu_e)$ is the luminosity emitted at the rest-frame frequency ν_e, and $d_{\rm L}$ is the luminosity distance [115, 116].

With this information it is possible to express the total emitted luminosity as a function of time, in diagrams called 'Light Curves' (LCs). LCs are a useful tool in order to investigate the flux variations and modulations as well as MBH binaries properties because their variability can be related to the eccentricity, separation of the binary and the mass ratio between the black holes. On the other hand, MBH binaries are not the only possible cause of periodicity; there are single-MBH disc processes that might produce quasi-periodic emission as well. The possibility to produce detailed predictions of the EM signatures of binary accretion will aid in the interpretation of electromagnetic MBHB candidates.

The most challenging complication in the identification of genuine SBHBs from light-curve analysis arises from intrinsic quasar variability. Indeed, the LCs of accretion

discs around single BH generally show correlated red-noise variability, with power spectra well described by a power law ν^{-2}, that flattens at low frequency. This behaviour is reproduced by a *damped random walk* [DRW; 117] model, i which flux fluctuations are correlated over a characteristic timescale τ. It can mimic spurious periodic signals when only a few cycles are observed [118]. Confirming periodicity emitted by true MBHBs requires observing several orbital cycle, often $\gtrsim \mathcal{O}(10)$, making robust detections challenging with current baselines. On the other hand, systems hosting MBHBs may exhibit more coherent periodic or quasi-periodic modulation in the LCs, directly linked to the binary orbital period, eccentricity and mass ratio.

Non-thermal emission

In addition to the thermal multicolour black body emission produced by the accretion disc, active galactic nuclei (AGN) are also characterised by a strong non-thermal emission in the X-ray frequency band. This emission is expected to originate by a hot, optically thin corona located above and below the innermost regions of the disc. In this region, the UV/optical photons emitted by the disc are scattered at higher energy through the inverse Compton scattering, producing a power-law spectrum that extends into the hard X-ray frequencies (i.e., $0.2 - 10\,\mathrm{keV}$). The corona emission is proportional to the total luminosity of the disc through the correction factor, $K_{\rm band}$, which is defined as the ratio between the disc luminosity, $L_{\rm disc}$, and the luminosity in a given spectral band, $L_{\rm band}$; that is, $K_{\rm band} = L_{\rm disc}/L_{\rm band}$. In [119], the X-ray correction factor is computed empirically, combining several AGN samples. The bolometric correction $K_{\rm X}$ results to be:

$$K_{\rm X}(L_{\rm disc}) = a\left[1 + \left(\frac{\log(L_{\rm disc}/L_{\odot})}{b}\right)^{c}\right], \tag{2.51}$$

where a, b, c are best-fit parameters shown in Table 1 in [119]. Moreover, the hot corona emission produces a power law spectrum with $\nu L_\nu \propto \nu^{-0.7}$ [120] We then compute LCs including this additional contribution. The details of how the emission model is implemented within our framework is discussed in Section 3.3.4.

Part III

Simulations framework

Chapter 3

Simulations framework

Understanding the dynamical evolution of MBHBs , from the their early formation stages all the way to coalescence, and investigating how the surrounding environments impact their electromagnetic emission is crucial for interpreting current and future observations. To explore the evolution of a massive black hole binary across its phases, different but complementary approaches can be employed. Methods can be divided into analytical, semi-analytical, and numerical. Analytical methods are based on resolving the equation of motions using exact or approximate solutions under some, usually strict, caveats. They are useful in providing physical intuition to simplified descriptions. However, their applicability is usually restricted to ideal cases, such as isolated two-body systems. Semi-analytical approaches attempt to combine analytical prescriptions with phenomenological models. These methods are particularly effective for describing physical processes such as dynamical friction or the stellar scattering. Numerical simulations, on the other hand, represent the most general and versatile tool, as they directly integrate the equations of motion.Unfortunately, they are computationally expensive and, since numerical schemes involve a large number of modelling choices (e.g., integration methods, resolution limits, etc.), different implementations (e.g. Eulerian vs Lagrangian, 2D vs 3D) may produce different outcomes that reflect numerical limitations rather than genuine physical differences [e.g., 121]. In Section 3.1, I outline the main approaches typically used to study binaries embedded in circumbinary discs. Then, in Section 3.2 I provide an overview of the results obtained so far in the literature using different numerical and physical models. Finally, in Section 3.3 I present the methodology developed in this thesis to address the current lack of full 3D hydrodynamical simulations that characterise binary-disc interaction and the associated EM signatures at intermediate separations,

i.e., $10^{-4} - 10^{-2}$ pc.

3.1 Numerical techniques

Numerical simulations of MBHBs surrounded by circumbinary discs adopt different methods and assumptions to capture the disc-binary interaction, making the interpretation of the results non-trivial. The first distinction concerns the dimensionality of the simulation: 2D models are computationally fast and allow to perform simulations at higher resolution and for longer timescales compared to what can be typically done in 3D simulations within the same runtime. Even though they are more expensive, 3D simulations allow to resolve the disc structure in all the directions, providing a more realistic representation of the dynamics of the gas.

Another crucial difference is the numerical framework used to solve the system hydrodynamics equations. There are two approaches to describe the gas evolution as a fluid: the Eulerian (grid-based) approach and the Lagrangian (particle-based) approach. In the Eulerian approach, the simulation domain is divided into a grid and the fluid equations are solved on the grid cells. This approach is useful to look at the fluid motion focusing on fixed space locations through which the fluid flows with time, offering high accuracy in capturing shocks [122, 123]. In the Lagrangian approach, the fluid equations are solved for each fluid element, therefore following the motion of the fluid. A commonly used Lagrangian technique is the Smoothed Particles Hydrodynamics (SPH) [124, 125], in which the fluid is described as a collection of particles carrying properties such as mass, angular momentum, velocity and energy. For each particle, physical quantities are estimated through a weighted interpolation over its neighbours particles, using a smoothing kernel function. The extent of this interpolation is controlled by the smoothing length, which defines the characteristic scale over which the particles are "smoothed". Each particle interacts only with its neighbours within a distance comparable to the smoothing length. Many modern methods combine features of both approaches (e.g., mesh-free finite-volume techniques or moving-mesh schemes) [122, 126]. An advancement of SPH is the Mesh-less Finite Mass (MFM) method [123], in which particles still have fixed mass but fluxes of physical quantities are computed across effective faces between neighbours particles. The MFM method does not allow mass exchange between particles. However, it is possible to use the SPH technique in a way analogue to the Eulerian approach by discretising the fluid

into particles with a given volume. In this Mesh-less Finite-Volume (MFV) approach [123], the method computes the physical quantities across the effective particle interfaces and interparticle mass fluxes are allowed. As in the grid-based finite-volume method, the MFV provides a more accurate treatment of shocks and discontinuities.

The outcome of simulations of MBHBs embedded in circumbinary discs can be affected by the treatment of the binary orbit. In virtually all the grid-based simulations, the binary orbit is fixed over time, therefore violating the conservation of linear and angular momentum. Although this approximation can be done whenever the disc mass is negligible compared to the binary, it may lead to an inaccurate prediction of the binary orbital evolution [37]. 3D particle-based codes instead evolve the binary orbit consistently together with the gas particles, conserving linear and angular momentum.

Finally, simulations of MBHBs can lead to different results depending on which physical processes are included. Unfortunately, implementing phenomena such as disc self-gravity, radiation pressure or MHD effects, is often non-trivial. Moreover, running a comprehensive simulation including all the relevant physics can be computationally prohibitive. The diversity in numerical methods and physical models has resulted in a variety of outcomes, making it challenging to piece together a coherent picture. In the following section, I provide an overview of the results obtained so far in the literature, with the aim to summarise the current understanding of MBHBs in circumbinary discs.

3.2 Overview of previous MBHBs simulations

3.2.1 Binary-disc interaction and orbital evolution

In recent years, MBHBs and circumbinary discs have been extensively investigated with the aim of better understanding how the disc affects the evolution of the binary orbit and what are the emerging distinctive electromagnetic signatures. Despite significant progress, the diversity in numerical methods and physical models adopted has resulted in a variety of results. The interaction between the binary and the disc has been extensively modelled with hydrodynamics simulations in 2D [e.g., 29, 30, 32, 34, 71, 78, 88, 127–132], in 3D [e.g., 25, 33, 36, 37, 69, 70, 127, 133–136], including

the disc self-gravity [e.g., 35, 72, 75, 137], radiation pressure [80, 138–140], magnetic fields [73, 80], and general relativity [64, 77, 89, 141].

The choice of a physical model for the disc strongly influences the outcome of the interaction with the binary. The evolution of the binary semi-major axis depends on the contributions to the net torque from two distinct components: the gravitational torque exerted by the circumbinary disc on each binary component and the gas accretion torque. Early numerical simulations of circumbinary discs showed the binary inspiral to be aided by the presence of the disc [25, 69, 142]. The findings of more recent 2D, fixed binary orbit, simulations show that the angular momentum transfer onto the binary an be positive, leading to the expansion of the binary [29, 30, 34, 136]. In particular, [30] found that the sign of the torque depends on the binary mass ratio: systems with $q \geq 0.05$ can experience net positive torque (i.e., the binary migrate inward). Using a similar numerical scheme, [31] found that the fate of the binary depends on the disc temperature, i.e. on the disc aspect ratio. They find the threshold for expansion to be $H/R > 0.04$, while 3D SPH simulations of locally isothermal discs find the threshold to be much higher, i.e. $H/R = 0.2$ [33]. These results suggest that the disc aspect ratio H/R plays a critical role in the interaction between the disc and the binary but it is not the only component. In a recent study, [36] show, by employing 3D MFM simulations with hyper-Lagrangian resolution achieved via adaptive particle splitting, that the binary inspiral-outspiral depends also on the disc viscosity. Moreover, numerical simulations that study the regime where the disc self-gravity cannot be neglected, have found that the interaction between the binary and its gaseous disc leads the binary to shrink as a consequence of the time evolution of the disc temperature, regardless of its initial value [35, 67, 75, 137].

The interaction between the binary and its circumbinary disc changes the binary eccentricity as well [28]. Based on analytical arguments, [143] showed that an equilibrium eccentricity should exist, which was later confirmed by the SPH simulations of [72], who derived an equilibrium eccentricity $0.5 < e < 0.8$ for comparable mass binaries, linking the precise value to the disc cavity size. More recent 2D, fixed orbit, hydrodynamic simulations found equal-mass binaries to reach an equilibrium eccentricity value around ~ 0.45 [144, 145]. Using a very similar numerical scheme, [32] finds that binaries with mass ratios $q > 0.2$ evolve towards an equilibrium eccentricity of $e \sim 0.5$.

We can therefore conclude that the evolution of the semi-major of the binary depends on both the disc aspect ratio and the binary mass ratio and the eccentricity tends to reach an equilibrium at around ~ 0.5. However, the vast majority of previous works used a locally isothermal equation of state, assuming a constant gas temperature profile through the disc over time and therefore limiting the ability to capture shock-induced heating and its effect on the disc and ultimately on the binary. For instance, some of the gas that leaks inside the cavity is flung back towards the inner edge of the cavity, producing shocks which can alter the disc aspect ratio and temperature profile [69, 70] and may impact the evolution of the binary as well.

Moreover, additional physical processes such as magnetic fields and radiation pressure are expected to play a crucial role in the binary-disc interaction. MHD simulations [80, 81] have shown that magnetic stresses provide an efficient mechanism for angular momentum transport inside the disc, modifying both the accretion variability and the net torque on the binary. In this case, the disc is thicker and gas-pressure dominated , with strong accretion streams that lead to a more efficient accretion, reaching rates more than twice those obtained in purely hydrodynamical simulations [80]. However, simulations that include radiation pressure have shown a thinner and denser circumbinary disc, with weaker accretion streams and an accretion rate that drops to $\sim 0.1 - 0.2\,\dot{M}_{\rm edd}$, i.e., about a factor of 3 lower than in MHD-only runs. The cavity turns out to be less eccentric and the over-density at the inner edge of the cavity is less pronounced.

As the binary approaches coalescence, its evolution becomes dominated by gravitational waves emission. At this stage, the interaction with the circumbianry disc becomes negligible and the system enters the fully relativistic (GR/GRMHD) domain. GR/GRMHD regime can neglected when focusing on disc-binary interactions and the associated EM counterparts. Still, just to give a more comprehensive view, full GR and GRMHD simulations show that the gravitational field strongly modifies the gas distribution near the black holes, reducing the size of the mini-discs, and altering the cavity structure. At separations $\lesssim 100\,r_{\rm g}$, deviations from Newtonian predictions become significant, with accretion rates lower by up $20-30\%$. The cavity of the disc is more compact and less eccentric, influencing both the gravitational and accretion torques on the binary. [64, 77, 89, 141]

3.2.2 Periodic modulations of EM emission

Attempts to characterise the EM signatures from MBHBs at very small separations (i.e., tens to a hundred gravitational radii) have been made by several authors [e.g. 68, 74, 79, 141, 146–150]. It is well known established that binaries produced a modulation in the accretion rate over their orbital period, which might produce a corresponding periodicity in the emitted flux. Another promising EM signature, of MBHBs is the so-called 'lump', an over-density region orbiting at the cavity edge of the circumbinary disc with an orbital period a few times longer than the binary orbital period, as explained in Section 2.1.3. Early 2D hydrodynamical simulations [e.g., 71, 78] showed that the lump can modulate the accretion rate onto the binary, producing periodic variability in the emitted light. Subsequent 2D and 3D simulations [64, 68, 72, 74, 75, 141, 151], also including magnetic fields [73, 76, 79] attempted to characterise the EM signatures from MBHBs at very small separations (i.e. tens to a hundred gravitational radii $R_{\rm g}$), confirming the lump formation and stability influence the EM emission. These results have been further validated by 3D general relativistic magneto-hydrodynamics (GRMHD) simulations [65, 76, 77]. Despite the diversity in numerical methods and physical models adopted, all these studies consistently find that the lump originates when the particles of gas flung back to the cavity edge shock and deposit material at the inner edge of the circumbinary disc. Moreover, the lump is stronger in circular equal-mass binaries, with amplitude decreasing for lower mass ratios, being a possible smoking gun signature of circularity or equal mass systems [74].

The characterisation of the interaction binary-disc and the EM signatures at intermediate scales - that is, separations $\sim 10^{-4} - 10^{-2}$ pc from full 3D hydrodynamical simulations that resolve the thermal evolution of the circumbinary disc also under the influence of radiation pressure - is currently missing and is of fundamental importance for aiding the identification of the origin of the GWB signal found with PTA experiments. Furthermore, the modelling of these signatures is of paramount importance for the identification of MBHB candidates in time-domain surveys, which can constitute the cosmic population of precursors of the merging binaries that will be detected by LISA. In the following section, I present the methodology developed in this work to address this gap.

3.3 Methodology adopted in this work

3.3.1 Numerical setup and initial conditions

We performed 3D hyper-Lagrangian resolution hydrodynamics simulations of the evolution of the circumbinary disc around an accreting MBHB. We used the 3D meshless finite mass (MFM) version of the code GIZMO [123] combined with the adaptive particle splitting technique [see 36, for details] to increase the resolution inside the cavity carved by the binary. The MBHBs have, in code units, a total mass of $M_{\rm B} = M_1 + M_2 = 1$, where M_1 and M_2 are the masses of the primary and secondary black hole, respectively, and the initial semi-major axis, $a_0 = 1$. Each MBH is modelled as a sink particle with an accretion radius of $R_{\rm sink} = 0.05a$. As the binary orbit is allowed to evolve with time [37], conservation of mass, linear and angular momentum are ensured during each accretion event, in the same way as is done in the PHANTOM code [133]. We initially modelled the circumbinary disc with $N = 10^6$ gas particles for a total mass of $M_{\rm D} = 0.01M_B$. The mass is distributed with an initial surface density profile of $\Sigma \propto R^{-1}$ and a radial extent between $R_{\rm in} = 2a$ and $R_{\rm out} = 10a$. The disc is co-planar with the binary orbit and has an initial aspect ratio of $H/R = 0.1$ in all my simulations. We generated the disc initial conditions using the SPH code PHANTOM [152].

3.3.2 Disc physics

In our model, the thermodynamic evolution of the gas follows an adiabatic equation of state with index $\gamma = 5/3$, so that the disc is allowed to heat and cool and it is possible to capture the effect of shocks. In the Shakura-Sunyaev accretion disc model, the angular momentum transport within the disc is modelled with the α viscosity parameter, which constitutes a simple parametrisation of the turbulence within the disc. This turbulence might be driven by the magneto-rotational instability in highly ionised discs [153]. We therefore included viscosity using the Shakura-Sunyaev parametrisation with a kinematic viscosity of $\nu = \alpha c_{\rm s} H$, where $c_{\rm s}$ is the gas sound speed, $\alpha = 0.1$, and the disc thickness H is $H = c_{s,i}/\Omega_K$. Since we do also include the disc self-gravity together with a cooling prescription, our discs may develop gravitational instabilities that will eventually result in an additional source of angular momentum transport [110, 154, 155]. To ensure the gravitational stability of the disc, we set the initial Toomre parameter, $Q > 1$ [108].

As discussed in Section 2.1.2 and Section 3.2, the vast majority of existing numerical simulations that consider the disc self-gravity [e.g., 35, 67, 75, 109, 110] make use of a simple cooling prescription that assumes gas to cool on a timescale, $t_{\rm cool}$, that is a multiple, $\beta_{\rm cool}$, of the dynamical time, $t_{\rm dyn} = \Omega^{-1}$; that is, $\beta_{\rm cool} = \Omega t_{\rm cool}$. In this work, we have used a more realistic radiative cooling in the form of black-body radiation. The cooling rate is given by

$$\Lambda_{\rm cool} = \frac{8}{3}\frac{\sigma_{\rm SB} T_{\rm i}^4}{\kappa \Sigma}, \tag{3.1}$$

where $\sigma_{\rm SB}$ is the Stephan-Boltzmann constant, κ is the opacity, Σ is the 3D disc surface density, and $T_{\rm i}$ is the temperature of each element. We compute Σ in 3D using the Sobolev length approximation as $\Sigma \sim \rho^2/|\nabla\rho| + \rho * h/N_{\rm ngb}$ where ρ is the 3D volumetric density, $|\nabla(\rho)|$ is the norm of the gradient, h is the smoothing length, and $N_{\rm ngb}$ is the number of neighbours. We assume the opacity, κ, to be a combination of the Kramer opacity, $\kappa_{\rm Kramer} = 4.0 \times 10^{25}(1+X)(0.013+0.001)\rho T_{\rm i}^{-7/2}$ (which includes the contribution from free-free, bound-free and bound-bound transitions), with a hydrogen mass fraction of $X = 0.59$, and the electron-scattering opacity $\kappa_{\rm es} = 0.2(1+X)\,{\rm cm^2\,g^{-1}}$. We do not model optically thin regions: we assume optical thickness larger than 1 and neglect any effect related to a possible atmosphere around the disc.

3.3.3 Parameters space

When scaled to physical units, all the simulations have a binary total mass of $M_{\rm B} = 10^6 M_\odot$ and initial separation of $a = 4.8 \cdot 10^{-4}\,{\rm pc} \simeq 1.2 \cdot 10^4\,{\rm R_g}$, where $R_{\rm g} = GM_{\rm B}/c^2$ is the gravitational radius of the binary. This implies that we can follow the gas only down to $R_{\rm sink} = 0.05a \sim 600 R_{\rm g} \sim 100 R_{\rm ISCO}$. Therefore, it is important to bear in mind that in the following analysis we are neglecting the emission in the region between $100R_{\rm ISCO}$ and $R_{\rm ISCO}$ and the total luminosity of the system is likely going to be underestimated, especially in the UV and X-ray bands. Choosing this particular semi-major axis value sets the orbital period of the binaries to 1 year. Since my final aim is to analyse the EM counterparts that Vera Rubin Observatory surveys would detect, given its 10 years survey duration, this choice of semi-major axis implies that we can observe the flux emitted by the source over 10 orbital periods. We modelled binaries with an eccentricity of $e = 0,\ 0.45,\ 0.9$ and mass ratio of $q = 0.1,\ 0.7,\ 1$. We

performed a total of 9 simulations, three of which accounted for radiation pressure. We run the binary simulations for 1300 binary orbits (with the exception of the $e = 0.45$, $q = 0.7$ case, which is evolved for $1600\,P_{\rm B}$) to ensure that the disc reaches a quasi-steady state, i.e. the ratio between the change in binary angular momentum over accretion rate does not change with time. We placed the simulated binary at different redshifts of $z = [0.1, 2]$, and analysed the observed flux in different frequency bands, mainly focussing on the optical band that will be probed by the upcoming Vera Rubin Observatory [Rubin Observatory; 156].

3.3.4 Thermal and non-thermal emission model

Thermal emission model

For each gas particle, i, we calculated the temperature, $T_{\rm i}$, assuming that both gas and radiation pressure contribute to the hydrostatic equilibrium of the disc, and thus numerically solving the following implicit equation for T_i at each resolution element:

$$P_{\rm tot} = P_{\rm gas} + P_{\rm rad} = \frac{\rho k_{\rm B} T_{\rm i}}{m_{\rm p}\mu} + \frac{4}{3}\frac{\sigma_{\rm SB} T_{\rm i}^4}{c}. \tag{3.2}$$

We divided the disc temperature domain into a 2D matrix with dimensions of 512×512 pixels in the x-y plane, which coincides with the MBHB orbital plane. For each pixel, we computed the midplane temperature as the average temperature of all the particles within the z co-ordinate $-0.05a < z < 0.05a$, obtaining the midplane temperature matrix, T. For a more detailed analysis of the mini-discs, we further divided the spatial domain from the sink radius of each MBH out to $r = 3a$ into a 2D matrix of 512×512 pixels. For each pixel in this grid, we computed the midplane temperature, T, using the same method outlined above.

In the classical thin disc approximation, the expression of $T_{\rm eff}(R)$ presented in Eq. 2.44 is obtained from the balance between local viscous dissipation and blackbody radiation and it is valid if the vertical structure of the disc is ignored. However, when the vertical structure of the disc is taken into account, it is more appropriate to relate the effective temperature to the midplane temperature $T_{\rm c}$ and the optical depth τ as:

$$T_{\rm eff}^4 = \frac{4}{3}\frac{T_{\rm c}^4}{\tau}, \tag{3.3}$$

with the optical depth defined as $\tau = \kappa\Sigma$. Moreover, using this approach it is possible to take into account the radiative transfer through the vertical column of the disc. We then computed the effective temperature in the optically thick approximation ($\kappa\Sigma > 1$) in each element of both matrices following the latter approach.

We obtained the flux emitted by each pixel using Planck's formula:

$$dL_\nu \equiv B_\nu \, \mathrm{d}\nu \mathrm{d}A = \frac{2h\nu^3}{c^2} \frac{\mathrm{d}\nu}{\exp\left(\frac{h\nu}{k_\mathrm{B}T_\mathrm{eff}}\right) - 1} \mathrm{d}A \,, \tag{3.4}$$

where h is the Planck constant, k_B is the Boltzmann constant, and $\mathrm{d}A$ is the area of each element. In order to analyse the different contributions to the emission from each part of the disc, we have divided the simulated domain into five different regions: the two mini-discs that extend from the sink radius of each component to the Roche Lobe size, the streams region that extends from outside the Roche Lobe out to $r = 3a$, an inner part of the disc, $3a < r < 5a$, and an outer part of the disc, $5a < r < 10a$. For each region, we computed the SED through the sum of each pixel flux obtained with Eq. 3.4.

Non-thermal emission model

We further added the non-thermal emission that is expected to originate from the corona using the correction to the bolometric luminosity in [119] in the hard X-ray (i.e. $0.2 - 10\,\mathrm{keV}$) band as explained in Section 2.1.3. However, we assume that the corona emission is proportional to the total luminosity of the mini-discs instead of the total luminosity of the circumbinary disc. We assume the mini-discs to behave similarly to single MBH AGN discs, where the X-ray emission is produced by the corona, as there is no clear description available to date of the properties of the non-thermal corona in the accretion discs that form around the binary components. To compute the X-ray correction factor, K_X, we follow the Eq. 2.51 using the mini-discs' luminosity, L_MDs, instead of the bolometric one L_bol.

Since we ultimately want to obtain LCs to compare with future observations, we placed the source at different distances from the observer and, assuming isotropic emission, we computed the total flux in different bands following 2.50.

TABLE 3.1: Frequency bands and 5-σ flux sensitivities of the Rubin Observatory telescope's optical filters.

	y	z	i	r	g	u	
lower	2.83	3.25	3.67	4.34	5.43	7.5	$\times 10^{14}$ Hz
upper	3.16	3.67	4.34	5.43	7.5	8.57	$\times 10^{14}$ Hz
5σ sensitivity flux	40.58	9.23	4.47	3.11	2.32	6.04	$\times 10^{-15}$ erg/s/cm^2

https://pstn-054.lsst.io/PSTN-054.pdf for magnitude values details.

Sensitivity limits of Vera Rubin Observatory

In order to understand whether these changes in the observed flux are detectable, we need to simulate a realistic detection scenario, taking into account the sensitivity limit of the employed survey and its observation time span. In particular, in all our studies we focus on MBHB observability with the Rubin Observatory. To infer the observability of the systems, we adopt a similar method to the one used by [82]. We add to the simulated fluxes in the optical bands a Gaussian noise with variance given by the 5σ sensitivity of the telescope in the considered band. We then performed a fast Fourier transform (FFT) onto a limited number of cycles (commensurate to a survey time span of ≈ 10 years) and qualitatively identified whether prominent peaks in the spectrum appear and what their origin is. We defer a more thorough statistical study of the detectability of these features to a follow-up study (F.Cocchiararo et al., in prep). The Rubin Observatory 5σ sensitivities in different bands are listed in Table 3.1.

3.3.5 Implementation of radiation pressure in GIZMO

We implement the radiation pressure contribution in GIZMO using an approximate formulation that does not require solving the full radiation hydrodynamics equations. We first determined the initial temperature $T_{0,\mathrm{i}}$ by solving the following relation :

$$\frac{4}{3}\frac{\sigma_{SB}}{c}T_{0,\mathrm{i}}^4 + \frac{\rho_{\mathrm{i}} k_B}{\mu m_p} T_{0,\mathrm{i}} - \rho_{\mathrm{i}} c_{\mathrm{s,i}}^2 = 0 \tag{3.5}$$

where $c_{\mathrm{s,i}}$ is the sound speed of the gas element i determined by the radial profile

$$c_{\mathrm{s,i}} = \frac{H}{R}\sqrt{\frac{M_1 + M_2}{a_0}} r^{-0.5} \,. \tag{3.6}$$

Using $T_{0,\mathrm{i}}$, we calculated the initial internal energy $u_{0,\mathrm{i}}$ for each gas element i as the sum of the gas internal energy and the radiation internal energy. The values of $u_{0,\mathrm{i}}$ are included in the initial conditions file, ensuring that the contribution of the radiation pressure is accounted for at the beginning of each simulation. We then evolve the internal energy equation over time.

At each time-step of the simulation, the temperature T_i is re-calculated from the updated internal energy u_i by solving:

$$4\frac{\sigma_\mathrm{SB}}{c\rho_\mathrm{i}}T_\mathrm{i}^4 + \frac{3}{2}\frac{k_\mathrm{B}}{\mu m_\mathrm{p}}T_\mathrm{i} - u_\mathrm{i} = 0 \tag{3.7}$$

and the ideal gas pressure is computed as $P_\mathrm{gas} = (\rho_\mathrm{i} k_\mathrm{B} T_\mathrm{i})/(\mu m_\mathrm{p})$. In order to account for the contribution of radiation pressure, we compute the parameter β, defined as the ratio of gas pressure to total pressure:

$$\beta = \frac{1}{1 + \frac{4}{3}\frac{\sigma_\mathrm{SB}}{c}\frac{T^4}{P_\mathrm{gas}}}. \tag{3.8}$$

We use this parameter to modify and update the effective adiabatic index γ_β in the equation of state, ensuring a self-consistent treatment of the coupled gas and radiation pressure, using the following definition [157]:

$$\gamma_\beta = \beta + (4 - 3\beta)^2 \frac{\gamma - 1}{\beta + 12(\gamma - 1)(1 - \beta)}. \tag{3.9}$$

The adopted approach differs from full RMHD treatment such as the one in [80], where the radiative transfer equation is solved with the MHD equations and radiation is evolved as an independent dynamical component, with its energy and angular momentum. Such approach captures radiative transport, anisotropic radiation fields at a higher computational cost. In contrast, our method assumes local thermodynamic equilibrium between gas and radiation, neglecting explicit radiative transport. Radiation pressure contributes to the total pressure and internal energy via the adiabatic index γ_β in Eq. 3.9. This adopted approach has some limitations as it does not treat optically thin regions. However, it is computationally efficient and captures the main impact of radiation pressure in optically thick gas, which is the environment we are interested in in the context of this thesis.

Part IV

Results

Chapter 4

Electromagnetic signatures from accreting massive black hole binaries in time domain photometric surveys

Based on:

F.Cocchiararo, A.Franchini, A.Lupi, A. Sesana,

"Electromagnetic signatures from accreting massive black hole binaries in time domain photometric surveys", 2024 A&A, 691, A250, DOI, ADS link

---

In this chapter, we study spectral and time variability of accreting MBHBs at milli-parsec separations surrounded by a geometrically thin circumbinary disc. To this end, we present the first computation of the expected SEDs and LCs from 3D numerical simulations with hyper-Lagrangian refinement of these systems. We have taken into account the thermodynamic evolution of the gas using a radiative cooling prescription in the form of black-body radiation. We have also included the self-gravity of the disc, which is usually neglected, and the Shakura-Sunyaev prescription for viscosity. We model binaries of mass $10^6\,M_\odot$, with an eccentricity of $e = 0$, 0.9 and mass ratio of $q = 0.1$, 1 and then compute their emitted spectra and LCs. We also added to the spectrum the contribution from a non-thermal corona, based on the assumption that its emission is proportional to the radiation emitted by the discs around each binary component (e.i., mini-discs). We placed the simulated binary at different redshifts

of $z = 0.1, 0.4, 0.7$, and analysed the observed flux in different frequency bands, mainly focussing on the optical band that will be probed by the upcoming Rubin Observatory [156]. As an exercise, we then assumed the source to be two orders of magnitude brighter, but still preserving the same LC, and we investigated the observability with the Rubin Observatory at higher redshifts of $z = 1, 2, 3$. Finally, we analysed the time evolution of the disc and binary properties such as the aspect ratio, H/R, the semi-major axis, a, and the eccentricity, e, of the binaries.

The numerical details and the initial conditions of the simulations are describe in Sec. 3.3.1 and Sec. 3.3.3. The physical assumptions of the disc together with the thermal and non-thermal emission calculation are presented in Sec. 3.3.2 and in Sec. 3.3.4, respectively. In the following, we show and discuss the main results we obtain, including the time evolution of the main binary and disc properties. Finally, we draw our conclusions and discuss possible observational implications.

4.1 Disc and binary evolution

Since our numerical simulations are 3D and the gas is allowed to change its temperature with time, we can resolve gas shocks and investigate the effect they have on the final temperature of the disc. As showed by previous simulations in the literature [36, 64, 68–74], part of the streams of gas that enter the cavity is flown back to the disc, creating shocks at the inner edge of the cavity wall that affect the disc aspect ratio. Figure 4.1 shows the evolution of the aspect ratio profile at $t = 0, 500, 700, 900, 1000, 1300\, P_{\rm B}$ for the circular cases (upper panels) and eccentric cases (lower panels) with mass ratio $q = 1$ (left panels) and $q = 0.1$ (right panels). For each radial bin with N particles, we compute the aspect ratio as:

$$\frac{H}{R} = \frac{1}{R}\sqrt{\frac{1}{N-1}\sum_{i=1}^{N}(z_{\rm i} - \bar{z})^2}\,, \tag{4.1}$$

with $\bar{z} = \frac{1}{N}\sum_{i=1}^{N} z_i$ the mean of the vertical coordinates and $R = \frac{1}{N}\sum_{i=1}^{N} R_i$ the mean radius of the particles in each radial bin. In order to exclude gas particles too far from the disc, we select only gas particles whose density $\rho_{\rm i}$ is higher than the minimum particle density at the initial time. Since the Toomre parameter $Q > 1$, the disc cools down until $Q \sim 1$. Indeed, the aspect ratio decreases from the initial

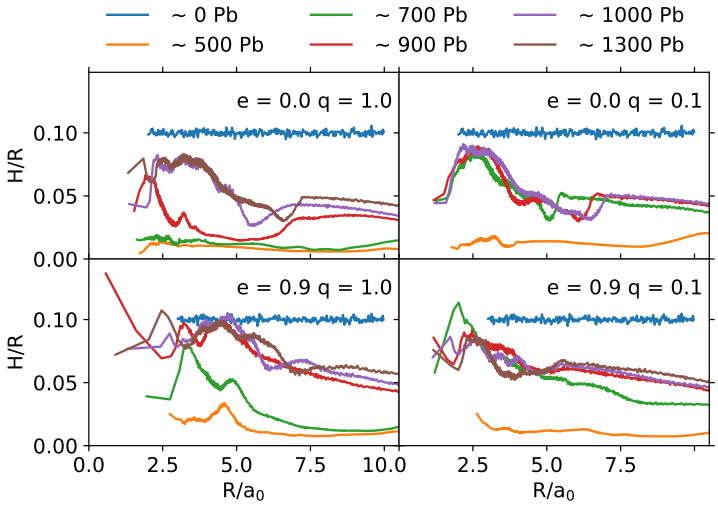

FIGURE 4.1: Time evolution of the disc aspect ratio, H/R, as a function of radius for circular binaries (top panel) and eccentric binaries (bottom panel) with a mass ratio of $q = 1$ (left column) and $q = 0.1$ (right column). For all the simulations, we report the thickness profile at different times with different colours. All the simulations start with $H/R = 0.1$.

value $H/R = 0.1$ to $H/R \sim M_{\rm D}/M_{\rm B} \sim 0.01$ within the first few orbits, with $M_{\rm D}$ and $M_{\rm B}$ the mass of the disc and the binary, respectively. In all our simulations, the disc then re-expands in the vertical direction and the aspect ratio increases, eventually reaching a stable profile. This is consistent with the disc temperature increase from an initial value at the inner edge of $T_{\rm eff} \sim 10^3\,K$ to a final value of $T_{\rm eff} \sim 10^4\,K$. Since gas particles are continuously flung back into the cavity wall, the shocks that occur in this region maintain the disc aspect ratio to $H/R \sim 0.08$, regardless of the choice of binary mass ratio and eccentricity. The radiative cooling in the outer parts of the disc is more efficient and the aspect ratio reaches eventually a value $H/R \sim 0.04$. Equal-mass binaries have a bigger quadrupole mass moment that exerts larger torques on the inner edge of the disc cavity, eventually producing more prominent streams and stronger shocks. As a consequence, discs around equal-mass binaries reach a stable configuration after $\sim 1000\,{\rm P_B}$ ($e = 0$) and $\sim 900\,{\rm P_B}$ ($e = 0.9$), while it takes only $\sim 700\,{\rm P_B}$ for discs around unequal-mass binaries, regardless of eccentricity. The evolution of the binary semi-major axis depends on the contributions to the net torque from two distinct components: the gravitational torque exerted by the circumbinary disc on each binary component and the gas accretion torque [see 72, for the detailed computation of the two contributions]. Early numerical simulations of circumbinary discs showed the binary inspiral to be aided by the presence of the disc [25, 69, 142].

The findings of more recent 2D, fixed binary orbit, hydrodynamic simulations show that the angular momentum transfer onto the binary is positive and this leads the expansion of the binary [29, 30, 34, 136]. Using a similar numerical scheme, [31] found that the fate of the binary depends on the disc temperature, i.e. on the disc aspect ratio. They find the threshold for expansion to be $H/R > 0.04$, while 3D smoothed particle hydrodynamics (SPH) simulations of locally isothermal discs find the threshold to be much higher, i.e. $H/R = 0.2$ [33]. In a recent study, [36] show, employing 3D MFM simulations where hyper-Lagrangian resolution was achieved via adaptive particle splitting (the same method employed here), that the binary inspiral-outspiral depends also on the disc viscosity. Numerical simulations that study the regime where the disc self-gravity cannot be neglected, have found that the interaction between the binary and its gaseous disc leads the binary to shrink as a consequence of the time evolution of the disc temperature, regardless of its initial value [35, 75, 137].

The interaction between the binary and its circumbinary disc changes the binary eccentricity as well [28]. Based on analytical arguments, [143] shown that an equilibrium eccentricity should exist, which was later confirmed by the SPH simulations of [72], who derived an equilibrium eccentricity $0.5 < e < 0.8$ for comparable mass binaries, linking the precise value to the disc cavity size. More recent 2D, fixed orbit, hydrodynamic simulations found equal-mass binaries to reach an equilibrium eccentricity value around ~ 0.45 [144, 145]. Using a very similar numerical scheme, [32] finds that binaries with mass ratios $q > 0.2$ evolve towards an equilibrium eccentricity of $e \sim 0.5$.

While these latter works [36, 144, 145] assumed the disc to be locally isothermal, here we have allowed the disc temperature to change with time due to PdV work heating and radiative cooling. We find the interaction between the binary and the circumbinary disc to cause the binary to shrink, regardless of the initial conditions. In particular, a decreases by $\sim 1\%$ over ~ 1000 orbits in all cases, except for the binary with $q = 0.1$ and $e = 0.9$. In this case, the binary initially experiences an expansion of 0.05% over the first 600 orbits, likely because of the very high eccentricity that brings the lower mass MBH very close to the initial cavity edge. This is only a transient phase, as the binary then carves a larger cavity compared to the circular case and starts to shrink, transferring angular momentum to the circumbinary disc. We find

the eccentricity value to remain relatively constant during the whole simulation for initially eccentric binaries, while circular ones feature a mild eccentricity increase, reaching $e \sim 0.04$ in the equal-mass case and $e \sim 0.06$ in the unequal-mass case.

4.2 Analysis of the electromagnetic counterparts

4.2.1 Spectral energy distributions

We computed the EM emission from our numerical simulations by using Planck's Law (see Eq. 3.4), taking into account both the gas and the radiation pressure contribution when computing the disc temperature, as is mentioned in Sect. 3.3.3. We divided our simulated domain into five different regions: the mini-disc region that extends from the sink radius of each binary component out to the Roche Lobe size, the stream region that extends from outside the Roche Lobe out to $r = 3a$, and the inner ($3a < r < 5a$) and outer ($5a < r < 10a$) parts of the disc. For each region, the total SED was obtained by integrating the flux emitted by each pixel over the whole spatial domain.

Figure 4.2 shows the surface density maps, the effective temperature maps, and the SED obtained for each region at $t = 1298\, P_{\rm B}$ for the circular equal-mass binary. Each panel line shows a different orbital phase of the binary. Periodically, a small fraction of gas enters the cavity and feeds the mini-discs around each binary component through the streams. We assume an initial disc temperature profile that decreases with radius as $R^{-0.5}$. The inflow of gas into the cavity combined with the exchange of material among the mini-discs generates shocks that increase the gas temperature, resulting in an effective temperature of $T_{\rm eff} \sim 10^4\,{\rm K}$, warmer than the outer parts of disc.

As is shown by the four different orbital phases in Fig. 4.2, the mini-disc and stream temperature variations occur within an orbital period, producing EM emission variations. The spectra obtained by analysing the emission from the mini-discs and the streams region (blue, orange, and green lines) do indeed exhibit more variability than the inner and outer regions of the disc (red and purple lines). The emission peak of the mini-discs and the streams region changes frequency between the optical and UV band ($\log(\nu/{\rm Hz}) \sim 14.6 - 15.2$) spanning one order of magnitude in luminosity, while the emission peak of the circumbinary disc remains between the IR and optical band during one orbital period.

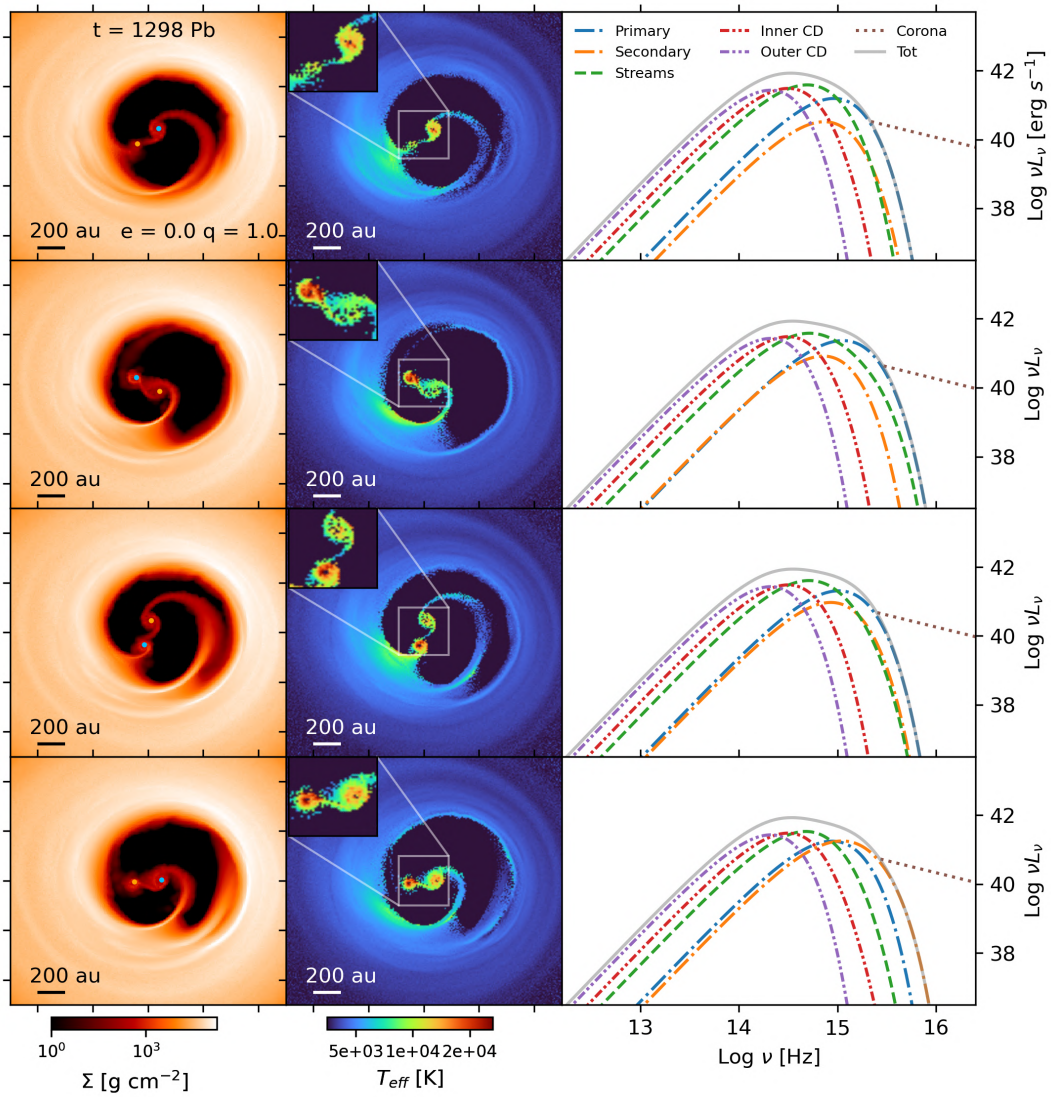

FIGURE 4.2: Surface density map, effective temperature map and SEDs for a circular equal-mass binary. From the top to the bottom row: the binary at four different orbital phases at time $t = 1298\,P_{\rm b}$. The left, middle, and right panels in each row show the surface density map in the $x-y$ plane, the effective temperature map in the $x-y$ plane and the SEDs. The tick spacing on the x and y axes in the left and central panels is $2a_0$, where a_0 is the initial binary semi-major axis. The surface density upper limit is set at $1.8\times10^5\,{\rm g\,cm^{-2}}$. In the SEDs, the contribution of the mini-discs around the primary and the secondary black hole is shown by the dash-dotted blue and orange lines, respectively, the stream region is represented by the dashed green line while the inner and outer part of the circumbinary disc are represented by the dash-dotted red and purple lines, respectively. The corona contribution is shown by the dotted brown line. The solid grey line shows the total emitted spectrum.

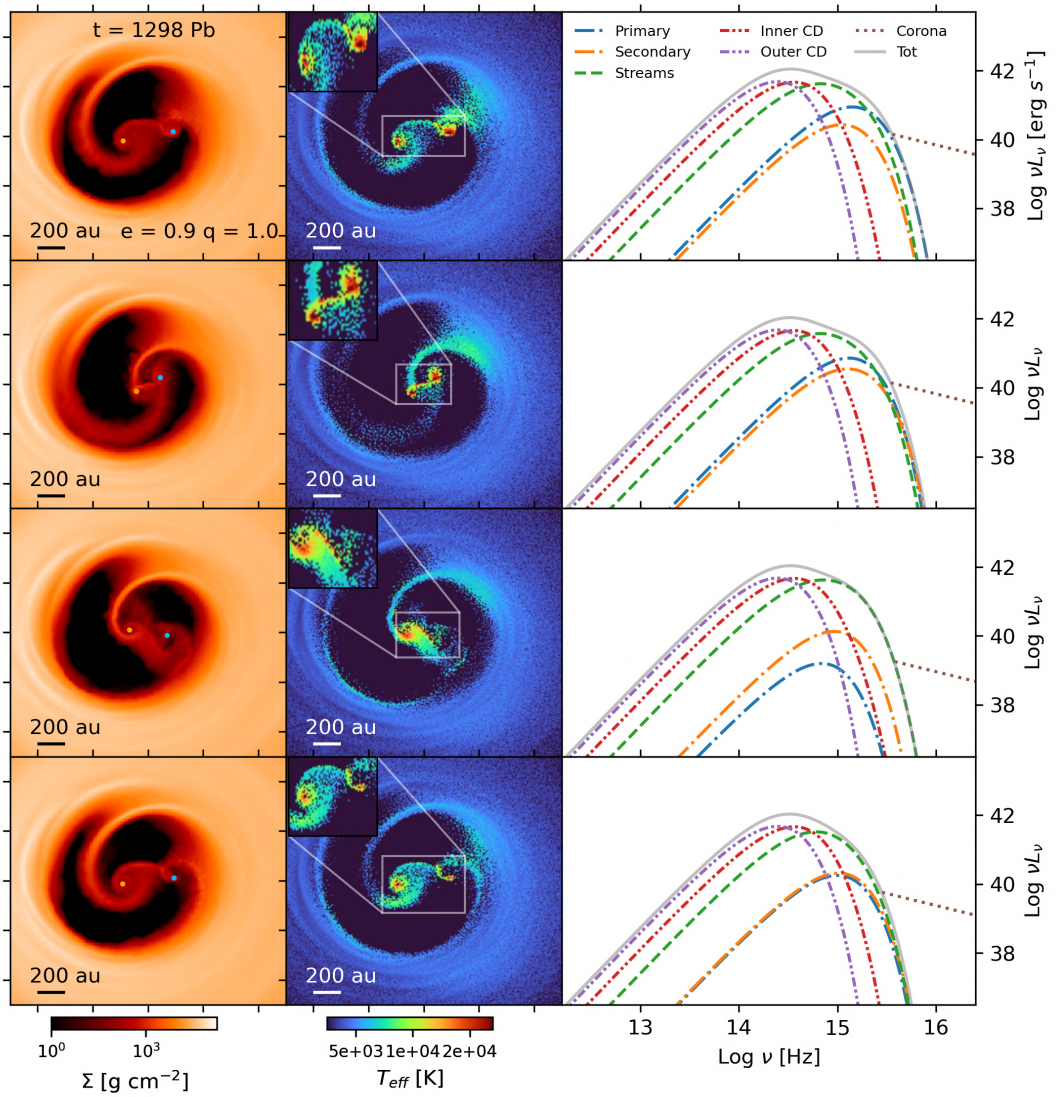

FIGURE 4.3: Same as Fig. 4.2 but for the highly eccentric $e = 0.9$ equal-mass binary.

In the highly eccentric $e = 0.9$ case (see Fig. 4.2), the emission from the cavity shows more variability than in the circular case, due to the geometry of the orbit of the components. Indeed, the emission peak of the mini-discs and the stream component changes between the optical and UV band ($\log(\nu/\mathrm{Hz}) \sim 14.8 - 15.4$) spanning two orders of magnitude in luminosity ($\log(\nu L_\nu/\mathrm{erg\,s^{-1}}) \sim 39 - 41$).

We find the mini-discs to have a lower temperature in the circular unequal-mass case (see Fig. 4.4) with respect to the circular equal-mass case shown in Fig. 4.2. Indeed, the exchange of material between the mini-discs does not produce significant shocks and the temperature does not increase as much as in the circular case. Therefore, the emission peak of the mini-discs is shifted to lower frequencies, $\log(\nu/\mathrm{Hz}) \sim 14.8{-}15.2$,

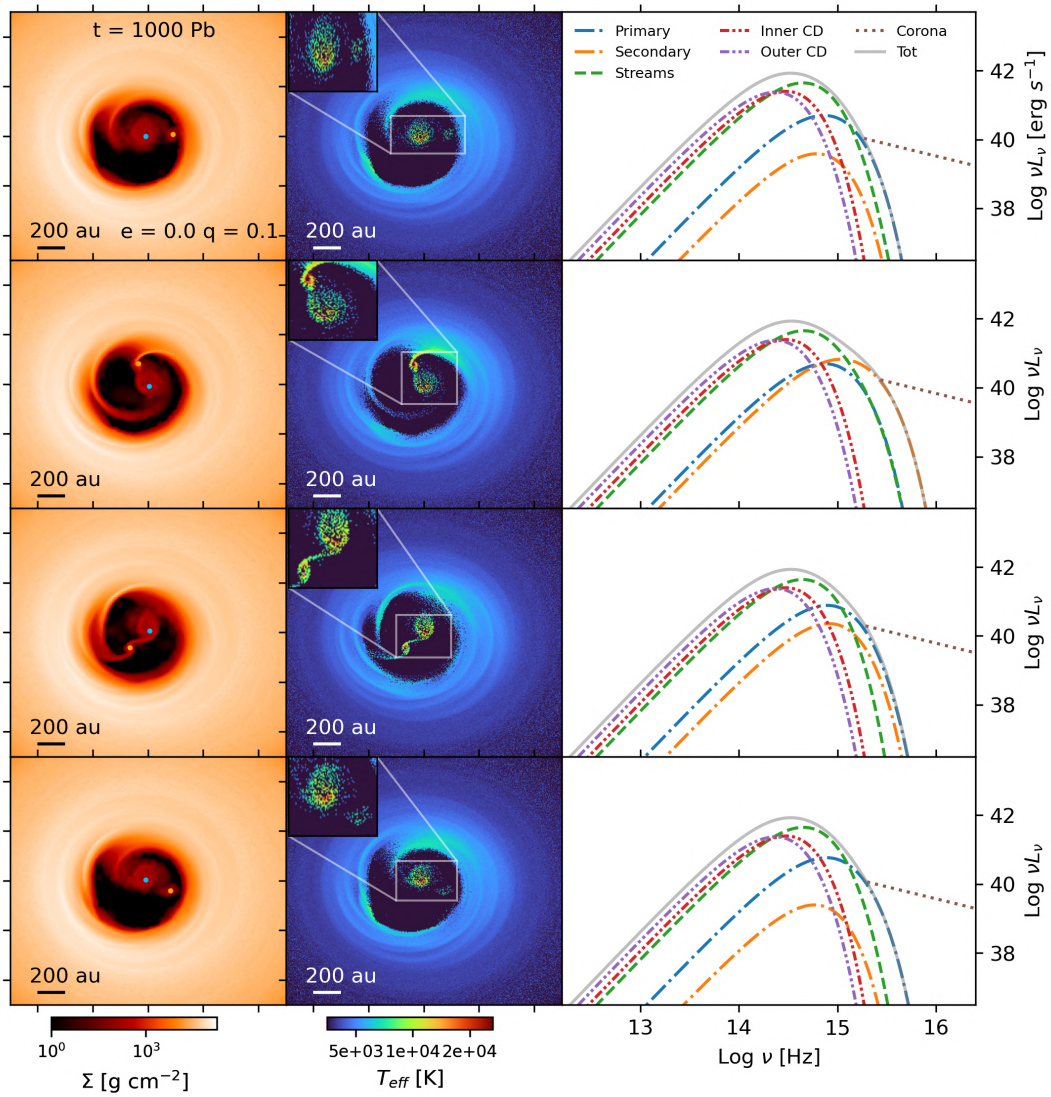

FIGURE 4.4: Same as Fig. 4.2 but for a binary with mass ratio $q = 0.1$ and eccentricity $e = 0$ and at time $t = 1000\,P_{\rm b}$.

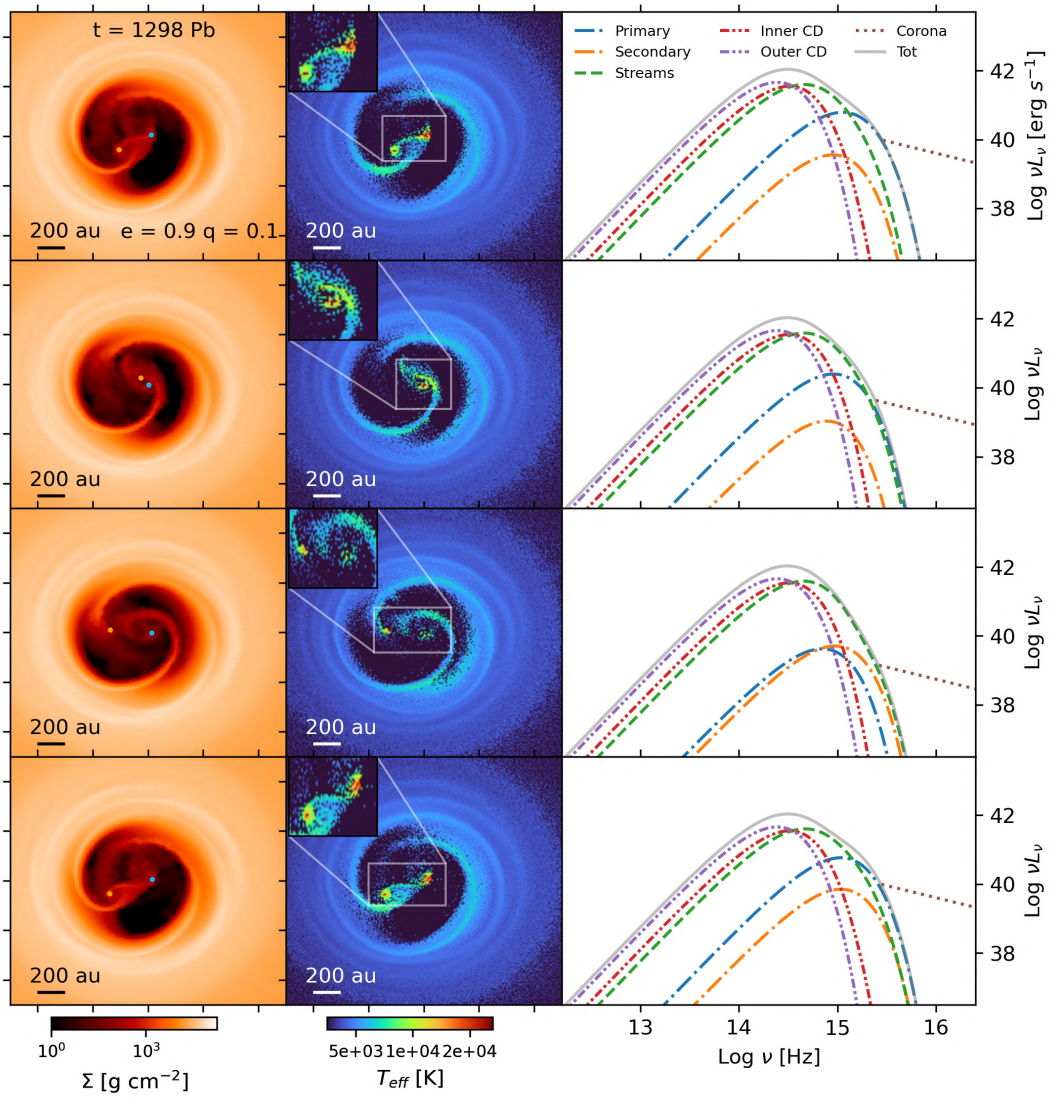

FIGURE 4.5: Same as Fig. 4.2 but for a binary with mass ratio $q = 0.1$ and eccentricity $e = 0.9$ and at time $t = 1298\,P_{\rm b}$.

and spans ~ 2 orders of magnitude in flux within one orbital period.

In the eccentric unequal-mass case (see Fig. 4.5), the mini-discs are significantly depleted as the high eccentricity of the binary causes them to strongly interact with each other and the material is either promptly accreted or flung back to the cavity wall. We note that in this case, the variability of the emission from the mini-discs is not totally hidden by the emission from the streams region but does change the spectrum at high frequencies within one orbital period.

In all of the simulations, by construction, the emission of the X-ray corona tracks that of the mini-discs, as per Eq. (2.51); therefore, depending on the simulation, it can vary by up to two orders of magnitude in luminosity.

4.2.2 Light Curves

We integrated the luminosity emitted in each disc region in order to produce the LCs, showing the flux variation in the system as a function of time. We assume the source to be at redshift $z = 0.1$ and investigate the effect of redshift on source observability in the next subsection. We have calculated the bolometric flux across the whole frequency range we used to produce the spectra ($1.0 \times 10^8 - 2.8 \times 10^{19}$ Hz or $4.13 \times 10^{-10} - 41.3$ keV) and in three different regions of the EM spectrum: in the optical, using the Rubin Observatory filters frequency bands (see Table 3.1), in the near-UV ($1.0 - 1.5 \times 10^{15}$ Hz or $4.13 - 6.20$ eV), and in the soft X-ray ($7.25 - 48.3 \times 10^{16}$ Hz or $0.3 - 2$ keV). The upcoming Rubin Observatory will perform a 10-year survey of the sky in the southern hemisphere and it will potentially be able to capture the EM emission from the accretion disc of MBHBs. We therefore focus most of our attention on the optical emission of our simulated systems, and we consider the Rubin Observatory z, i, r, and g filters (see Table 3.1 for details), and the instrument sensitivity, as is described in Sect. 3.3.4.

The results are shown in Figs. 4.6 ($e = 0$) and 4.7 ($e = 0.9$). In each panel of the two figures, the left column shows the LCs computed in all the considered bands together with the accretion rate, (grey line in the top panel), while the right column shows the FFT of the accretion rate and of the fluxes computed over 300 orbits, $t = 1000 - 1300\, P_{\rm B}$ ($t = 760 - 1060\, P_{\rm B}$ for the case $q = 0.1$, $e = 0$), normalised to unity. In the Rubin Observatory filters, the flux was computed including extra Gaussian stochastic fluctuations mimicking the effect of the Rubin Observatory sensitivity, as

is described in Sect. 3.3.4. In all cases, we see that the emission is brighter in the optical and UV band (except in the eccentric unequal case), while it is dimmer in the soft X-ray, consistent with our SEDs (see Figs. 4.2–4.5).

Indeed, in our model the only contribution that produces luminosity at high frequencies is the corona. Another clear trend shown in all simulations is that variability tends to increase with frequency. In fact, while the flux in the Rubin Observatory bands changes within a factor of 2-3, the UV and X-ray fluxes can experience oscillations of more than one order of magnitude, in particular in eccentric cases. This is consistent with the physics of the emission from the disc. The optical mostly comes from the circumbinary disc, which is relatively steady and only mildly affected by the binary. Conversely the UV emission is dominated by the streams and mini-discs, which are strongly impacted by the dynamics of the binary, and thus highly variable. Finally, the X-ray corona is directly connected to the UV emission of the mini-discs, which is the component showing the highest variability. The large amplitude variation in the UV flux that we find suggests that these systems might be identifiable by future wide-field UV facilities, such as ULTRASAT [scheduled for launch in 2027, 158] and UVEX [scheduled for launch in 2030, 159].

The left panel in Fig. 4.6 displays a number of interesting features. It is clear that the main modulation pattern is not related to the binary period, but occurs on longer timescales, and this is true both for the LCs and for the accretion rate. This is confirmed by the FFTs, which show two clear peaks at $0.2\,f_{\rm K}$ and $0.4\,f_{\rm K}$ (second harmonic), where $f_{\rm K}$ is the Keplerian frequency of the binary. This periodicity is associated with the 'lump', an over-density region that obits at the cavity edge with an orbital period a few times the binary orbital period, as reported in previous works [64, 65, 68, 71–79]. It is also interesting to notice that, while the accretion rate shows an intricate structure of harmonics [29, 37, 64], this is much less evident in the LCs, where there is significant power only at $2\,f_{\rm K}$, which corresponds to one half of the orbital period. The situation is strikingly different when the mass ratio of the binary is small (right panel in Fig. 4.6). In this case, both the accretion rate and the LCs show a clear periodicity on the binary period, which is confirmed by the FFT, where clear peaks are visible at $1\,f_{\rm K}$ and $2\,f_{\rm K}$ (second harmonic). We also note that there is no clear power at $f < f_{\rm K}$. This is because no significant lump forms in this case, since perturbations induced by the binary are not sufficient to excite an $m = 1$ mode

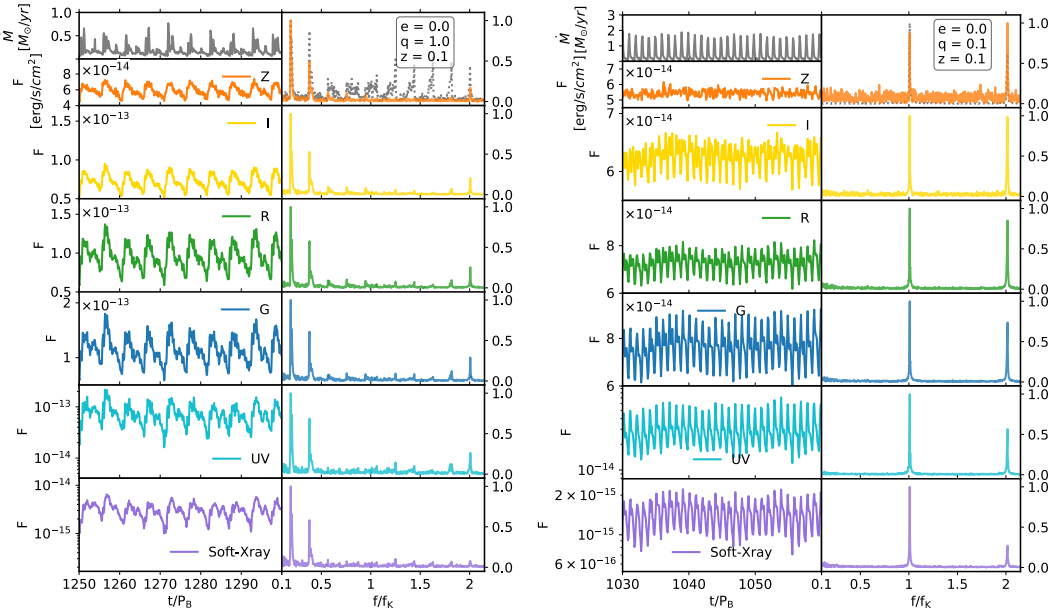

FIGURE 4.6: Light curves and their FFT for circular mass binaries at $z = 0.1$. The left and right panels are for binaries with $q = 1$ and $q = 0.1$, respectively. In each panel, the first row shows the accretion rate (grey line) and the flux (orange line) integrated over the whole frequency range we consider ($10^8 - 2.8 \times 10^{19}$ Hz). The left column shows the flux evolution in time while the right column shows the FFT of the accretion rate and flux over 300 orbits in the time window $t = 1000 - 1300\, P_{\rm B}$ (left panel) or $t = 760 - 1060\, P_{\rm B}$ (right panel), normalised to unity, in function of $\rm f/f_K$ with $\rm f_K$ the Keplerian frequency of the binary. The second, third, and fourth rows show the flux and FFT in the optical z band, UV band, and soft X-ray band, respectively. The optical flux was computed taking into account an extra Gaussian noise component, as is described in Sect. 3.3.4.

at the inner edge of the circumbinary disc cavity. This is in line with results of 2D simulations in the literature [see e.g. 64].

Results for the eccentric binary simulations are shown in Fig. 4.7. The equal-mass case (left panel) shows an interesting periodicity structure. The fluxes emitted in the optical bands all exhibit a clear modulation of a factor ≈ 2, combining periodicities related to both the binary and the lump dynamics. In the FFT, we can clearly see the lump periodicity at $f \approx 0.15 f_{\rm K}$: this is lower than the circular binary case, as the cavity is larger and the period associated with its inner edge is $\propto R^{3/2}$. Contrary to the circular equal-mass case, clear peaks are visible also at $1\, f_{\rm K}$ and $2\, f_{\rm K}$ (second harmonic), driven by the binary orbital period. In the eccentric unequal-mass case instead (right panel), the lump periodicity is absent and the peak at $f \sim 2 f_{\rm K}$ is less prominent than what was found in the circular unequal binary case. We have also explored the effect of placing the binary at different redshifts. For simplicity, we

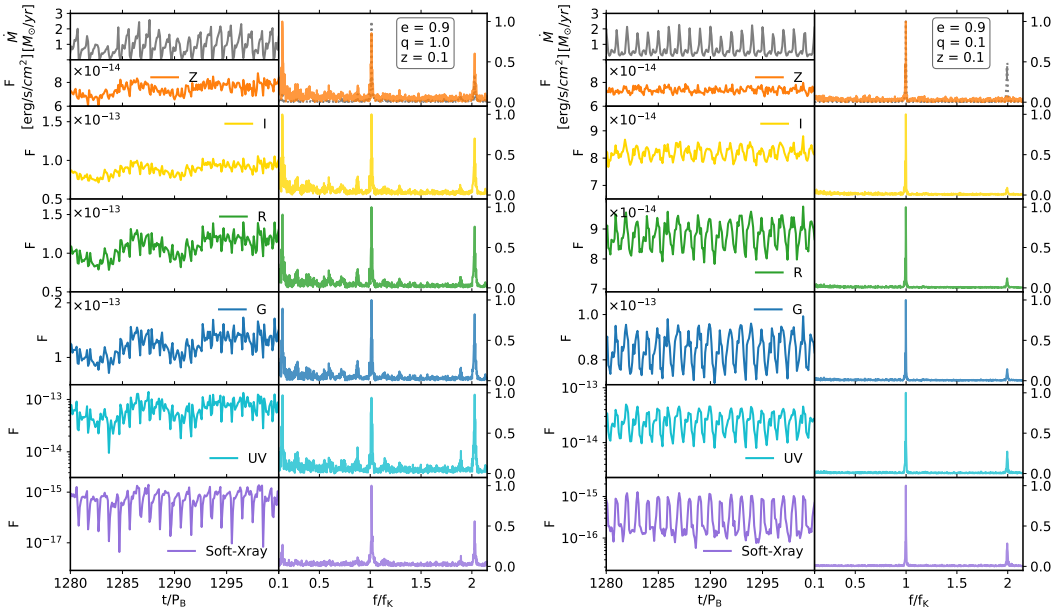

FIGURE 4.7: Same as Fig. 4.6 but for eccentric $e = 0$ binaries. Here, the Fourier transform of the accretion rate and fluxes is computed over 400 orbits in the time window $t = 900 - 1300\, P_{\rm B}$.

discuss the main results without including plots. Besides the obvious difference in flux, making closer binaries easier to detect, there is also some minor change difference in the displayed periodicities due to the redshifting of the spectra at $z < 0.6$. At redshifts of $z > 0.6$, fluxes are very noisy and periodicity peaks are not always distinguishable in all the optical bands. However, all the main features described here for binaries at $z = 0.1$ remain valid.

4.2.3 Periodicity identification in the Vera Rubin Observatory survey

We have so far computed the FFT over a large number of orbits in order to distinguish the different periodicities associated with binaries with different mass ratio and eccentricity. However, Rubin Observatory might only have a handful of binary orbits at its disposal in its 10-year observational campaign. This is because binaries with periods shorter than a few years are expected to be primarily driven by GW emission, meaning that wide binaries (with long periods) live longer and are more likely to be present in the data [see 82]. In fact, the binary period of 1 year considered here was chosen to be representative of the typical system that might be detected with Rubin Observatory.

Since we output ten snapshots per binary orbit, the cadence of our simulated light

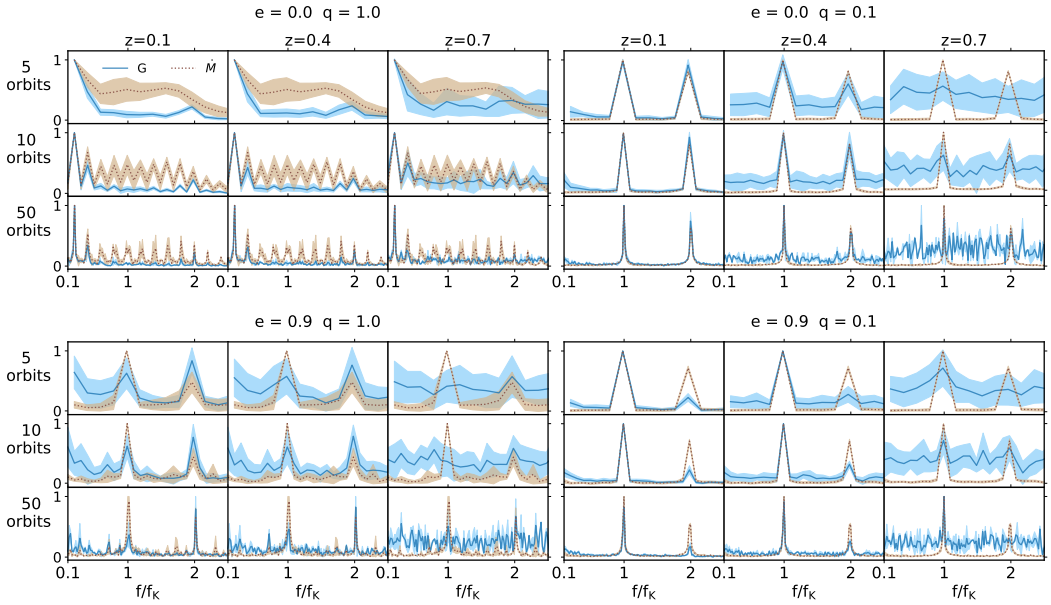

FIGURE 4.8: Fast Fourier transform of LCs from simulations. The top panels are for simulations of circular binaries, while the bottom panels are for simulations of eccentric $e = 0.9$ binaries. The left and right columns are for binaries with $q = 1$ and $q = 0.1$, respectively. The first row of each case shows the FFT of the Optical G band flux (blue line) and the FFT of the accretion rate (brown line) computed over 5-orbit windows within a total of 300/400 orbital periods at redshift z = 0.1, 0.4, 0.7. The second and the third rows show the FFT computed over 10- and 50-orbit windows, respectively.

curves is roughly 36 days. This sampling rate is sparser compared to what future Rubin Observatory surveys are expected to achieve. In fact, the Rubin Observatory Deep Drilling Fields will be covered with daily cadence, whereas in the most optimal scenario, the main Wide Fast Deep survey will get back on the same target at a roughly weekly cadence. Therefore, our simulated data miss high frequency information that, if present, might be detected in real observations. However, we stress here that our light curve sampling rate is good enough to cover periodicities occurring at the binary and at the inner disc cavity orbital frequencies, which are the most prominent signatures proposed in the literature. To get a qualitative idea of whether the periodicities found in the previous section can be identified in Rubin Observatory data, we have computed the FFT over 5, 10 and 50 binary orbits along a total of 300 orbits for the circular binary cases and 400 orbits for the eccentric binaries, essentially shifting the FFT window within these few hundred orbits. We have then computed the average FFT and its standard deviation (STD) at different redshift, $z = 0.1, 0.4, 0.7$.

In Fig. 4.8 we show the results for each of the four binaries we considered. In

each plot, the first row shows the mean FFT both of the flux in the optical g band (blue line) and of the accretion rate (brown line) using a 5-orbit window at redshift $z = 0.1, 0.4, 0.7$ from the left to the right. The second and the third rows show the results obtained with 10- and 50-orbit windows, respectively. We note that, given a Rubin Observatory survey of 10 years, 5, 10, and 50 orbits correspond to binaries with a period of two years, one year, and 2.4 months, respectively.

The main result of this exercise is that periodicities are more easily observed in unequal-mass binaries than in equal-mass ones. In fact, starting from the top left panel of Fig. 4.8, we see that periodic features in circular equal-mass binaries will be extremely hard to pick. With only 5 orbits, the lump periodicity falls in the lowest frequency bin of the Fourier decomposition and cannot be securely identified. Other periodicities are much weaker and do not show significant power in the FFT over 5 orbits. Things improve with increasing numbers of orbits and the lump periodicity clearly emerges when considering 50 orbits. Conversely, the circular unequal-mass case (top right panel) shows that the peaks at $f = f_{\rm K}$ and $f = 2f_{\rm K}$ are already prominent after only 5 orbits, which is very promising, and the situation naturally improves if more orbits are sampled.

A similar situation is observed for eccentric binaries, with periodicities that are more prominent in the unequal-mass case. There are noticeable differences though. In the equal-mass case (lower left panel), periodicities at $f = f_{\rm K}$ and $f = 2f_{\rm K}$ start to emerge already after 5 orbits. However, the variance is large, meaning that these features are not prominent and might be hard to detect. The situation naturally improves with the number of orbits, but a large variance remains, even after 50 orbits. It is also interesting to note that the lump frequency, clearly present in the circular case, does not seem to emerge here. In the eccentric unequal-mass case (lower right panel), the orbital periodicity is clearly identified already after 5 orbits, although the second harmonic is much less prominent than in the circular case.

In all cases, the variance tends to increase with redshift. This is a natural effect due to the inclusion of the Rubin Observatory sensitivity limit in the computation. In particular, the Rubin Observatory telescope could encounter substantial difficulties in detecting flux periodicities emanating from binaries with mass $M_{\rm B} \sim 10^6 M_\odot$ at redshift $z > 0.5$. This is clearly illustrated by the $z = 0.7$ panels of Fig. 4.8, where the peaks generally observable at $z = 0.1, 0.4$ tend to be swamped in the variance.

This does not necessarily mean that Rubin Observatory cannot identify LISA MBHB precursors beyond $z \approx 0.5$. In fact, the bolometric luminosity of the systems simulated here is $L_{\rm bol} \approx 10^{42}$ erg s^{-1} $\approx 0.01 L_{\rm Edd}$. The largely sub-Eddington luminosity is mainly due to the relatively low temperature of the gas, reaching only $T \approx 3 \times 10^4$K, which is a factor of a few cooler than the temperature of a standard thin disc around a $10^6\,M_\odot$ MBH [160]. This is also expected, due to the fact that $R_{\rm sink} = 0.05a \sim 100 R_{\rm ISCO}$, as mentioned in Sec. 3.3.1 and in Sec. 3.3.3, and the overall luminosity of the system might indeed be higher. We therefore explore here also the detectability of a putative brighter binary by simply multiplying the emission by a factor of 100 — that is, $L = 100 \times L_{\rm true}$ — thus preserving all the variability properties found in our simulations. Although this is not self-consistent with our simulation, we consider it a useful exercise to assess Rubin Observatory performances against light curves that could be representative of an $M = 10^6 {\rm M}_\odot$ MBHBs emitting at the Eddington luminosity, or potentially of a more massive system of $M = 10^8 {\rm M}_\odot$ but emitting at $\approx 0.01 L_{\rm Edd}$. We repeated the process described above: we analyse the FFT of the flux over 5, 10 and 50 binary orbits along a total of 300 orbits for the circular binary cases and 400 orbits for the eccentric binaries and we compute the average FFT and its STD for different redshifts $z = 1, 2, 3$. Results are shown in Fig. 4.9. Most of the features discussed for the case $L = L_{\rm true}$ are still observed, but now peaks in the FFT can be easily identified up to $z = 2$, around cosmic noon. A full statistical assessment of Rubin Observatory capabilities of correctly identifying these peaks will be the subject of future work (F.Cocchiararo et al., in prep).

4.3 Summary of the main results

In this Chapter,

we find that, after an initial phase in which the black-body cooling dominates the gas thermodynamic evolution, the disc thickens again, reaching $H/R \sim 0.08$ in the inner parts and maintaining a lower $H/R \sim 0.04$ (corresponding to a lower temperature) in the outer part of the disc, regardless of the initial choice of binary mass ratio and eccentricity. The final equilibrium state is, in fact, mostly driven by the initial disc mass and radial extension, which are the same in all simulations. Therefore, self-regulation [155] drives all discs to reach a similar aspect ratio at the end of the transient phase. We find the interaction between the binary and the circumbinary disc

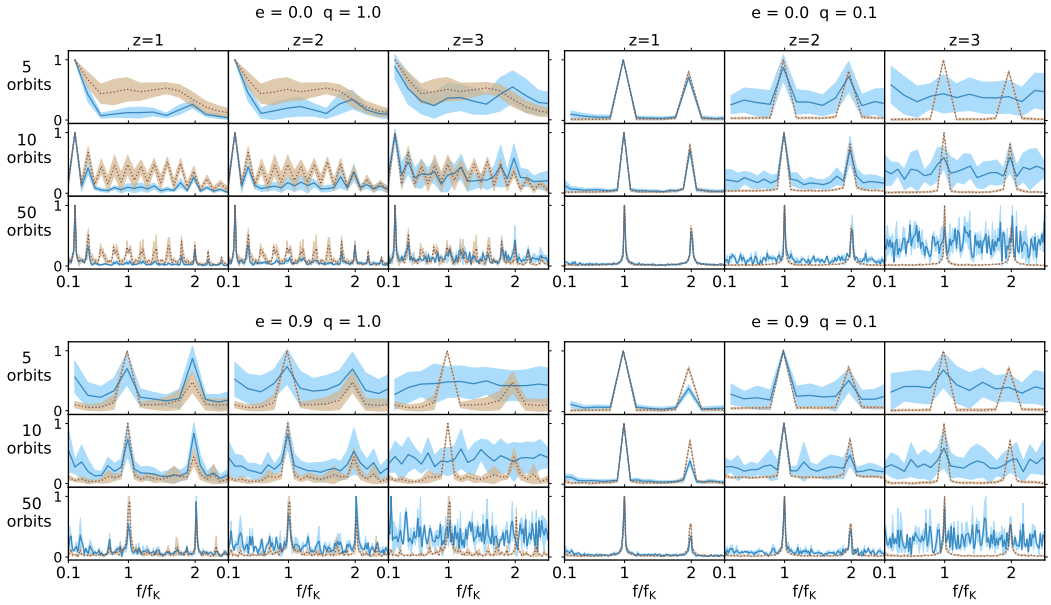

FIGURE 4.9: Same as Fig. 4.8 but assuming that the emitted luminosity is 100 times higher than the luminosity we obtained from simulations.

to cause the binary to shrink, regardless of the initial conditions. Since in our model the temperature changes with time, this result further supports previous findings in the literature [35, 67]. We find that circular orbits tend towards higher eccentricity values, in agreement with previous works [e.g. 32, 145], whereas very eccentric binaries experience a negligible eccentricity evolution within the timeframe of our simulations. We notice, however, that we followed the evolution of the relaxed disc only for about 400 orbits, corresponding to 400 years. It might be that the eccentricity evolution for very eccentric binaries occurs on a longer timescale than the one simulated here. Indeed, here we simulated the binary evolution over $\sim 1300\,\mathrm{yr}$, while in both the cited works the timescale is longer.

We computed the SEDs from the circumbinary discs in our simulations assuming black-body emission. We find that the luminosity emitted by the innermost region of the disc — the mini-discs and the streams — exhibits more variability than the outer parts of the disc. In the circular equal-mass case, the emission peak of the mini-discs and the streams region changes frequency between the optical and UV band ($\log(\nu/\mathrm{Hz}) \sim 14.8 - 15.4$), spanning one order of magnitude in luminosity. In the unequal-mass case, the mini-discs have a lower temperature due to the absence of shocks produced by the exchange of material among the binary components. Thus, the emission peak of the mini-discs is shifted to slightly lower frequencies —

$\log(\nu/\mathrm{Hz}) \sim 14.8 - 15.2$ — and spans up to ~ 2 orders of magnitude in luminosity. In both the eccentric binary cases, we find that the emission from the mini-discs is completely (in the equal-mass case) or partially (in the unequal-mass case) covered by the streams emission. The X-ray photons are provided by the corona, which we assume to have an emission proportional to that of the mini-discs. Therefore, the luminosity in the X-ray band displays the highest variability, which can reach up to two orders of magnitude for unequal-mass binaries.

We computed the LCs in different frequency bands, mainly focussing on the optical window that will be probed by Rubin Observatory. We calculated the (thermal) flux emitted over the whole EM spectrum that we used to produce the SEDs, in the optical frequency band using the Rubin Observatory filters, in the near-UV band, and in the soft X-ray band.

In almost all cases, the flux is notably higher in the UV band, while in the soft X-ray is dimmer, consistent with the shape of the SEDs. As the frequency increases, the flux variability grows, in particular in the UV and soft X-ray bands. Here, the flux oscillates by more than an order of magnitude, while in the Rubin Observatory optical bands fluxes vary within a factor of two, in line with the physics of emission from the disc.

In the circular equal-mass case, both the flux and the accretion rate FFTs reveal clear peaks at $0.2\,f_{\rm K}$ and $0.4\,f_{\rm K}$ associated with the lump periodicity. Moreover, in the LCs, a peak at $2\,f_{\rm K}$ is also present, which corresponds to a periodicity of one half the binary orbital period. In the eccentric equal-mass case, the lump periodicity is significant only in the optical and UV fluxes, while its amplitude is negligible in the soft X-ray band. This is probably due to the larger cavity carved by the binary, which causes the lump region to emit in the optical/UV band rather than in the soft X-ray band. We indeed found the lump modulation peak to be shifted to $f_{\rm K} \sim 0.15$. This is consistent with the fact that the cavity is larger than in the circular equal-mass case since the period associated with its inner edge is $\propto R^{-3/2}$. We note that we found evidence of lump periodicity only in equal-mass binaries. This is consistent with previous works that show the lump modulation amplitude to decrease with binary mass ratio [78]. Therefore, a lack of sub-orbital modulation in the presence of a clear orbital modulation might indicate a small binary mass ratio. We also found a prominent flux and accretion rate modulation over the orbital period of the binary

and half of it in all the simulations, with the exception of the circular equal-mass case, which shows a a weak periodicity only at $2\,f_{\rm K}$. By exploring different redshifts, there are some minor change in periodicities at a redshift of $z < 0.6$, while at higher redshifts fluxes are very noisy and the periodicities are not always well distinguished.

All the aforementioned considerations are valid when the FFT is computed over a large number of binary orbits (i.e. $300 - 400\,P_{\rm B}$). However, the Rubin Observatory survey is planned for 10 years and most compact MBHBs are expected to have periods of ≈years. Therefore, we have computed the FFT of the flux and of the accretion rate over 5, 10, and 50 binary obits at different redshifts to make a more realistic assessment of the prominence of these periodicities in the Rubin Observatory data. In the circular equal-mass case, detecting periodicities is challenging, in particular with only five orbits. We found that, as the number of orbits used to compute the FFT increases, the periodicities become more distinct and the associated variance decreases, as was expected. Still, the identification of equal-mass, circular binaries appears to be the most challenging. Conversely, binaries with $q = 0.1$ show promising results, with distinguishable peaks at $1\,f_{\rm K}$ and $2\,f_{\rm K}$ even after five orbits. Similar trends are observed in eccentric cases. The lump periodicity is totally absent in all cases except for the circular equal-mass case, which shows a hint of lump periodicity when computing the FFT over 50 orbits. Thus, the chances of detecting it during a 10-year survey by assuming unequal MBHB with an orbital period of 1 year are negligible.

Due to the intrinsic faintness of our system, $L_{\rm bol} \approx 10^{42}$ erg s^{-1}, the detectability of periodicities with Rubin Observatory are limited to systems at $z < 0.5$. As an exercise, we increased the luminosity of all our systems by a factor of 100, mimicking a MBHB of $M = 10^6 {\rm M}_\odot$ emitting at the Eddington limit. We found that in this case, periodicities can be identified by Rubin Observatory up to $z \approx 2$, opening the possibility of finding these systems in a large fraction of the co-moving volume of the Universe.

Our results show that periodic variability arising from unequal-mass binaries is generally easier to detect in Rubin Observatory observations than in equal-mass systems. Moreover, binaries with different physical configurations (e.g., as mass ratio and eccentricities) produce distinct light curve modulations. This suggests that time-domain EM observations could be used to infer key binary properties. Such EM signatures

are highly relevant in the context of future multi-messenger studies. Observations from Rubin Observatory can provide valuable input for upcoming low-frequencies GWs missions such as LISA and PTAs. In particular, Rubin Observatory may help identify potential LISA progenitors and provide priors on their mass ratios, eccentricities and environments. The combination of EM and GW information will offer a powerful tool to test theoretical models of MBHBs formation and evolution.

In this chapter, we present advanced 3D simulations that improve the description of accreting MBHBs embedded in gaseous discs, which is fundamental in order to make more realistic predictions of the emission signatures of these sources. We note here that we included the effect that radiation pressure has in determining the gas temperature only a posteriori. In the following chapters, we discuss how the radiation pressure implementation in simulations affects both the disc and binary evolution (Chapter 5) and EM signatures of these systems (Chapter 6).

Chapter 5

The role of radiation pressure in accreting massive black hole binaries

Based on:

F.Cocchiararo, A.Franchini, A.Lupi, A. Sesana,

"Radiation pressure role in accreting massive black hole binaries", 2025, submitted to A&A, DOI, ADS link

---

A critical aspect that has often been neglected in previous studies is the role of radiation pressure in the hydrodynamics evolution of the circumbinary disc. Previous works have already performed radiation-MHD simulations [138, 139], in both their Newtonian [161, 162] and GR versions [163], around a single BH as well as in the study of tidal disruption events [164, 165]. At sub-parsec scales discs are likely dominated by radiation pressure; therefore, including this additional term in the hydrodynamics equations is very important in order to advance the theoretical modelling of the MBHB-disc interaction. Radiation pressure plays an important role in the hotter inner regions of the disc, where it significantly affects the gas dynamics, potentially modifying its geometry - including its aspect ratio, cavity shape and eccentricity - and therefore altering the inflow of gas towards the binary. Correctly modelling the inflow of gas inside the cavity is fundamental as this affects the gravitational and accretion torques on the binary, the accretion rate and therefore the evolution of the binary orbital parameters, i.e. semi-major axis and eccentricity.

In this chapter, we evaluate the impact of radiation pressure on the evolution of circumbinary discs around MBHBs for different values of the binary initial mass ratio and eccentricity. Building on our previous simulations presented in Chapter 4, we implement the contribution of the radiation pressure in our 3D numerical simulations with hyper-Lagrangian refinement and consider milli-parsec scale binaries. The simulations also account for the thermodynamics evolution of the gas using a radiative cooling prescription in the form of black-body radiation. We have also included the self-gravity of the disc and the Shakura-Sunyaev prescription for viscosity.

We explore the time evolution of the binary and disc properties for three values of the binary eccentricity $e = 0, 0.45, 0.9$ and mass ratio $q = 0.7, 1$. We compare the evolution of the disc and binary orbital parameters with the simulations that included only gas pressure in order to isolate the effect of radiation pressure.

We describe the numerical details of the simulations, how we implemented the radiation contribution to the total pressure, the physical parameters we use, and the circumbinary disc assumptions in Sections 3.3. We here show and discuss the main results we obtain, including the time evolution of the main binary and disc properties. Finally, we report our conclusions.

5.1 Disc evolution

For a more comprehensive physical understanding of circumbinary discs evolution, it is essential to account for radiation pressure, which, while is often included in GRMHD simulations [80, 138–140], is usually neglected in studies of binaries at large separations. Its effect is particularly important in the hot inner regions of the disc, where it can significantly alter the gas dynamics, the disc geometry, and ultimately influence the inflow of material toward the binary. Figure 5.1 shows the surface density maps in the $x - y$ plane for the simulations with $e = 0$ and $q = 1$ (upper panel), $e = 0.45$ and $q = 0.7$ (middle panel), and $e = 0.9$ and $q = 1$ (bottom panel) respectively, at $t = 1$, 900, 1300 $P_{\rm B}$ for the un-equal mass binary, and $t = 1$, 900, 1600 $P_{\rm B}$ for the equal mass binaries. In order to highlight the radiation pressure effect, we show, in each of the three panels, the same simulation which includes only the gas pressure contribution in the upper row.

The first noticeable effect of radiation pressure is to inhibit the cavity eccentricity

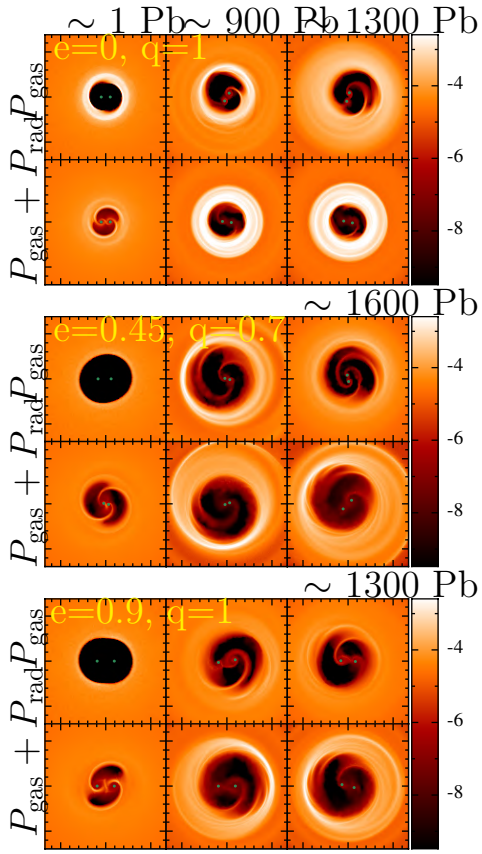

FIGURE 5.1: Surface density map in code units (1 code unit = 200 AU) in the $x-y$ plane for the simulations with e=0 q=1 (upper panel), e=0.45 q=0.7 (middle panel), and e=0.9 q=1 (bottom panel), at three different moments: $t = 1$, 900, 1300 $P_{\rm B}$ for the equal mass cases and $t = 1$, 900, 1600 $P_{\rm B}$ for the unequal mass case. In each panel, the first and the second row show results for $P_{\rm tot} = P_{\rm gas}$ and $P_{\rm tot} = P_{\rm gas} + P_{\rm rad}$, respectively. In both the eccentric simulations, the initial cavity radius is $3a_0$, while in the circular binary case it is $2a_0$. When the radiation pressure is included, the binary begins accreting at the very early stages of its evolution, otherwise the disc experiences a transient phase lasting approximately 900 $P_{\rm B}$, 700 $P_{\rm B}$ and 600 $P_{\rm B}$ for the case e=0 q=1, e=0.45 q=0.7 and e=0.9 q=1, respectively. The spatial resolution at the edge of the cavity ($r = 3a$) is $\Delta x = 0.025a$.

growth, particularly in the circular equal mass binary case. The simulation with the circular equal mass binary and the implementation of radiation pressure shows a region of enhanced density in the inner part of the disc that extends up to $R \sim 5a$. This feature persists also after $t = 1300\,P_{\rm B}$. In the eccentric binary cases, the presence of radiation pressure results in a denser over-density at the cavity inner edge. This feature, called "lump", has been previously found in the literature in circumbinary discs around close-to-equal-mass binaries and it is the result of the combination of the flung-back streams impacting on the cavity edge and of the disc eccentricity [64, 73, 89, 141]. In the radiation pressure case, the dense region that forms in the equal mass circular binary case possibly hinders the formation of the lump.

With our 3D simulations that include time dependent thermodynamics, we are able to resolve shocks arising from gas streams that are flung back into the cavity inner edge. These shocks do indeed affect the inner disc thickness and temperature. The radiation pressure contribution can also play a role in this process, potentially influencing the disc structure.

Figure 5.2 shows the time evolution of the surface density, disc aspect ratio H/R, the midplane temperature, and the effective temperature $T_{\rm eff}$ as a function of the radius R for all our simulations, at four different times. We compute the aspect ratio of the disc following Eq. 4.1. In all our simulations, for each gas particle i, we obtained the temperature T_i numerically solving the total pressure equation Eq. 3.2.

We divide the disc temperature domain into a 2D matrix in the x-y plane, corresponding to the binary orbital plane. For each pixel, the midplane temperature is calculated by averaging the temperatures of all the particles within the vertical range $-0.05a < z < 0.05a$, obtaining the midplane temperature matrix T. Finally, we calculate the effective temperature in the optically thick approximation ($\kappa\Sigma > 1$) as reported in Eq. 3.3.

Since the Toomre parameter is $Q > 1$, the disc tends to cool down in order to reach a self-regulated state with $Q \sim 1$. Regardless of the inclusion of the radiation pressure contribution, during the first $\sim 400\, P_{\rm B}$, the cooling leads to a decrease in the disc aspect ratio to $H/R \sim M_{\rm B}/M_{\rm D} \sim 0.01$. When radiation pressure is neglected, the disc still experiences this cooling phase but the aspect ratio increases again after 900 orbits, settling at a much higher value, around 0.07. This evolution of the disc aspect ratio is driven by the change in midplane temperature of the disc. As we can see from the third raw of Figure 5.2, the midplane temperature initially decreases and then increases again, causing the vertical expansion of the disc. On the contrary, if radiation pressure is included, the midplane temperature decreases and does not increase again. The disc aspect ratio therefore remains at around $H/R \sim 0.02$, except for the very inner parts of the disc that are influenced by the effect of the stream shocks. Since the disc is initially completely radiation pressure dominated, the cooling dominates over heating, causing the disc vertical collapse. This behaviour is consistent with what was found in [138], in [139] and in [80]. During this cooling phase, the surface density increases in both the radiation pressure and gas pressure only runs and regardless of the binary mass ratio and eccentricity. In the simulations

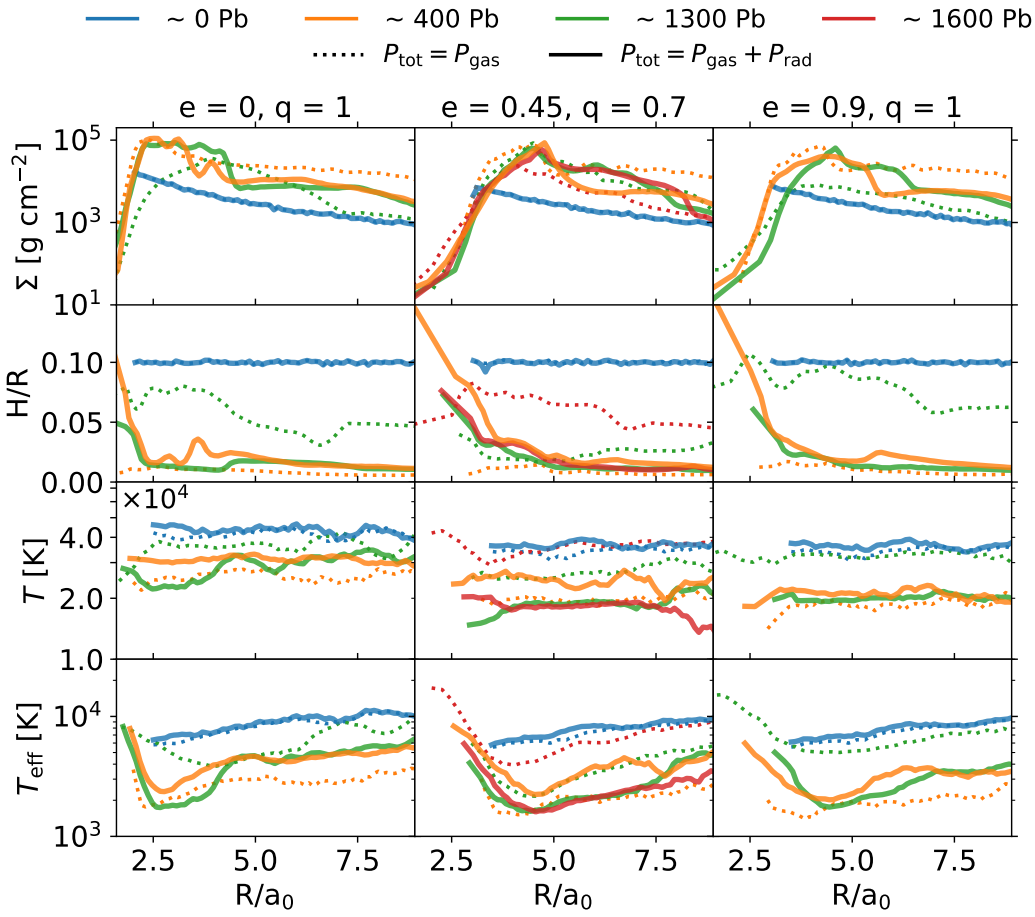

FIGURE 5.2: Time evolution of the surface density (first row), disc aspect ratio H/R (second row), the midplane temperature (third row), and the effective temperature (last row) as a function of radius for the binary case $e = 0$ $q = 1$ (first column), $e = 0.45$ $q = 0.7$ (central column), and $e = 0.9$ $q = 1$ (last column), at different times distinguished by different colours. The solid and dashed lines refers to the simulation without and with the implementation of the radiation pressure, respectively. The initial condition of the disc is the the same across all the cases, except the initial cavity radius that is $3a_0$ in both the eccentric simulations, while it is $2a_0$ in the circular binary cases. We calculate the midplane temperature and the effective temperature assuming that both the gas and the radiation pressure contribute to the hydrostatic equilibrium of the disc in all the cases. The radiation pressure contribution leads the disc to maintain a lower aspect ratio and temperature.

that include the radiation pressure effect, the surface density reaches a stable profile on a shorter timescale. This possibly implies that the additional vertical support provided by the radiation pressure rapidly regulates both the thermal balance and geometrical structure of the disc. The effective temperature decreases from initial values between $T_{\rm eff} \sim 6 \times 10^3 - 10^4\,K$ to $T_{\rm eff} \sim 1.5 - 7 \times 10^3\,K$, the hottest region lying, as expected, within $R \lesssim 2.5 - 3\,a_0$. The final effective temperature of the disc inner edge in the simulations with radiation pressure is $\sim 2 - 3 \times 10^3 K$, a factor at most 3 lower than the simulations that neglect the radiation pressure contribution. Consistently with the evolution of the disc aspect ratio, the effective temperature remains lower in the simulations that include the effect of radiation pressure.

5.2 Binary evolution

In the previous section we have shown that the radiation pressure has a non-negligible effect on the thermal properties of the disc inner edge, which ultimately regulates how much material is able to enter the cavity and accrete onto the binary. The radiation pressure contribution to the hydrostatic equilibrium of the disc does also affect the migration of material from the outer to the inner regions of the circumbinary disc. This could result in a different contribution of the accretion torque $\mathbf{L}_{\rm acc}$ to the total angular momentum equation, potentially changing the binary fate. Indeed, conservation of angular momentum in our simulations implies that

$$\frac{d\mathbf{L}}{dt} = \mathbf{T}_{\rm grav} + \frac{d\mathbf{L}_{\rm acc}}{dt}, \tag{5.1}$$

where $\mathbf{L}$ is the total binary angular momentum and $\mathbf{T}_{\rm grav}$ is the gravitational torque (i.e., $d\mathbf{L}_{\rm grav}/dt$). The contribution from the accretion of gas particles onto the two binary components - $\mathbf{L}_{\rm acc}$ - and the contribution of the gravitational torque exerted by the disc elements onto each individual MBH - $\mathbf{T}_{\rm grav}$ -, determine whether the binary orbit shrinks or expands as a result of the interaction with the circumbinary disc [137].

We compute the gravitational torque exerted by N gas particles on each binary component as

$$\mathbf{T}_{\rm grav} = \sum_{k=1}^{2}\sum_{i=1}^{N} \mathbf{r}_{\rm k} \times \frac{GM_{\rm k}m_{\rm i}(\mathbf{r}_{\rm i}-\mathbf{r}_{\rm k})}{|\mathbf{r}_{\rm i}-\mathbf{r}_{\rm k}|^3}, \tag{5.2}$$

where m_i and $\mathbf{r_i}$ are the the mass and the position of the gas particle i, M_k and $\mathbf{r_k}$ are the mass and the position of the sink particle k. Both the gas particles and MBHs position vectors are computed with respect to the centre of mass of the system. The accretion torque can be computed as

$$d\mathbf{L}_{\rm acc} = \mathbf{r}_i \times m_{\rm i}\mathbf{v}_{\rm i} - \frac{m_{\rm i}M_{\rm k}}{m_{\rm i}+M_{\rm k}}[(\mathbf{r}_{\rm i}-\mathbf{r}_{\rm k})\times(\mathbf{v}_{\rm i}-\mathbf{v}_{\rm k})], \tag{5.3}$$

where $\mathbf{r_i}$, $\mathbf{v_i}$, and m_i are the position, velocity and mass of the accreted particle i, while $\mathbf{r_k}$, $\mathbf{v_k}$, and M_k are the position, velocity and mass of the sink k. We calculate the cumulative variation of the binary angular momentum over the entire duration of the simulations as

$$\Delta\mathbf{L} = \sum_{dt}(\mathbf{T}_{\rm grav}dt + d\mathbf{L}_{\rm acc}), \tag{5.4}$$

where dt is the time step between two consecutive snapshots.

Figure 5.3 shows the cumulative change in angular momentum in our six simulations. We note that we can self-consistently prove that we conserve the angular momentum as we evolve a live binary and are therefore able to track its orbital parameters evolution. Indeed, since our binaries are live, we can compute the evolution of the their semi-major axis a and eccentricity e directly from the simulation, using the BHs orbital energy and angular momentum at each time-step. We compute the (instantaneous) evolution of the semi-major axis and eccentricity from the binary energy and angular momentum. In particular, we measure the binary energy directly from the simulations, using

$$E(t) = \frac{1}{2}\mu(t)|\mathbf{v}|^2 - \frac{GM(t)\mu(t)}{|\mathbf{r}(t)|} \tag{5.5}$$

where μ is the binary reduced mass, and we then compute its eccentricity

$$e(t) = \sqrt{1 + \frac{2E(t)L^2(t)}{G^2M^2(t)\mu^3(t)}}\,, \tag{5.6}$$

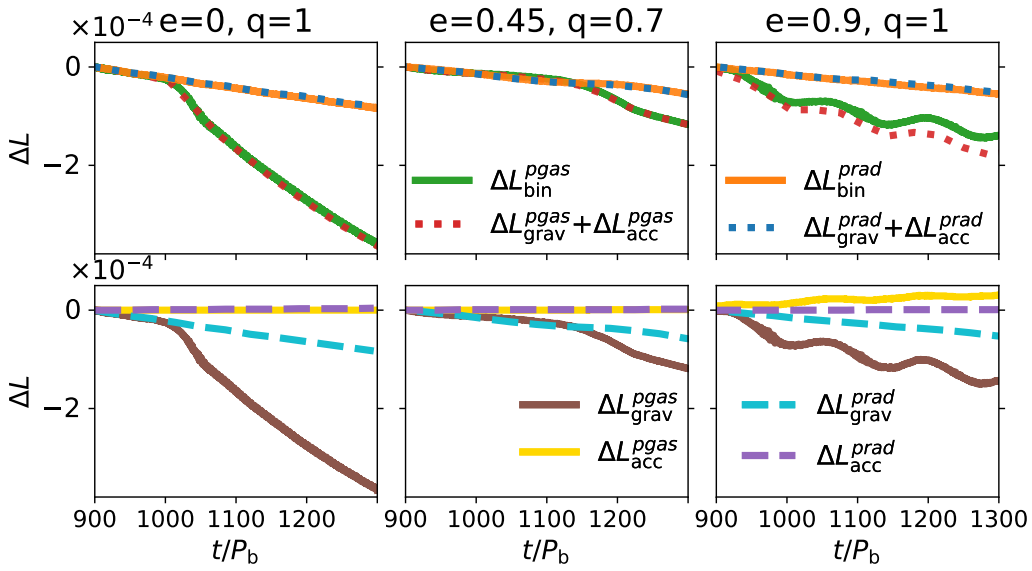

FIGURE 5.3: Angular momentum conservation for all our 6 simulations: three with gas-pressure-only and three with the addition of radiation pressure. The first column shows the circular equal mass binary simulations, the middle column shows binaries with $e = 0.45$ and $q = 0.7$ and the right column shows equal mass highly eccentric binaries with $e = 0.9$. The brown and yellow lines show the gravitational and accretion torque contributions and their sum is shown with the dotted red line for the gas-pressure-only simulations. The green line represents the binary angular momentum as measured directly from the simulation. For simulations that include radiation pressure the same quantities are plotted in dashed cyan (gravitational torque), dashed purple (accretion torque), dotted blue (sum of gravitational and accretion contribution), and orange (binary angular momentum calculated directly from the live evolution)

and semi-major axis

$$a(t) = \frac{L^2(t)}{GM(t)\mu^2(t)(1-e^2(t))}\,. \tag{5.7}$$

Regardless of the binary properties or the implementation of radiation pressure, the total angular momentum is conserved, with only minor fluctuations in the $e = 0.9$ $q = 1$ binary case. In all the simulations, the negative gravitational torque dominates and the total angular momentum variation is $\Delta\mathbf{L} < 0$, which means that the binary undergoes orbital contraction. In particular, in the circular cases, the accretion torque contribution to the total angular momentum evolution is nearly negligible. Indeed, even if $\Delta\mathbf{L}_{\rm acc} > 0$, this positive contribution is not sufficient to counterbalance the stronger negative gravitational torque, resulting in net angular momentum loss. We find a similar evolution in the medium eccentric case $e = 0.45$. In the more eccentric case $e = 0.9$, even if in the gas-pressure-only simulation the accretion contribution is higher than in the other cases, the negative gravitational torque still dominates and the binary loses angular momentum. The inclusion of radiation pressure does not change the binary fate: the net negative torques lead the binary to inspiral. These results are in agreement with those in [129], where the negative gravitational torque contribution dominates the positive accretion torque whenever the circumbinary disc aspect ratio is small enough.

Figure 5.4 shows the time evolution of the semi-major axis, eccentricity and accretion rate over time for all our simulations. We observe that, in all the cases, the binary either undergoes orbital contraction or stalls. In the circular case, the presence of radiation pressure slows down the binary inspiral. This is consistent with the fact that the accretion torque component $\Delta L_{\rm acc}$ is slightly stronger in the simulations with radiation pressure. In the moderate eccentric case $e = 0.45$, after a transient phase of ~ 300 orbits, the semi-major axis is still approximately equal to 1. In the highly eccentric case $e = 0.9$, we find orbital contraction regardless of the presence of radiation pressure. However, in the radiation pressure case, the binary shrinks between $900 - 950$ orbital periods and then stabilises, maintaining a nearly constant semi-major axis around ~ 0.997. Without the radiation pressure, the semi-major axis decreases and still reaches value ~ 0.997, but with some oscillations.

In the initially circular binary, the eccentricity e experiences a slight increase, reaching

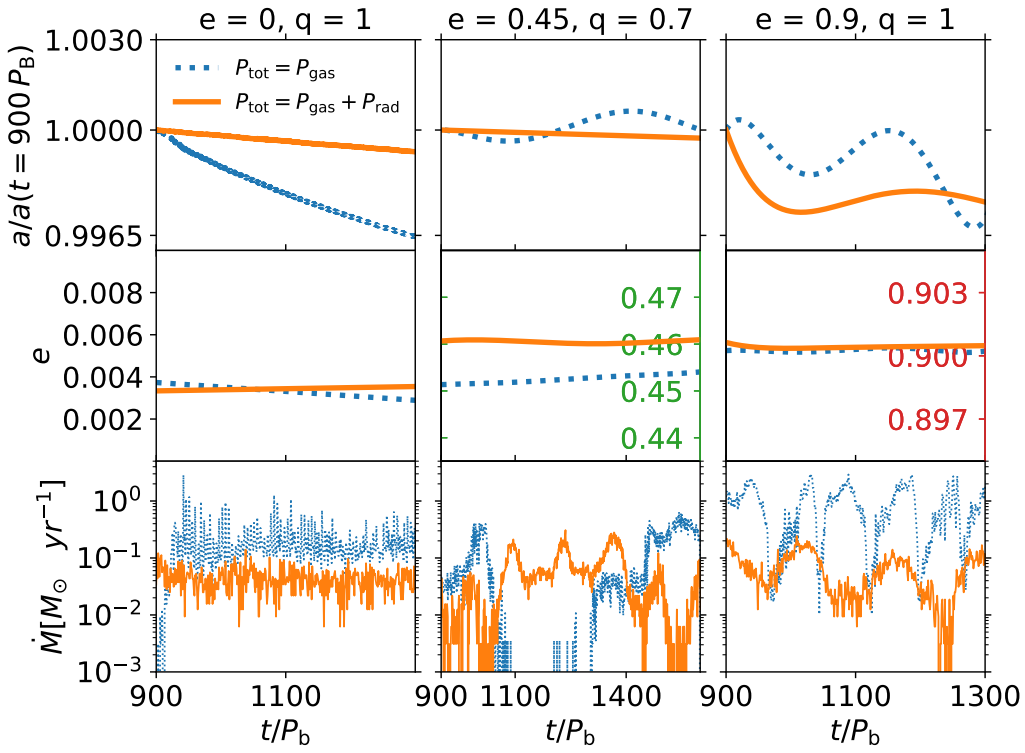

FIGURE 5.4: Time evolution of the semi-major axis (top panel), eccentricity (centre panel) and accretion rate (bottom panel) over the last 400 orbital periods for the binary case e=0 q=1 (first column) and e=0.9 q=1 (last column), and over the last 700 orbital periods for the binary case e=0.45 q=0.7 (central column). The orange and the blue lines refer to the simulation with and without the radiation pressure contribution, respectively. The semi-major axis is normalised to set $a(t = 900\,P_B) = 1$. since this is the point where our binaries start to accrete material.

values of ~ 0.003, independent of radiation pressure presence. In the $e = 0.45$ case, the eccentricity increases marginally to $e \sim 0.46 - 0.47$, while with $e = 0.9$ the eccentricity remains essentially constant. We therefore do not find a unique value at which the binary eccentricity saturates.

The accretion onto the binary is generally lower in the presence of radiation pressure, except during a transient phase of $\sim 400\, P_{\rm B}$ in the middle eccentric case. This result is consistent with the fact that the disc is geometrically thinner and colder, as shown in previous work [127, 132], if we include radiation pressure in our simulations, see Figure 5.2. The radiation pressure contribution causes the accretion rate to decrease from values $\gtrsim \dot{M}_{\rm edd}$ to average values between $\dot{M} \sim 0.1 - 0.01\, M_{\odot}/{\rm yr}$. This result is consistent with what found in [80] and in [81], where radiation pressure contribution decreases the accretion rate from $1\, \dot{M}/\dot{M}_{\rm edd}$ to $0.1\, \dot{M}/\dot{M}_{\rm edd}$ for a circular equal and unequal mass binaries with total mass $\sim 10^7\, M_{\odot}$.

5.3 Interplay between disc shape and binary preferential accretion

We here investigate the radiation pressure effect on the disc morphology and how this can reflect on the accretion of gas onto the binary components. We can see from Fig. 5.1 that, during the binary evolution, the cavity becomes more eccentric when radiation pressure is excluded from simulations. Additionally, the precession of the cavity also appears to be different between simulations with and without radiation pressure.

In order to compare the evolution of the cavity eccentricity and its precession under different conditions and binary configurations, we compute the Laplace-Runge-Lenz eccentricity vector for each gas element i:

$$\mathbf{e}_{\rm i} = \frac{|\mathbf{v}_{\rm i}|^2 \mathbf{r}_{\rm i} - (\mathbf{v}_{\rm i} \cdot \mathbf{r}_{\rm i})\mathbf{v}_{\rm i}}{G M_{\rm B}} - \hat{\mathbf{r}}_{\rm i}. \tag{5.8}$$

Following this definition, we compute the orbital eccentricity as:

$$|\mathbf{e}| = \sqrt{e_{\rm x}^2 + e_{\rm y}^2}, \tag{5.9}$$

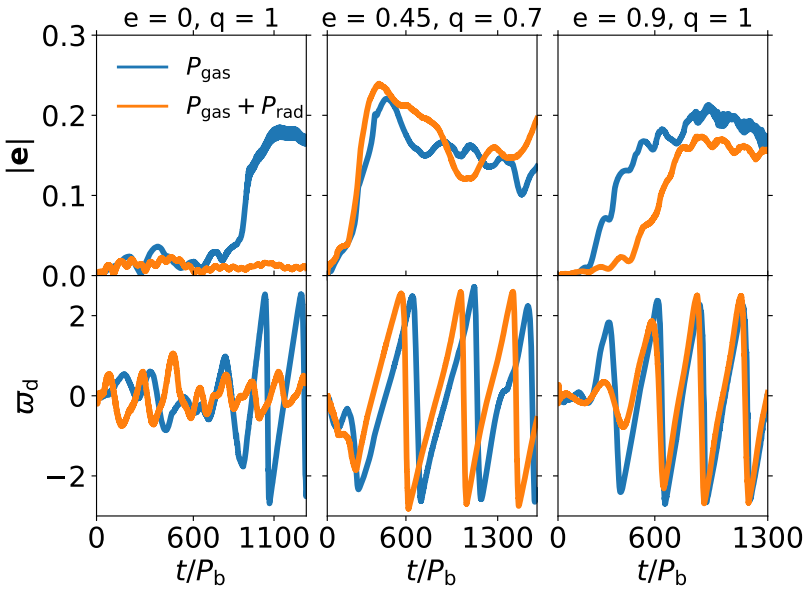

FIGURE 5.5: Eccentricity vector evolution over time for the simulations with $e = 0$, $q = 1$ binaries (left column), $e = 0.45$, $q = 0.7$ binaries (centre column), and $e = 0.9$, $q = 1$ binaries (right column). The top panels show the magnitude and the bottom panels show the phase in radians. The orange and blue lines refer to the simulation with and without the radiation pressure contribution, respectively.

where e_x and e_y are the Cartesian component of the vector. We determine the longitude of the pericenter of the disc ϖ_d as

$$\varpi_d = \arctan \frac{e_y}{e_x}. \tag{5.10}$$

We compute the mass weighted eccentricity vector between $r = a$ and $r = 4a$ of all the gas elements with a bound orbit (e.i. $E_i < 0$) over 1300 and 1600 orbital periods, for the equal and unequal mass simulations, respectively.

Figure 5.5 shows the evolution of the disc eccentricity magnitude (top panels) and the longitude of pericentre (bottom panels) for the six simulations. The orange and blue lines refer to the simulations with and without the implementation of radiation pressure, respectively. In the circular binary case, when the radiation pressure contributes to the hydrostatic equilibrium of the disc, the cavity remains circular and the precession is not significant, unlike in the case without the radiation pressure. In the eccentric binary cases, the radiation pressure effect is less dramatic and the disc cavity becomes eccentric and undergoes precession. The evolution of the the cavity eccentricity is similar in both simulations, with and without the radiation pressure.

This suggests that radiation pressure has an important effect in counteracting cavity eccentricity growth and precession in circular equal mass systems. While the effect of radiation pressure is to significantly reduce the disc temperature and locally isothermal simulations find more eccentric cavities for colder discs, we do not find any disc eccentricity growth in our circular binary simulation in the presence of radiation pressure. The main difference is indeed the inclusion of radiation pressure in our work but we caution that in order to pinpoint the exact origin of this eccentricity suppression we would need to carry out more of these expensive simulations in order to investigate the dependence of this result from the choice of initial conditions of the circumbinary disc. We note that a similar result was also obtained with radiation MHD simulations at smaller binary separations [80, their Fig. 9].

We investigate how the precession of the binary with respect to the precession of the cavity affects the accretion dynamics. In fact, the angle between the the binary eccentricity vector and the disc cavity eccentricity vector plays a crucial role in determining the amount of preferential accretion experienced by each binary component [131, 145, 166]. When this angle settles to a nearly constant value over time, due to synchronised precession between the binary and the disc, we refer to it as locking angle. In particular, [131] showed that non-zero locking angles which depend on both the binary mass ratio and eccentricity, can enhance or dampen preferential accretion: apsidal misalignment between the binary and the cavity eccentricity vectors, especially at higher eccentricities ($e_{\rm B} > 0.6$) may reduce accretion efficiency, slowing mass ratio growth; conversely, apsidal alignment at lower eccentricities leads to more efficient accretion, promoting mass ratio equalisation.

We compute the alternation of the accretion rate onto each black hole and the preferential accretion ratio $\lambda = \dot{M}_2/\dot{M}_1$ across all the binary configurations, with and without the implementation of radiation pressure. The results are shown in the first two rows of Fig. 5.6.

For the circular equal mass system, the accretion onto the binary components tends to be symmetric. We indeed find $\lambda = 1$, both with and without the implementation of radiation pressure, consistent with the expected value from the empirical relation $\lambda_{\rm fit} = q^{-0.9}$ [30] and in agreement with previous gas-only works [e.g., 30, 34, 64, 129]. For the highly eccentric equal mass binaries $e = 0.9$ $q = 1$, we obtain $\lambda = 1.2$ and $\lambda = 0.98$ with only gas pressure and with radiation pressure, respectively, broadly

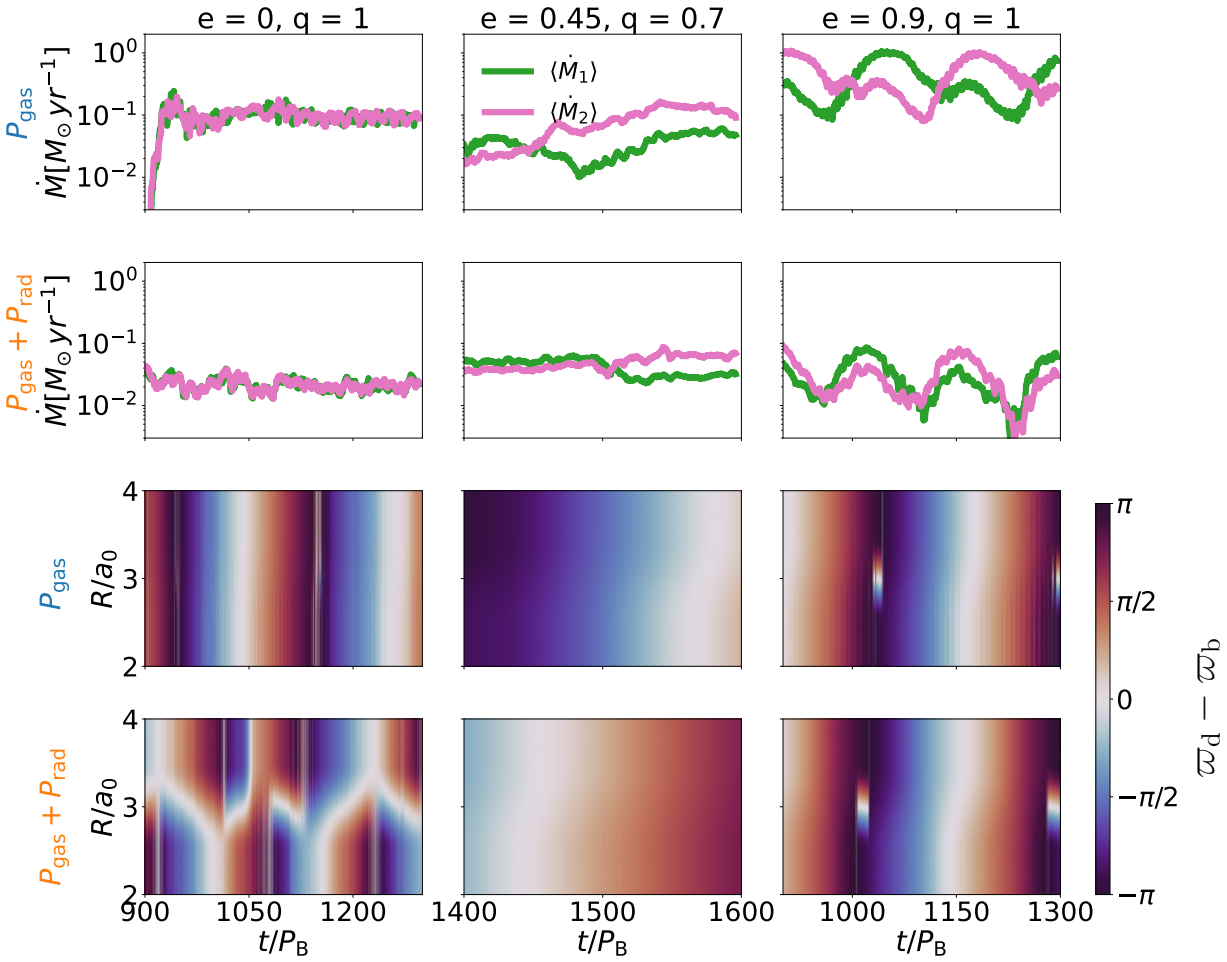

FIGURE 5.6: Time evolution of the individual accretion rate (first and second row) and the relative precession phase between the disc and the binary $\varpi = \varpi_{\rm d} - \varpi_{\rm b}$ (third and last row), for the equal mass circular case $e = 0$ $q = 1$ (left column), $e = 0.45$ $q = 0.7$ (middle column), and the equal mass highly eccentric one $e = 0.9$ $q = 1$ (right column). The first two rows show the accretion onto the primary (green line) and the secondary (pink line) black hole, over over the last 400 and 200 orbits for the equal and unequal mass cases, respectively. The upper row shows the results of simulations without the radiation pressure, while the second row includes the radiation pressure. The third and last row display the evolution of the relative precession phase over the radius. The third row shows results without radiation pressure, and the last row includes it. For $e = 0.45$ a transient locking between the disc and the binary eccentricity vectors emerges, leading to episodes of preferential accretion.

consistent with [131].

The most interesting regime to investigate is the unequal mass binary case as prolonged preferential accretion is expected to occur in unequal mass systems. In the intermediate eccentricity unequal mass case, we find $\lambda = 2.28$ and $\lambda = 1.18$ without and with the radiation pressure contribution in the simulations. The stronger preferential accretion we observe in the only gas pressure case, results from favourable locking angles between the binary and cavity eccentricity vectors, which significantly enhances the accretion onto the secondary binary component. We note that [131], for a similar case with $e = 0.4$ and $q = 0.7$, reported $\lambda \approx 2$. The inclusion of the radiation pressure again leads to a more balanced accretion rate between the binary components. Our results are somewhat in contrast with RMHD simulations of circular unequal-mass binary presented in [81], where they found that radiation pressure reduces the total accretion rate but does not suppress preferential accretion onto the secondary ($\lambda \sim 1.8$).

In order to better understand the behaviour of the alternation of the accretion rate onto each black hole and the preferential accretion, we analyse the relative precession phase between the disc and the binary, defined as $\varpi = \varpi_d - \varpi_b$. We computed the binary eccentricity vector $\mathbf{e}_\mathrm{b}$ and its phase ϖ_b following equations (5.8) - (5.10). The third and last row of Figure 5.6 show the time evolution of this relative precession for all our binary configurations. Note that the bottom left panel of the second raw has little meaning as the disc is quasi-circular. We compute the disc eccentricity vector phase using Eq. 5.10. In the circular equal mass case (left panel), the phase difference between the binary eccentricity vector and the disc eccentricity vector exhibits a periodic behaviour, repeating over $\sim$ 200 orbital periods. When radiation pressure is included, the disc eccentricity growth is strongly suppressed (see Fig. 5.5) and the disc experiences a periodic behaviour on shorter timescale. The disc eccentricity remains small and therefore, even with an alternating pattern in the relative angle, this does not affect accretion.

In the highly eccentric equal mass scenario (i.e. $e = 0.9$, $q = 1$) shown in the rightmost panel of Figure 5.6, the angular difference exhibits a similar behaviour in the gas-only and radiation-pressure simulations. In both cases, ϖ precesses over approximately 260 orbital periods. In the $e = 0.9$ case, the discontinuity between π and $-\pi$ combined with the use of circular binning, which is not optimal for highly

eccentric configuration, produces some artefacts in the precession phase maps. In the moderate eccentric unequal mass case (i.e., $e = 0.45$ $q = 0.7$) shown in the middle panel of Figure 5.6, the relative precession phase evolves more slowly, with a full cycle spanning ~ 400 orbital periods. The full cycle duration is determined by analysing the relative precession phase over a longer time window, while Fig. 5.6 shows results only in a narrow time window ($t = 1400 - 1600\, P_{\rm B}$) consistent with the time window used in other figures. This results in a temporary locking phase, associated to a strong preferential accretion onto the secondary component. In this simulation we indeed find $\lambda \sim 2$. The inclusion of radiation pressure does not lead to a significant change in the difference between the relative precession phase between the disc and the binary in this case.

In order to further investigate the dynamics of the streams that provide material to the binary component during the alternation of the accretion rate onto each black hole and the preferential accretion phases, which are essentially determined by the angle between the disc and binary eccentricity vectors, we show the disc surface density maps for the two eccentric binary simulations in Figure 5.7. From top to bottom, the panels correspond to angles of $\varpi \sim -\pi, -\pi/2, 0$, except for the $e = 0.45$ radiation pressure case, where we reported $0, \pi/4, \pi/2$. These configurations respectively represent accretion preferentially onto the primary black hole, symmetric accretion onto both components, and accretion predominantly onto the secondary.

In the eccentric equal mass case $e = 0.9, q = 1$, regardless of the presence or not of radiation pressure, when the disc and the binary eccentricity vectors are antiparallel, in agreement with Figure 5.6, the accretion is preferentially onto the black hole located near the cavity edge. When the vectors are perpendicular, the two binary components accrete the same amount of gas. Finally, when the disc and the binary eccentricity vectors are parallel, accretion is favoured onto the black hole further away the cavity edge.

In the middle eccentric case $e = 0.45, q = 0.7$, the behaviour is more complex. In the gas pressure only simulation, we find a similar result to the equal mass case: when $\varpi_{\rm d}$ and $\varpi_{\rm b}$ are antiparallel, accretion is preferentially onto the primary black hole, when they are aligned, it favours the secondary. However, the configuration at $\pi/2$ results in a preferential inflow onto the secondary, which is located closer to the cavity edge. When the radiation pressure is included, the trend is reversed: accretion occurs

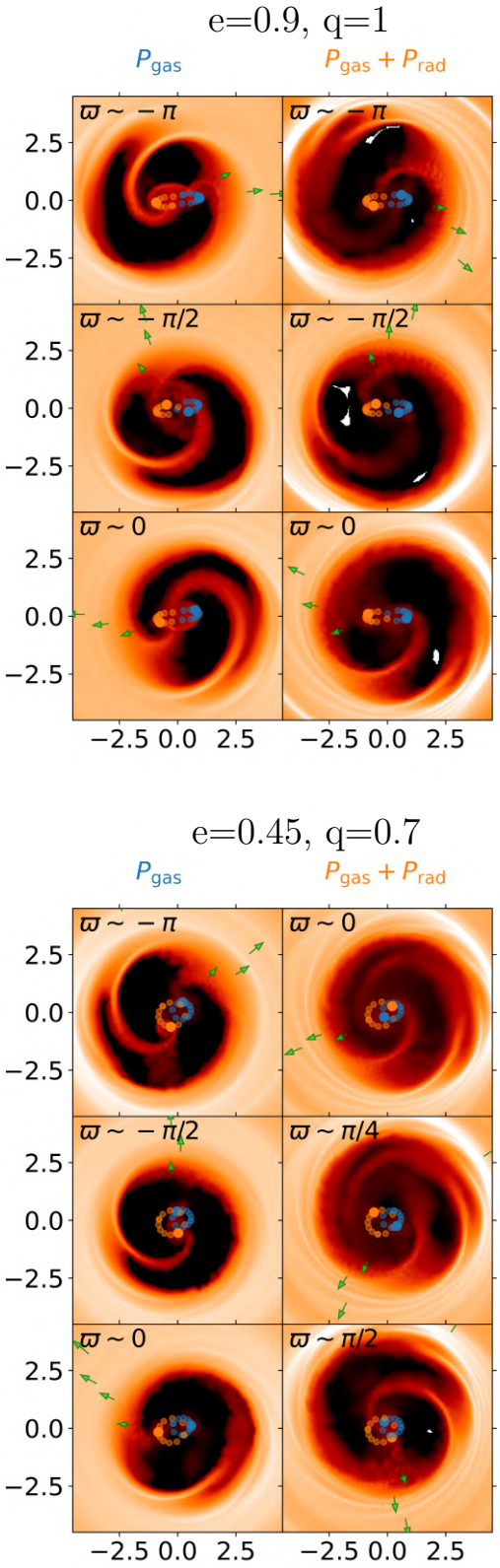

FIGURE 5.7: Surface density maps in the $x - y$ plane of the circumbinary disc around the equal mass eccentric binary $e = 0.9$ and $q = 1$ (left panel), and the unequal mass eccentric binary $e = 0.45$ and $q = 0.7$ (right panel) shown at different relative precession angles. The left and right columns refer to the simulations without and with the radiation pressure, respectively. The solid blue and orange circles represent the primary and the secondary black hole, respectively, while the semi-transparent circles marks each orbit. The green arrows indicate the disc eccentricity vector phase at increasing radii.

preferentially onto the primary when the vectors $\varpi_{\rm d}$ and $\varpi_{\rm b}$ are aligned. As in the only-gas simulation, for $\varpi \sim \pi/2$, the black hole closer to the cavity accretes more gas from the circumbinary disc.

5.4 Summary of the main results

In this Chapter, we find that radiation pressure suppresses the growth of cavity eccentricity and its precession in circular equal-mass binaries, while it has negligible impact in eccentric systems. In the circular equal mass case the effect of radiation pressure is to effectively suppress disc eccentricity growth and therefore prohibit the formation of the "lump", i.e. over-density at the cavity inner edge. This result is in agreement with recent RMHD simulation of circular equal-mass binaries presented in [80], where they found that radiation contribution leads to a less eccentric cavity and a weaker over-density at the inner edge of the disc due to reduced impact of streams and overall disc cooling. Conversely, we find that if the binary is eccentric, the effect of radiation pressure is to lead to a more pronounced lump (see Fig. 5.1). This is consistent with the disc aspect ratio being significantly lower in the simulations with radiation pressure, which, consistently with other studies [141], contributes to enhancing the over-density contrast. In these cases the high binary eccentricity can overcome the effect of radiation pressure suppressing the cavity eccentricity growth while in the circular binary case radiation pressure maintains the circularity of the cavity.

Radiation pressure plays a crucial role in regulating both the vertical structure and thermal evolution of the circumbinary disc. In all simulations, the disc initially cools over the first ~ 400 orbits, reducing its aspect ratio from $H/R = 0.1$ to $H/R \sim 0.01$, as it attempts to reach a self-regulated state with Toomre parameter $Q \sim 1$. When radiation pressure is included, the disc aspect ratio remains at value ~ 0.01 except for the innermost regions, where $H/R \sim 0.05$ due to shocks driven by gas streams that are flung back from the binary and impact the cavity edge. Since the disc is initially completely radiation pressure dominated, the cooling dominates the heating and the disc collapses in the vertical direction, consistent with previous more sophisticated numerical simulations in the literature [138, 139]. The presence of radiation pressure leads to effective temperatures up to a factor of 3 lower than in simulations with only gas pressure. Similarly, in RMHD simulations of circular equal mass

[80] and unqual-mass [81] systems are found a thinner, denser disc structure where radiation contribution leads to weaker streams and colder, thinner disc configurations. Accretion rate onto the binary are lower when radiation pressure is included ($\dot{M} \sim 0.01 - 0.1\,\mathrm{M}_{\odot}/\mathrm{yr}$), consistent with the colder, thinner disc structure [80, 81, 127, 132].

Since we evolve the binary orbit with time, we can track the evolution of the binary orbital elements and assess the dynamical impact of radiation pressure. We find that radiation pressure does not significantly affect the conservation of total angular momentum. The gravitational torque exerted by the disc is always negative, consistent with the fact that our circumbinary discs self-regulate towards aspect ratio lower than 0.1, i.e. the value considered to be the threshold for binary outspiral [121]. The torque due to accretion of particles onto the binary components is always positive and slightly higher in the only-gas-pressure simulation very eccentric $e = 0.9$ case. However, its magnitude is never sufficiently large to counteract the negative gravitational torque and we therefore find our binaries to always decrease their semi-major axis.

The binary eccentricity remains mostly constant, with only minor variations ($e \sim 0.003$ in the circular case and $e \sim 0.46$ in the $e = 0.45$ and $q = 0.7$ case). We therefore do not find convergence towards a unique value, regardless of the presence of radiation pressure in the simulations. While it is possible that the systems have not yet reached an equilibrium eccentricity due to the limited duration of the runs, we note that our results are consistent with those of [32], who similarly find no evolution of the binary eccentricity in the circular equal mass case and an eccentricity growth in the $e = 0.4, 0.5$ and $q = 0.7$ cases over a longer timescale.

We investigate the interplay between the disc morphology and the alternation of accretion onto each black hole. In the unequal mass binary case we explored, the radiation pressure contribution reduces the preferential accretion onto the secondary, resulting in a more balanced mass growth between the binary components. In particular, in the gas-pressure-only eccentric $e = 0.45$ simulation, we find the ratio between secondary and primary black hole to be $\lambda = \dot{M}_2/\dot{M}_1 \sim 2.3$, in agreement with [131]. However, when radiation pressure is included, the accretion is more balanced and $\lambda = 1.18$ and mass ratio growth is effectively suppressed, somewhat in contrast with RMHD simulations of circular unequal-mass binary presented in [81], where they found that

radiation pressure does not suppress preferential accretion onto the secondary. In order to better understand the behaviour of the alternation of the accretion rate onto each black hole and the preferential accretion, we analyse the relative precession phase between the disc and the binary defined as $\varpi = \varpi_{\rm d} - \varpi_{\rm b}$. In equal mass binary cases, we find that ϖ cycles over ~ 200 and ~ 260 orbital periods for eccentricities $e = 0$ and $e = 0.9$, respectively, with shorter cycles in cases with the radiation pressure. For the eccentric unequal mass binary ($e = 0.45$ and $q = 0.7$), ϖ evolves more slowly, allowing temporary locking phases between the disc and the binary. This phases correspond to episodes of enhanced accretion onto one binary component over time. In the radiation pressure simulations, accretion occurs onto the secondary black hole when $\varpi \sim 0$ (i.e., disc and binary eccentricity vectors are aligned). For intermediate angles such as $\pi/2$, we find that preferential accretion can still occur in the unequal mass case, where the black hole closer to the cavity tends to accrete more.

Finally, we note that, since radiation pressure in hydrodynamics simulations of MBHBs regulates the thermal structure of the circumbinary disc, it may also impact the electromagnetic emission of MBHBs, possibly affecting the periodic signatures in emitted light used to identify these objects in observations. This is the subject of a follow up work F.Cocchiararo et al. (in prep).

Chapter 6

Suppressed "lump" EM signature in radiation pressure dominated accreting massive black hole binaries

Based on:

F.Cocchiararo, A.Franchini, A.Lupi, A. Sesana,

"Suppressed "lump" EM signature in radiation pressure dominated accreting massive black hole binaries", 2025, submitted to A&A, DOI, ADS link

---

This chapter is the second part of a larger project focusing on the role of radiation pressure in the evolution and emission of massive black hole binaries at milli-parsec separation. We here investigate its impact on the EM emission and EM characterisation of these systems. As discussed in Sec. 3.2.2, besides the natural variability arising from the binary orbital period, one of the most promising EM signatures of MBHBs is the so-called 'lump', that can modulate the accretion rate onto the binary, producing periodic variability in the emitted light. Despite the diversity in numerical methods and physical models adopted, it is well established that the lump originates when the particles of gas flung back to the cavity edge, shock and deposit material at the inner edge of the circumbinary disc. Moreover, the lump is stronger in circular equal-mass binaries, with amplitude decreasing for lower mass ratios [74]. However, at larger binary separations (e.g., $10^{-4}\,\mathrm{pc} \sim 10^{4}\mathrm{R_g}$), our results presented in Chapter

4 shown that the lump can also form in eccentric equal-mass binaries, thus making it a potential smoking-gun signature of equal-mass systems. Indeed, it is important to verify whether this dynamical feature survives the implementation of additional physics that is expected to play an important role in the problem. One additional piece of physics is radiation pressure, whose impact at large binary separations has remained largely unexplored. The first part of this project, discussed in Chapter 5, we addressed this gap by investigating its impact on the evolution of accreting MBHBs at milli-parsec scales using 3D numerical simulations. We found that radiation pressure alters the vertical and thermal structure of the disc, producing a geometrically thinner, and therefore colder, configuration. This leads to a reduced accretion rate onto the binary and suppresses cavity eccentricity growth and precession in circular equal mass binaries, with potential implications for the EM emission and periodic signatures used to identify these systems. Consistently, 3D radiation magneto-hydrodynamics (RMHD) simulations of MBHBs at smaller radii reported similar effects, further supporting the key role of radiation pressure in shaping circumbinary disc dynamics [80].

A detailed characterisation of EM signatures at intermediate separations of $10^{-4} - 10^{-2}$ pc, corresponding to orbital periods of days to years, in particular under the influence of radiation pressure, is currently missing and it is essential both to constrain the origin of the GWB evidence in PTA experiments and to identify MBHB candidates in time-domain surveys, such as the future upcoming Vera Rubin Observatory [Rubin Observatory; 156]. These candidates may represent the progenitors of merging binaries that will be detected by LISA [98, 167, 168].

Motivated by these considerations, in this work we have computed for the first time the SEDs and the multi-wavelength LCs from 3D numerical simulations with hyper-Lagrangian refinement of milli-parsec scale binaries including the radiation pressure contribution in the disc. We use the same set of numerical simulations presented in Chapter 5. The simulations include a radiative cooling prescription in the form of black body cooling. They also include gas self-gravity and the Shakura-Sunyaev prescription for viscosity. We computed the electromagnetic emission for three values of the binary eccentricity $e = 0, 0.45, 0.9$ and mass ratio $q = 1, 0.7$. The simulated binaries were placed at different redshift ($z = 0.1, 0.4, 0.7, 1.0, 1.5$), and the resulting flux was evaluated across different frequency bands, with particular emphasis on the

optical bands that will be accessible to the upcoming Rubin Observatory. Since we explore the same set of parameters used in the set of simulations presented in Chapter 4, in which radiation pressure was not included, we can directly estimate its effect on the electromagnetic emission.

In the following, we show and discuss the main results we obtain in the EM emission properties. Finally, we draw our conclusions and discuss possible observational implications.

6.1 Spectral energy distributions

We compute the EM emission from our numerical simulations using Plank's law (Eq. 3.4). In determining the disc temperature, we account for both the gas and radiation pressure contribution, as explained in Section 3.3.4.

Figure 6.1 shows the SEDs obtained for each region for equal mass binaries $e = 0$ and $q = 1$ (top panel), unequal mildly eccentric binaries $e = 0.45$ and $q = 0.7$ (middle panel) and equal highly eccentric binaries $e = 0.9$ and $q = 1$ (bottom panel), from simulations without and with radiation pressure, on the left and right column respectively. The spectra are shown at a the same time-step. The spectra obtained by analysing the emission from the mini-discs and the streams region (blue, orange, and green lines) exhibit a clear shift of the emission peak toward higher frequencies when radiation pressure is included, transitioning from peak emission in the optical to the UV band. In the equal-mass circular case ($e = 0$, $q = 1$), the minidiscs show an increase in peak luminosity of approximately an order of magnitude, with peak frequency shifting by $\log(\nu/\mathrm{Hz}) \sim 0.3$. The stream region, instead, shows a frequency shift $\log(\nu/\mathrm{Hz}) \sim 0.2$ but does not show a significant change in luminosity. For the eccentric cases the effect of radiation pressure is even more pronounced. In the moderately eccentric case ($e = 0.45$, $q = 0.7$), both primary and secondary minidiscs display a significant increase in peak luminosity by ~ 3 orders of magnitude, with a frequency shift of the emission peak of $\log(\nu/\mathrm{Hz}) \sim 0.6$ and $\log(\nu/\mathrm{Hz}) \sim 0.4$, respectively. The stream region also shifts toward UV frequencies ($\Delta \log(\nu/\mathrm{Hz}) \sim 0.3$) and increases by a factor of ~ 1 in luminosity. In the highly eccentric case ($e = 0.9$, $q = 1$), the mini-discs still show an enhancement in peak luminosity by ~ 2 orders of magnitude, with a shift in frequency of $\log(\nu/\mathrm{Hz}) \sim 0.4$ and $\log(\nu/\mathrm{Hz}) \sim 0.6$ for the mini-disc around the primary and secondary, respectively. This behaviour is in

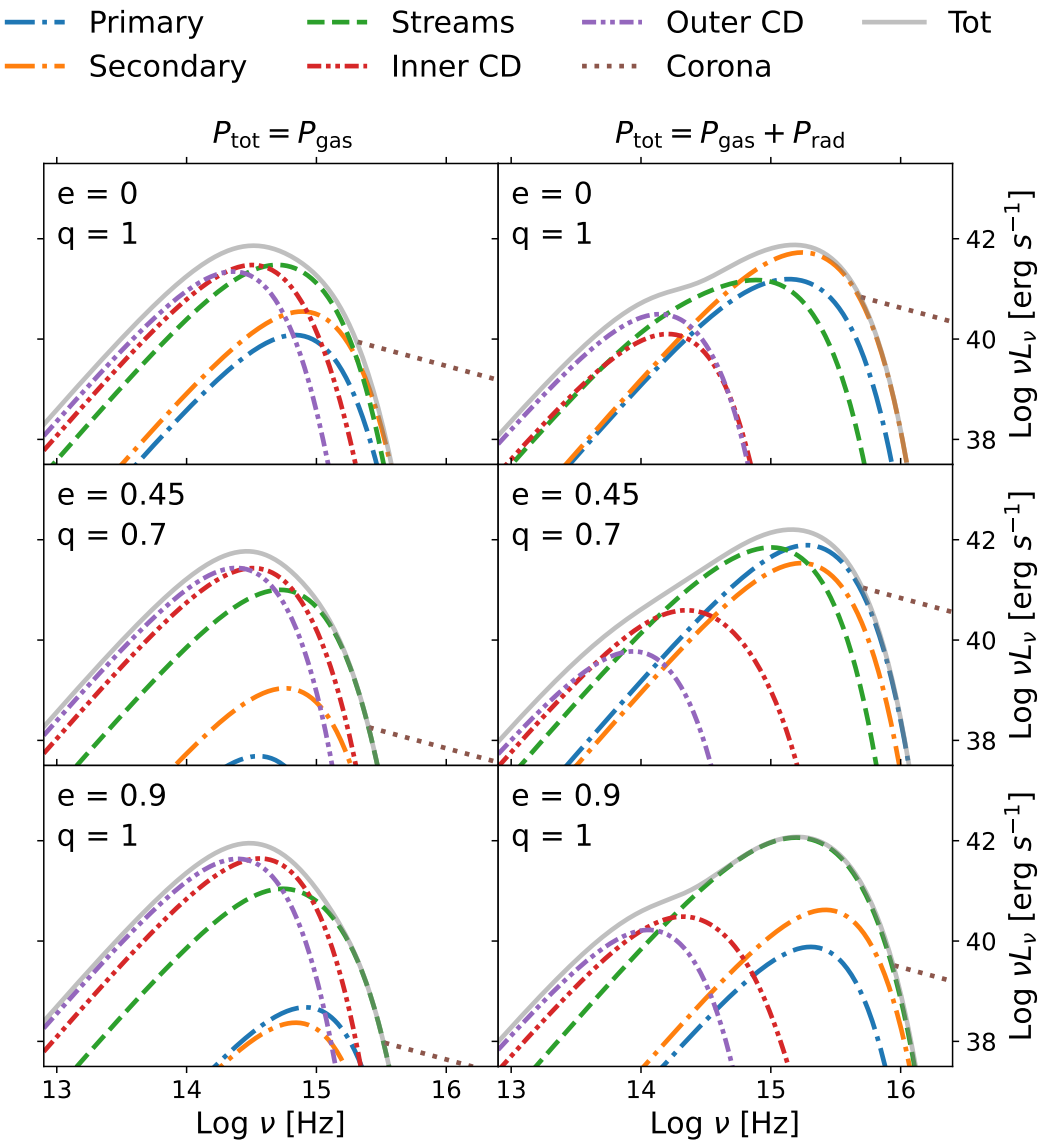

FIGURE 6.1: Spectral energy distributions (SEDs) obtained by including the contribution of the radiation pressure either a posteriori (left column) or during the binary evolution (right panel) at the same accretion rate for the $e = 0$ $q = 1$ binaries (top panel), $e = 0.45$ $q = 0.7$ binaries (centre panel), and $e = 0.9$ $q = 1$ binaries (bottom panel). The contribution from the different regions of the disc (e.g. mini-discs, stream, inner and outer part of the circumbinary disc and the corona) are highlighted in different colours and have been computed at the time when the accretion rate of both binaries is equal.

agreement with RMHD simulations of circumbinary discs presented in [80] and [81], which they found thermal emission peaking in the optical/UV band with luminosities of order $\sim 1\%\, L_{\rm Edd}$ for systems of mass $\sim 10^7\, M_\odot$.

We find that the inner and outer regions of the circumbinary disc (red and purple lines) follow an opposite trend. In all cases, the inclusion of radiation pressure causes their peak emission to shift towards lower frequencies by approximately $\log(\nu/{\rm Hz}) \sim 0.2 - 0.3$, while the luminosity decreases by ~ 1 order of magnitude. This behaviour is consistent with the fact that radiation pressure significantly alters the vertical and thermal structure of the circumbinary disc, resulting in a geometrically thinner, therefore colder configuration [80, 139, 169, 170]. In the results discussed in Chapter 5, we found that the disc aspect ratio settled around $H/R \sim 0.02$ and the effective temperature dropped to $T_{\rm eff} \sim 2 - 3 \times 10^3\,{\rm K}$, a factor ~ 3 lower than in gas-only simulations.

Figure 6.2 shows the radial profiles of surface density Σ, disc aspect ratio H/R, midplane temperature T, optical depth τ and effective temperature $T_{\rm eff}$ for the two mini-discs around each binary component for the circular equal mass case, at time $t = 1133\, P_{\rm B}$, for the simulation with and without radiation pressure (straight and dotted lines respectively). The inclusion of radiation pressure in the simulation causes the surface density to decrease by 1 order of magnitude compared to the gas-only case, while H/R increases by a factor ~ 3. The mini-discs experience a vertical expansion because of their lower density. Since the radiation pressure provides most of the hydrostatic support, a decrease in density causes an increase in aspect ratio, if the temperature is roughly the same. The midplane temperature remains indeed comparable in both cases ($T \sim 2 - 4 \times 10^4\,{\rm K}$). The decrease in surface density leads to a lower optical depth (τ decreases from $\sim 10^2$ to ~ 100), which translates into a higher effective temperature: $T_{\rm eff}$ rises from $\sim 6 \times 10^3 - 10^4{\rm K}$ in the gas-only simulation to $\sim 2 \times 10^4 - 3 \times 10^4{\rm K}$ when radiation pressure is included. A lower surface density would also imply a more efficient black-body cooling. However the mini-discs continuously experience shocks from the streams and during their mutual interactions, resulting in heating overcoming radiative cooling.

The opposite trends observed in the evolution of the mini-discs is driven by the global structure and evolution of the circumbinary disc. In the radiation-pressure cases, the circumbinary disc remains geometrically thin and does not experience the

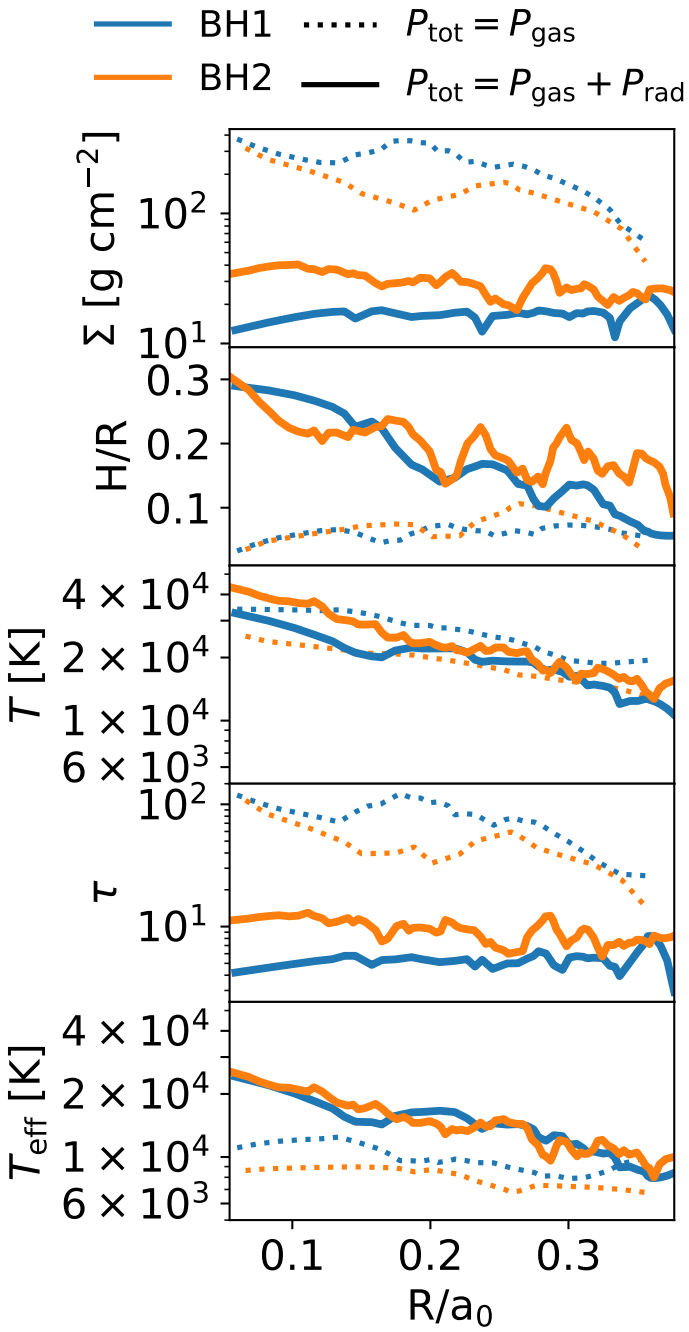

FIGURE 6.2: Profiles of surface density (first row), disc aspect ratio H/R (second row), midplane temperature (third row), optical depth τ and the effective temperature (last row) for the two mini-discs around each black hole in the circular equal mass binary, at time $t = 1133\, P_{\rm B}$, the same shown in Fig. 6.1. Blue and orange lines correspond to the two mini-discs while the solid and dashed lines refers to the simulation without and with the implementation of the radiation pressure, respectively. We calculate the profiles of these quantities within the Roche Lobe of each black hole. We computed the midplane temperature and the effective temperature assuming that both the gas and the radiation pressure contribute to the hydrostatic equilibrium of the disc.

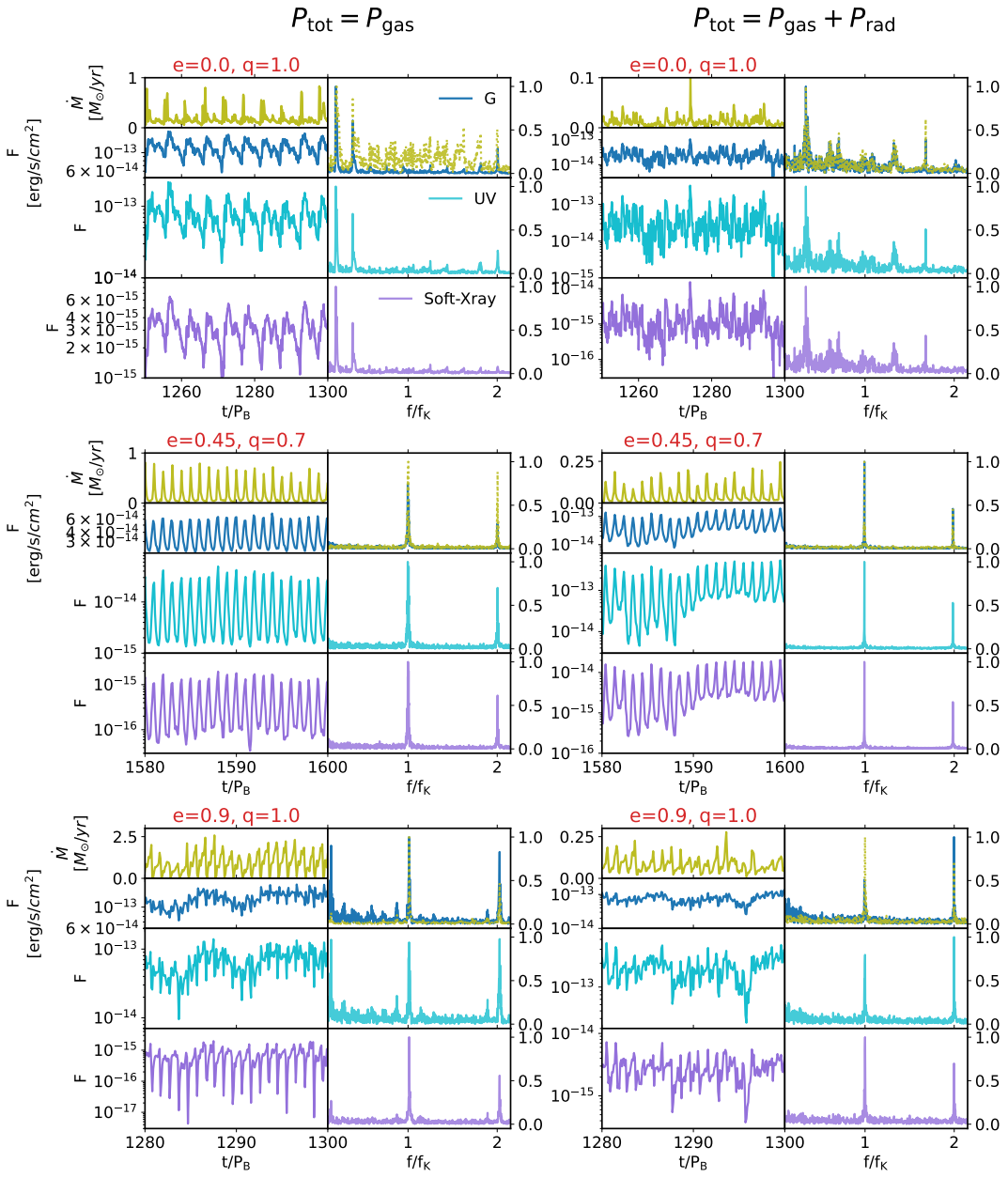

FIGURE 6.3: Light curves and the corresponding Fast Fourier Transform (FFT) obtained by including the contribution of the radiation pressure either a posteriori (left column) or during the binary evolution (right panel) for the $e = 0$ $q = 1$ binaries (top panel), $e = 0.45$ $q = 0.7$ binaries (centre panel), and $e = 0.9$ $q = 1$ binaries (bottom panel). In each panel, the first row shows the accretion rate (green line) and the optical G flux (blue line), while the second and last row show the flux and FFT in the UV (light blue line) and soft-X (purple line) band, respectively. The FFT is computed over 300 orbits in the window $t = 1000 - 1300\,P_B$ for the circular case and over 400 orbits in the window $t = 1200 - 1600\,P_B$ and $t = 900 - 1200\,P_B$ for the mildly and highly eccentric cases, respectively. The FFT is normalised to unity and shown as a function of f/f_k with f_k the Keplerian frequency of the binary. The optical flux is computed considering an extra Gaussian noise component, as described in Sec. 3.3.4.

vertical expansion as in the gas-only pressure cases. As a consequence, a smaller amount of material flow into the cavity, resulting in mini-discs with lower surface density. The reduced surface density leads to a lower optical depth, which boost the effective temperature of the mini-discs. Moreover, the lower density enhances the vertical pressure support through the $(1/\rho)(\partial P/\partial z)$ term in the vertical momentum equation, leading to an increase in the aspect ratio of the mini discs. As a result, in the radiation-pressure cases the mini-discs are thicker and hotter even if the circumbinary disc is thinner and colder than the gas-only cases.

6.2 Light curves

We compute the integrated luminosity from each region of the disc to obtain the LCs, which trace the time evolution of the flux. For simplicity, we present the LCs for a source at redshift $z = 0.1$ and then we explore how redshift affects the detectability of a source. The bolometric flux is calculated in three different regions of the EM spectrum: in the optical, using the Rubin Observatory filters frequency bands (see Table 1 in [38] for frequency band value specifications), in the near-UV ($1.0-1.5\times10^{15}$ Hz or $4.13-6.20$ eV), and in the soft X-ray ($7.25-48.3\times10^{16}$ Hz or $0.3-2$ keV). We show the results in the optical G filter only because, as shown in our previous work [38], the amplitude of the peak in the FFT of the light curve varies across the different optical bands, reaching its maximum in the optical g band, making it the most suited for identifying periodic modulations from MBHBs in Rubin Observatory. This choice is further supported by the results presented in [171], which indicate that the Rubin Observatory G band is expected to yield the highest number of detectable MBHB candidates. The results for simulations without and with the implementation of radiation pressure contribution, are shown in left and right column of Figure 6.3, respectively.

Consistent with gas-pressure-only simulations, even with the radiation pressure the emission is brighter in the optical and UV bands, while it is dimmer in the soft X-ray band. Another consistent trend is that variability tends to increase with frequency: while Rubin Observatory g band flux changes by a factor ≤ 1 order of magnitude, the UV and X-ray fluxes can experience oscillations up to 2 orders of magnitude. The emission in the optical bands comes mostly from the circumbinary disc, which is colder and less variable than the emission that comes from within the cavity. The

high variability found in the UV is due to the high variability of the streams and the mini-discs, which also impacts the emission of the non-thermal hot corona that emits in the soft-X band. The large amplitude variation in the UV flux that we find suggests that these systems might be identifiable by future wide-field UV facilities, such as ULTRASAT [scheduled for launch in 2027, 158] and UVEX [scheduled for launch in 2030, 159].

The gas-pressure-only equal-mass simulations show a clear flux periodicity structure. In the FFT of the fluxes across all bands, we can clearly see the lump periodicity at $0.2\,f_{\rm K}$ and $0.15\,f_{\rm K}$ for the circular $e = 0$ and highly eccentric $e = 0.9$ case, where $f_{\rm K}$ is the Keplerian frequency of the binary. Moreover, in both cases the FFT peaks associated with the binary motion are present: in the circular case one peak at $f = 2\,f_{\rm K}$ and in the eccentric case peaks at $f = 1, 2\,f_{\rm K}$.

When radiation pressure is included, the picture becomes more complex. In the circular equal-mass case, both the flux and the accretion rate FFTs show a more intricate pattern, with a prominent peak at $f = 0.36\,f_{\rm K}$ with its second harmonic at $f = 0.72\,f_{\rm K}$. Additionally, since the motion of gas flows is complex and the fluxes are not purely sinusoidal, the interaction between the gas in the mini-discs, streams, and the cavity edge produces additional peaks in the FFT corresponding to linear combination of the two main fundamental modes: the peak at $f = 1.32 f_{\rm K}$ corresponds approximately to the sum of $f = 0.36\,f_{\rm K}$ and $f = 1.0\,f_{\rm K}$, while the peak at $f = 1.68\,f_{\rm K}$ corresponds to a combination of $f = 1\,f_{\rm K}$ and $f = 2 \times 0.36 f_{\rm K}$. In the highly eccentric case $e = 0.9$, the FFT displays only the periodicities at $f = f_{\rm K}$ and $f = 2 f_{\rm K}$ which are driven by the binary orbital motion. Although some power is present near the expected lump frequency, it does not emerge as a distinct peak, unlike in the gas-pressure-only simulations. Similarly, in the mildly eccentric unequal mass case ($e = 0.45$ and $q = 0.7$), the flux FFT shows two peaks at $f = f_{\rm K}$ and $f = 2 f_{\rm K}$, both with and without the radiation pressure contribution.

In order to better understand the origin of the periodicities in the radiation pressure simulations and the differences with the ones in the gas-pressure-only simulations, we refer to Figure 6.4. The figure displays the surface density and effective temperature maps for circular equal-mass ($e = 0$, $q = 1$) binaries (upper sub-figure) and highly eccentric equal-mass ($e = 0.9$, $q = 1$) binaries (bottom sub-figure) at the same time as reported in Figure 6.1.The first and second rows show the surface density map and

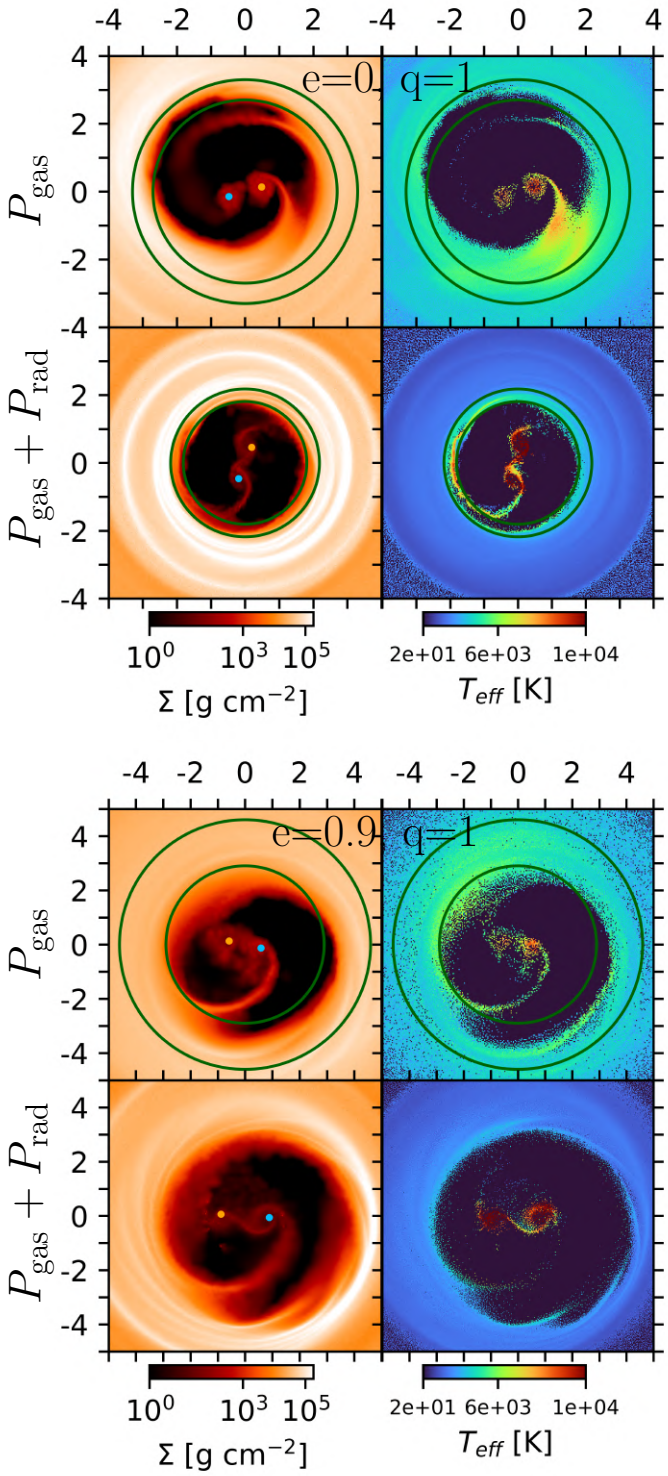

FIGURE 6.4: Surface density and effective temperature maps for circular equal-mass binaries with $e = 0$ (upper figure) and $e = 0.9$ ($e = 0.9$, $q = 1$) binaries (bottom figure). For each case, the first and second row show the result of simulations without and with radiation pressure, respectively. The green circle marks the region from which the main emission modulation in the FFT originates: in gas-pressure-only cases, this corresponds to the lump ($R \sim 2.5 - 3\,a$ for $e = 0$, and $R \sim 2.9 - 4.5\,a$ for $e = 0.9$), while with radiation pressure the main emission at low frequencies in the circular binary arises from the cavity edge ($R \sim 1.81 - 2.18\,a$).

the effective temperature map for simulation without and with the implementation of the radiation pressure contribution, respectively.

Since the frequency scales with radius as $f \propto R^{-3/2}$, we mark with green circles the regions from which the emission associated to the main peak in the FFT analysis is coming from. In gas-pressure-only simulations, these regions extend over $R \sim 2.5-3\,a$ for the circular binary, and $R \sim 2.9-4.5\,a$ for the eccentric case. These correspond to the location of the "lump", with frequency emission peaks at $f = 0.2\,f_{\rm K}$ and $f = 0.15\,f_{\rm K}$, respectively.

When radiation pressure is included, the FFT emission in the circular case shows a prominent peak at $f = 0.36\,f_{\rm K}$, which originates from a region at $R \sim 1.81-2.18\,a$, i.e., at the edge of the cavity. During the binary accretion, some of the gas that leaks into the cavity is flung back towards the inner edge of the circumbinary disc, where it produces shocks that heat the cavity edge. This gives rise to a circular region with an effective temperature about one order of magnitude higher than that of the circumbinary disc. In the highly eccentric case ($e = 0.9$), although a slight temperature enhancement is still present at the cavity edge, we do not find any low-frequency modulation and we therefore omit the green circles in the panels of Fig. 6.4. It is important to note that, in the circular case, even if the lump modulation does not form, there is still a flux modulation associated with the gas motion along the inner edge of the cavity. However, in the highly eccentric case, the lump is visible in the surface density map, but the temperature remains almost uniform. As a result, no flux modulation is linked to the motion of the cavity edge and there are only the modulations at $f = f_{\rm K}$ and $f = 2f_{\rm K}$. These results suggest that the radiation pressure contribution largely suppresses the presence of the electromagnetic signature associated with the lump-driven flux modulation. This result is in contrast with previous RMHD simulations of circular equal-mass binaries [80, 81], where residual periodicity at frequencies compatible with the expected lump modulation is still observed despite a weakened inner-edge over-density.

Finally, we investigate the impact of placing the binary system at different redshifts in order to assess the detection limits taking into account a 5σ sensitivity detection threshold in the optical band. Figure 6.5 shows the results. As expected, more distant binaries appear to be fainter and harder to detect. In gas-pressure-only simulations, we find different behaviour based on different cases. In the circular case, all the

periodicities are clearly visible up to redshift $z = 0.6$, while at higher redshift only the signal associated with the lump at $f = 0.2\, f_{\rm K}$ remains detectable up to redshift $z = 1.2$. In the mildly eccentric case $e = 0.45$, all the peaks are distinguishable up to redshift $z = 0.4$, whereas beyond this redshift only the modulation associated to the orbital period at frequency $f = f_{\rm K}$ can still be identified up to redshift $z = 0.6$. In the highly eccentric case $e = 0.9$, the three periodicities can be all detected up to $z = 0.7$, but at higher redshift the flux becomes very noisy and the peaks are no longer distinguishable. Instead, the inclusion of radiation pressure improves the detectability, in almost all the cases, in particular in the eccentric ones. In the circular binary case $e = 0$, the periodicities remain visible up to $z \sim 0.8$, with the periodicity at $f = 0.36\, f_{\rm K}$ visible up to $z = 1.0$, while for highly eccentric system $e = 0.9$ they are still detectable up to $z \sim 1.2$. In the mildly eccentric case $e = 0.45$, the periodicity associated with the binary orbital period can even be detected up to redshift $z = 2$. The enhanced emission from the mini-discs and streams due to radiation pressure, once redshifted, results in a higher flux in the optical bands, improving detectability of MBHBs signatures even at higher redshifts.

6.3 Periodic signal identification in Rubin Observatory survey

Periodic features in the light curves of MBHBs represent one of the most promising electromagnetic signatures to distinguish them among candidates. Testing whether such signals can be recovered with the cadence and sensitivity of the future Rubin Observatory is therefore crucial to this aim. So far, we have computed the FFT across a large set of binary orbits, successfully disentangling the different periodicities arising from binaries with different mass rations and eccentricities. However, Rubin Observatory will likely have access to only a limited number of binary orbits during its 10-years surveys, depending on the binary orbital period. Thus, it could be non-trivial to detect periodicities.

In order to evaluate the impact of the radiation pressure on the periodicity detectability by the Rubin Observatory, we repeated the same analysis carried out in [38]: we perform FFT of the accretion rate and flux in the optical G band over 5,10 and 50 orbits windows, sliding them across a total of 300 and 400 orbits in circular and eccentric binaries, respectively. For each configuration, we average the FFT and compute

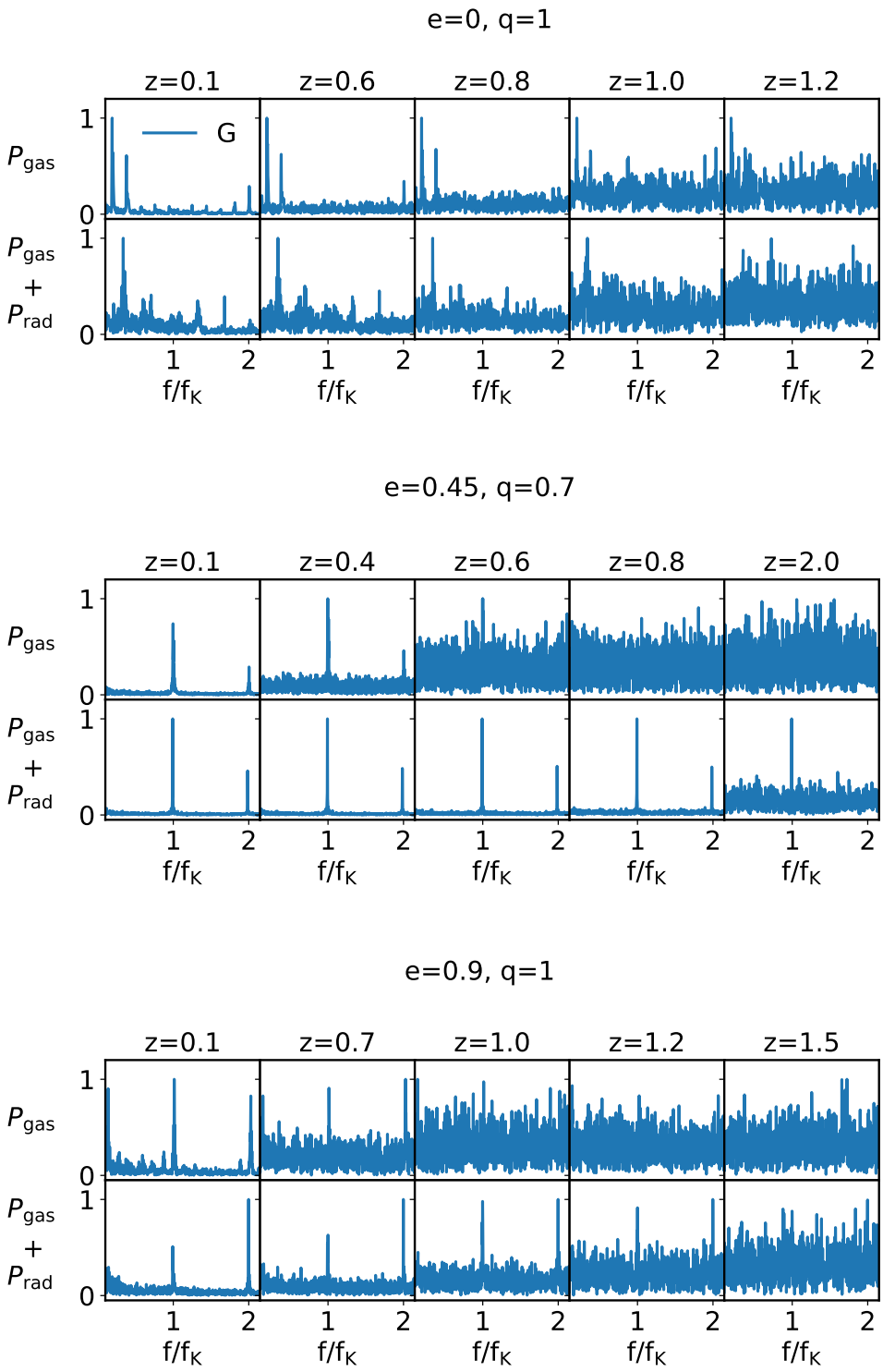

FIGURE 6.5: Fast Fourier Transform of the optical g band flux. From the top to the last panel: circular, mildly eccentric $e = 0.45$ and highly eccentric $e = 0.9$ binaries. The first and second row of each case shows the FFT computed without and with the implementation of the radiation pressure, respectively. The FFT is computed over 300 orbital periods in the eccentric case and 400 orbital periods in the eccentric ones, placing the binaries at different redshifts.

their mean and standard deviation at redshifts $z = 0.1, 0.4, 0.7, 1.0, 1.5, 2$. The results are shown in Figure 6.6 where, for simplicity, we only show the cases with redshift $z = 0.1, 0.4, 0.7, 1.0$. Comparing our results with those in Figure 6 from [38], we find the same main trend observed in gas-pressure-only simulations: periodicities are easier to detect in unequal-mass systems, while equal-mass binaries exhibit weaker signals that improve with longer time-windows. As in the gas-pressure-only case, at higher redshifts, the variance, i.e. the statistical error on the mean flux/accretion rate, grows due to the Rubin Observatory sensitivity limit, particularly in the equal mass and highly eccentric binaries.

In the equal-mass case, only the main peak at $f \sim 0.36\, f_{\rm k}$ can be distinguished at low redshift ($z < 0.4$) when considering 5-10 orbits, while increasing the number of orbits up to 50 makes the identification of periodicities possible but only up to $z \sim 0.7$. In the highly eccentric equal-mass case ($e = 0.9$, $q = 1$) the peaks corresponding to the two modulations at $f = f_{\rm K}$ and $f = 2f_{\rm K}$ are more pronounced and can be clearly identified even taking into account a few orbits, in contrast to the case of gas-pressure-only simulation, where the signals are distinguishable only taking into account at least 10 orbits or 50 orbits at redshift $z < 0.4$ and $z < 0.7$, respectively.

In the unequal-mass case, the periodicities are easily distinguishable even at $z = 1.5$, even taking into account 5 orbital periods, in contrast to what was found in the gas-pressure-only simulations. We find that periodic signatures remain visible up to redshift $z \gtrsim 0.6 - 1.0$, higher than in the gas-pressure-only case. This improvement is given by the enhanced emission from the mini-discs and streams, which once redshifted boosts the observed flux in the optical band. Neglecting radiation pressure in the model may artificially lower the predicted detectability rate.

We note that we have assumed 5 and 10 orbits windows for the FFT because our binaries have a ~ 1 year orbital period and Rubin Observatory would last 10 years. This choice reflects a compromise: several cycles are needed to detect reliable periodicity, but binaries with longer periods are more numerous and complete fewer cycles within the survey baseline, making them harder to identify. Conversely, binaries with separations sufficiently small to do many cycles in the Rubin Observatory time-span can instead be more easily detected. Finally, a comprehensive statistical evaluation of the Rubin Observatory ability to detect these periodicity will be carried out in a future work F. Cocchiararo et al. (in prep).

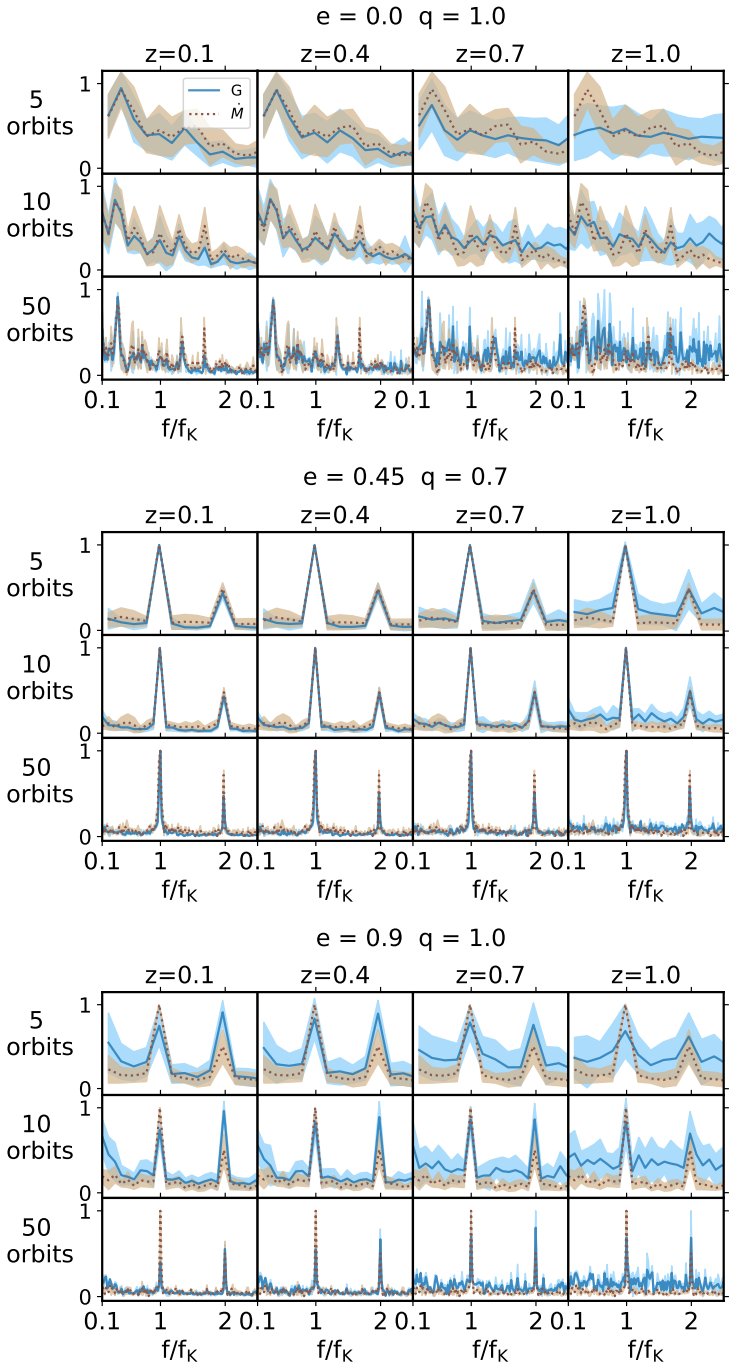

FIGURE 6.6: Fast Fourier transform of LCs from simulations with the implementation of radiation pressure. From the top to the last panel: circular, mildly eccentric $e = 0.45$ and highly eccentric $e = 0.9$ binaries. The first row of each case shows the FFT of the Optical G band flux (blue line) and the FFT of the accretion rate (brown line) computed over 5-orbit windows within a total of 300/400 orbital periods at redshift z = 0.1, 0.4, 0.7, 1.0. The second and the third rows show the FFT computed over 10- and 50-orbit windows, respectively.

6.4 Summary of the main results

In this Chapter, we find that radiation pressure plays a crucial role in shaping both the spectral energy distributions and the temporal variability of MBHBs, affecting the electromagnetic signatures of these systems. Radiation pressure produces opposite effects on the different emitting regions of the system. While the circumbinary disc becomes geometrically thinner, colder and less luminous with the emission peak shifting towards lower frequencies ($\Delta \log(\nu/\mathrm{Hz}) \sim 0.2 - 0.3$), the mini-discs experience vertical expansion and have a higher effective temperature, resulting in a shifted emission toward higher frequencies ($\Delta \log(\nu/\mathrm{Hz}) \sim 0.2 - 0.3$ in circular binaries and $\Delta \log(\nu/\mathrm{Hz}) \sim 0.4 - 0.6$ in eccentric cases) with luminosities increased by $1 - 2$ orders of magnitude with respect to the gas-pressure-only simulations, consistent with [80, 81]. The inclusion of the radiation pressure contribution modifies also the modulations of the flux coming from these systems. We computed the LCs in different frequency bands, mainly focusing on the optical window that will be probed by Rubin Observatory. Consistently with the shift in emission frequency, we find that the flux in the optical and near-UV frequency bands is higher with respect to the gas-pressure only simulation cases. The variability is also affected: while in the optical G band, flux oscillations reach a factor ≤ 1 order of magnitude, in the near-UV and soft-X ray bands they can vary by up to 2 order of magnitude as in gas-only simulations, comparable with what found in [80], [81].

In contrast to gas-pressure-only simulations discussed in Chapter 4, where a clear modulation associated to the lump was found in equal-mass circular and highly eccentric binaries, here the lump-driven modulation is strongly suppressed. In the circular equal-mass case, both the flux and the accretion rate FFTs reveal clear peaks at $f \sim 0.36\, f_{\mathrm{K}}$ and $f \sim 0.72\, f_{\mathrm{K}}$, associated to emission from the heated inner edge of the cavity. Indeed, during the accretion of gas onto the binary, some gas is flung back to the cavity edge, generating shocks that locally heat the gas. Moreover, in the LCs, we can notice other peaks: at $f = f_{\mathrm{K}}$ and $f = 2f_{\mathrm{K}}$ corresponding to a periodicity of the binary orbital period and half of it and $f = 1.32, 1.68\, f_{\mathrm{K}}$ interpreted as linear combinations of the main two fundamental modes. In the eccentric cases, the FFT shows only the periodicities at $f = f_{\mathrm{K}}$ and $f = 2f_{\mathrm{K}}$.

The results discussed so far apply when the FFT is evaluated over long time spans, corresponding to several hundreds of binary orbits. However, Rubin Observatory

will cover only a decade of observations, while most compact MBHBs are expected to have orbital periods of the order of years. To provide a more realistic estimate of the detectability of periodic signals, we therefore computed the FFT of the flux and accretion rate using shorter time windows of 5, 10, and 50 orbits, putting the source at different redshifts, and we compared the results with those obtained from gas-pressure-only simulations. Even with radiation pressure, in the circular equal-mass case identifying periodic signals is non-trivial, in particular with a handful of orbits. As expected, the periodic peaks become clearer and the statistical noise decreases when the number of orbits increases. In the highly eccentric equal-mass case the radiation pressure suppresses the lump modulation, but variability on the binary orbital period is quite pronounced, and the detection of periodicities even with a few orbits is improved with respect to the gas-pressure-only case. Finally, in the unequal-mass case, as also reported in the gas-pressure-only simulations, periodicities are easier to detect even at higher redshift $z \sim 1.5$. Because of the relatively low luminosity of our systems ($L_{\rm bol} \approx 10^{42}\,{\rm erg\,s^{-1}}$), periodic signals would be observable with Rubin Observatory only from systems at redshift $z < 0.7 - 1.0$.

The suppression of the lump modulation in equal-mass systems once radiation pressure is included in hydrodynamical simulations challenges one of the most promising EM tracers suggested by previous works. This results stress the importance of adopting simulations with more realistic physical processes in order to obtain a more comprehensive model of these systems and better characterise their EM signatures. At the same time, is it crucial to developed new statistical approaches to assess the observability of the predicted features. This second point will be the subject of a future publication Cocchiararo et al. (in prep).

Conclusions and outlook

In this thesis, we have investigated the dynamics and electromagnetic signatures of accreting massive black hole binaries at milli-parsec separations, using 3D hyper-Lagrangian hydrodynamical simulations. We used the 3D meshless finite mass version of the code GIZMO [123] enhanced with the particle splitting technique [36] to increase the resolution inside the cavity carved by the binary. In our simulations, we modelled the discs with an adiabatic equation of state, allowing the gas to heat due to shocks, viscous dissipation and PdV work, and to cool via black-body radiation. Additionally, we implemented the radiation pressure in the hydrodynamics evolution of the circumbinary disc and thus we evaluate its impact on both the evolution of the binaries and circumbinary discs as well as on the electromagnetic emission expected from these systems.

We modelled live binaries [37] with a total mass of $10^6\,M_\odot$ and initial separation $a_0 = 4.8 \times 10^{-4}\,\mathrm{pc}$. We have explored eccentricities $e = 0, 0.45, 0.9$ and mass ratios $q = 0.1, 0.7, 1$. We performed a total of 9 simulations, three of which include radiation pressure. We evolved each system for 1300 binary orbits (except for the $e = 0.45$, $q = 0.7$ case, which is evolved for $1600\,P_\mathrm{B}$) to ensure that the circumbinary disc reaches a quasi-steady state. We investigated the evolution of the disc properties (e.g., aspect ratio H/R, surface density Σ and effective temperature T_eff) and binary parameters (e.g., the binary semi-major axis a, eccentricity e and accretion rate $\dot{M}$). We also computed the SEDs and LCs positioning the source at different redshift $z = 0.1 - 2$ to evaluate the detectability of periodic signatures in the future surveys such as the Vera Rubin Observatory Legacy Survey of Space and Time (LSST/Rubin Observatory) [156].

In simulations with gas pressure only, we found that, after an initial phase in which the black-body cooling dominates the gas thermodynamic evolution, the disc thickens again, reaching $H/R \sim 0.08$ in its inner parts and maintaining a lower $H/R \sim 0.04$

(corresponding to a lower temperature) in its outer part, regardless of the initial choice of binary mass ratio and eccentricity. The final equilibrium state is primarily driven by the initial disc mass and radial extension, which are the same in all simulations, indicating that self-regulation [155] drives all discs toward a similar aspect ratio after the transient phase. We find the binary-disc interaction to cause the binary to shrink, regardless of the initial conditions. Since in our model the temperature changes with time, this result further supports previous findings in the literature [35, 67]. We find that circular orbits tend to develop higher eccentricities, in agreement with previous works [e.g. 32, 145], while highly eccentric binaries show negligible eccentricity evolution within the timescales of our simulations. We notice, however, that we followed the evolution of the relaxed disc only for about 400 orbits, corresponding to 400 years. However, it might be that the eccentricity evolution for very eccentric binaries occurs on a longer timescale than the one simulated here. Indeed, here we simulated the binary evolution over $\sim 1300/1600\,\mathrm{yr}$, while in both the cited works the timescale is longer.

The implementation of radiation significantly alters the disc evolution. Circumbinary discs remain geometrically thinner and colder, with $H/R \sim 0.01$ in most of the disc and reaches $H/R \sim 0.05$ only in the innermost regions affected by the shocks produced by the gas streams. Radiation pressure suppresses the growth of cavity eccentricity in circular equal-mass cases, preventing the formation of the characteristic "lump" at the cavity edge. Conversely, we find that in eccentric binaries, radiation pressure enhances the lump. This is consistent with the disc aspect ratio being significantly lower in the simulations with radiation pressure, which, consistently with other studies [141], contributes to enhancing the over-density contrast. In these cases the high binary eccentricity can overcome the effect of radiation pressure suppressing the cavity eccentricity growth while in the circular binary case radiation pressure maintains the cavity circular. In these cases the high binary eccentricity can overcome the effect of radiation pressure suppressing the cavity eccentricity growth, while in the circular binary case radiation pressure maintains the circularity of the cavity. The influence of radiation pressure on binary evolution is subtler. Even if the accretion torque is slightly reduced compared to the only-gas-pressure case (indeed the accretion rates are lower ($\dot{M} \sim 0.01 - 0.1\,\mathrm{M}_\odot/\mathrm{yr}$), consistent with the thinner and colder disc structure [127, 132]), the gravitational torque remains negative, driving the binary to shrink. Eccentricity remains mostly constant, with only minor variations. In the

unequal mass binary case we explored, the radiation pressure contribution mitigates preferential accretion onto the secondary, resulting in a more balanced mass growth between the binary components. In particular, in the gas-pressure-only eccentric $e = 0.45$ and $q = 0.7$ simulation, we find the ratio between secondary and primary black hole to be $\lambda = \dot{M}_2/\dot{M}_1 \sim 2.3$, in agreement with [131]. However, when radiation pressure is included, the accretion is more balanced and $\lambda = 1.18$ and mass ratio growth is effectively suppressed.

We computed the SEDs from the circumbinary discs in our simulations assuming black-body emission. In gas-pressure-only simulations, we find that the luminosity emitted by the innermost regions of the disc (i.e., the mini-discs and the streams) exhibit more variability than the outer parts of the disc. In the circular equal-mass case, the emission peak of the mini-discs and the streams region changes frequency between the optical and UV band ($\log(\nu/\mathrm{Hz}) \sim 14.8 - 15.4$), with the luminosity spanning one order of magnitude. In the circular unequal-mass case, the emission peak of the mini-discs is shifted to slightly lower frequencies — $\log(\nu/\mathrm{Hz}) \sim 14.8 - 15.2$ — and spans up to ~ 2 orders of magnitude in luminosity. In both the eccentric binary cases ($e = 0.9$ and $q = 0.1, 1$), we find that the emission from the mini-discs is completely (in the equal-mass case) or partially (in the unequal-mass case) covered by the streams emission. The X-ray emission, assumed proportional to that of the mini-discs, displays the highest variability, which can reach up to two orders of magnitude for unequal-mass $q = 0.1$ binaries.

We computed the LCs in different frequency bands, mainly focussing on the optical window that will be probed by Rubin Observatory. We calculated the (thermal) flux emitted over the whole EM spectrum that we used to produce the SEDs; that is, within the frequency band $10^8 - 2.8 \times 10^{19}$ Hz ($4.13 \times 10^{-10} - 41.3$ keV), in the optical frequency band using the Rubin Observatory filters, in the near-UV band within $1.0 - 1.5 \times 10^{15}$ Hz ($4.13 - 6.20$ eV), and in the soft X-ray band, in the range of $7.25 - 48.3 \times 10^{16}$ Hz ($0.3 - 2$ keV). In almost all cases, the flux is notably higher in the UV band, while in the soft X-ray is dimmer, consistent with the shape of the SEDs. As the frequency increases, the flux variability grows, in particular in the UV and soft X-ray bands. Here, the flux oscillates by more than an order of magnitude, while in the Rubin Observatory optical bands fluxes vary within a factor of two, in line with the physics of emission from the disc.

Periodic signals can be revealed in the Fourier spectra of the flux and accretion rate, in particular in the circular equal-mass case, where there are clear peaks at $0.2\,f_{\rm K}$ and $0.4\,f_{\rm K}$, associated with the lump periodicity. Moreover, in the LCs, a peak at $2\,f_{\rm K}$ is also present, which corresponds to a periodicity of one half the binary orbital period. In the eccentric equal-mass case, the lump periodicity is significant only in the optical and UV fluxes, while its amplitude is negligible in the soft X-ray band. This is probably due to the larger cavity carved by the binary, which causes the lump region to emit in the optical/UV band rather than in the soft X-ray band. We indeed found the lump modulation peak to be shifted to $f_{\rm K} \sim 0.15$. This is consistent with the fact that the cavity is larger than in the circular equal-mass case since the period associated with its inner edge is $\propto R^{-3/2}$. We note that we found evidence of lump periodicity only in equal-mass binaries. This is consistent with previous works that show the lump modulation amplitude to decrease with binary mass ratio [78]. Therefore, a lack of sub-orbital modulation in the presence of a clear orbital modulation might indicate a small binary mass ratio. We also found a prominent flux and accretion rate modulation over the orbital period of the binary and half of it in all the simulations, with the exception of the circular equal-mass case, which shows a weak periodicity only at $2\,f_{\rm K}$. Flux periodicities are effected by redshift, becoming harder to detect at $z < 0.6$.

We find that radiation pressure plays a crucial role in shaping both the spectral energy distributions and the temporal variability of MBHBs, affecting the electromagnetic signatures of these systems. While the circumbinary disc becomes geometrically thinner, colder and less luminous (the emission peak is shifted towards lower frequencies ($\Delta \log(\nu/\mathrm{Hz}) \sim 0.2 - 0.3$), the mini-discs experience vertical expansion with higher effective temperatures, resulting in a shifted emission toward higher frequencies ($\Delta \log(\nu/\mathrm{Hz}) \sim 0.2 - 0.3$ in circular binaries and $\Delta \log(\nu/\mathrm{Hz}) \sim 0.4 - 0.6$ in eccentric cases) with luminosities increased by $1 - 2$ orders of magnitude with respect to the gas-pressure-only simulations.

The inclusion of radiation pressure also alters the modulations of the flux coming from these systems. We computed the LCs in different frequency bands, with particular attention to the optical window that will be accessible to Rubin Observatory. Consistently with the shift in emission toward higher frequencies, we find that the flux in the optical and near-UV frequency bands is higher with respect to the gas-pressure

only simulations. The amplitude of the variability is also affected: in the optical G band, flux oscillations remain within approximately ≤ 1 order of magnitude, whereas in the near-UV and soft-X ray bands they can vary by up to 2 order of magnitude, comparable to those observed in gas-only simulations.

In contrast to our gas-pressure-only simulations, which show a clear modulation associated to the lump in equal-mass circular and highly eccentric binaries, here this lump-driven modulation is strongly suppressed. In the circular equal-mass case, the FFTs of both the flux and the accretion rate exhibit distinct peaks at $f \sim 0.36\, f_{\rm K}$ and $f \sim 0.72\, f_{\rm K}$, corresponding to emission from the the heated inner edge of the cavity. Indeed, during the accretion onto the binary, some gas is ejected back to the cavity edge, generating shocks that locally heat the gas. Additional peaks are observed in the LCs: the peaks at $f = f_{\rm K}$ and $f = 2f_{\rm K}$ correspond to a periodicity of the binary orbital period and half of it, while the peaks at $f = 1.32, 1.68\, f_{\rm K}$ can be interpreted as linear combinations of the main two fundamental modes. In the eccentric cases, the FFT shows only the periodicities at $f = f_{\rm K}$ and $f = 2f_{\rm K}$.

All the aforementioned considerations are valid when the FFT is computed over a large number of binary orbits (i.e. $300 - 400\, P_{\rm B}$). However, the Rubin Observatory survey is planned to last 10 years and most compact MBHBs are expected to have periods of ≈years. Therefore, to provide a more realistic estimate of the observability of periodic signals in Rubin Observatory data, we have computed the FFT of both the flux and the accretion rate over 5, 10, and 50 binary obits at different redshifts. In the circular equal-mass case, detecting periodicities is challenging, in particular when we consider only five orbits. As expected, the peaks become more distinct and the associated variance, i.e. the statistical error on the mean flux/accretion rate, decreases as the number of orbits increases. Still, the identification of equal-mass, circular binaries appears to be the most challenging. In contrast, binaries with $q = 0.1$ show promising results: clear peaks at $1\, f_{\rm K}$ and $2\, f_{\rm K}$ are detectable even with just five orbits. Similar trends are observed in eccentric cases. The lump periodicity is totally absent in all cases except for the circular equal-mass case, which exhibits a weak hint of lump periodicity when computing the FFT over 50 orbits. Therefore, for unequal-mass binaries with orbital period of approximately 1 year, the chances of detecting it during a 10-year survey are negligible.

The intrinsic faintness of our system, $L_{\rm bol} \approx 10^{42}$ erg s^{-1}, further limits detectability

of periodicities with Rubin Observatory at $z < 0.5$. As an illustrative exercise, we increased the luminosity of all our systems by a factor of 100, mimicking a MBHB of $M = 10^6\,M_\odot$ emitting at the Eddington limit. In this case, periodicities can be identified by Rubin Observatory up to $z \approx 2$, opening the possibility of finding these systems in a large fraction of the co-moving volume of the Universe.

Even when radiation pressure is implemented in the evolution of the systems, identifying periodic signals in circular equal-mass binaries remains challenging, in particular with a handful of orbits. In highly eccentric equal-mass case, radiation pressure suppresses the lump-driven modulation, but variability on the binary orbital period is quite pronounced and the detection of periodicities even with a few orbits is improved with respect to the gas-pressure-only case. In the unequal-mass case, as also reported in the gas-pressure-only simulations, periodicities are easier to detect even at higher redshift $z \sim 1.5$. Due to the relatively low intrisic luminosity of our systems ($L_{\rm bol} \approx 10^{42}\,{\rm erg\,s^{-1}}$), periodic signals would be observable with Rubin Observatory only from systems at redshift $z < 0.7 - 1.0$.

The suppression of lump modulation in equal-mass systems when radiation pressure is included in hydrodynamical simulations reduces the prominence of this feature as a potential EM tracer proposed by previous work. Nevertheless, the periodicity on the binary orbital period timescale remains the most robust and observationally promising signature. This finding highlights the importance of adopting simulations with more realistic physical processes to achieve a more comprehensive model of these systems to more accurately characterise their EM signatures. At the same time, it underscores the importance of developing new statistical approaches to evaluate the detectability of predicted features in real data. Both of these points represent possible ground for future investigation and expand the works presented in this thesis. In particular, we are already working on developing a new statistical model applicable to forthcoming observational data, allowing for a robust and quantitative identification of true periodic signals (F.Cocchiararo et al., in prep.).

Overall, our results suggest that periodicities related to unequal-mass binaries will be easier to identify in Rubin Observatory data, compared to equal-mass ones. Furthermore, LCs from binaries with different properties (equal vs unequal mass, circular vs eccentric) exhibit distinctive modulations, hinting at the possibility of constraining

the binary properties from their time-domain EM data, a prospect that warrants further investigation. Such information can play a pivotal role in informing both current and future low-frequency GW searches with LISA and PTAs at different levels. Working at millihertz frequencies, LISA will detect MBHBs with orbital periods of a few hours, capturing them during their late inspiral and final coalescence phases. In this context, Rubin Observatory could provide a valuable census of LISA precursors, i.e., binaries that will coalesce in the LISA band within the next few million years. Electromagnetic measurements can be used to estimate their mass ratios, eccentricities, and environment to set priors for LISA searches. Combined GW and EM information also offer a powerful testbed for our theoretical understanding of MBHB evolution. For instance, we expect binaries evolving in circumbinary gaseous discs to feature high, aligned spins [172]. Consequently, a hypothetical large population of gas-rich MBHBs detected by Rubin Observatory should correspond to spin-aligned systems detected by LISA. Conversely, at nanohertz frequencies, PTAs can potentially detect MBHBs with orbital periods comparable to those probed by Rubin Observatory. However, systems that can be individually resolved by PTAs, typically have masses $\gtrsim 10^9\, M_\odot$, orders of magnitude larger than those explored in our simulations [173]. If we assume that the trends we found with mass ratio and eccentricities in the EM signatures hold also at much higher masses, then putative multi-messenger observations of PTA sources will allow us to constrain the parameters of the system. In fact, most PTA resolved sources will be monochromatic, meaning that from the GW signal we shall only be able to extract a wave amplitude. The identification of an EM counterpart will first provide a measurement of the distance to the source, allowing one to estimate the source chirp mass from the amplitude. Moreover, distinctive periodicity features might help in constraining the binary mass ratio, allowing one to estimate the individual masses of the two black holes. It is therefore clear that refining our understanding of EM signals from MBHBs might prove extremely fruitful in the era of multi-messenger astronomy.

Acknowledgements

This thesis is the final result of three years of hard work, experiences and opportunities that allowed me to grow both as a researcher and as a person. This journey would not be possible without the advice, aid and encouragement of many people, to whom I am deeply grateful.

At first, I would like to thank my supervisor Alberto Sesana, who has supported and guided me not only during my PhD, but also during my Bachelor and Master thesis. Your passion for astrophysics and your dedication to research have always been a great source of inspiration for me. I also want to thank my co-supervisors, Alessia Franchini and Alessandro Lupi, for being so passionate about their work, for their support and advice at every stage of my PhD.

I thank Maria Charisi and Tamara Bogdanović for carefully reading this manuscript and for providing relevant feedback.

I truly thank all the PhD students and researchers of the Astrophysics group at the University of Milano-Bicocca, with whom I shared my daily life over the past years, from lunches and coffee breaks to aperitivi and D&D sessions. I am grateful to have been part of such a close-knit and supportive group. In particular, I would like to thank my office mates Federica, Francesco and Lorenzo for making every day more enjoyable, fun and lighter. Without you, my PhD experience would not have been the same.

Finally, I wish to thank my parents and my sister Desirèe, whose support was vital in these eventful last three years, and all those who cared about me during the entire journey that led me to this final step.

While I was high school, studying for sociology tests, I dreamed of making my greatest passion the focus of my studies and my work. I am deeply grateful to have had this opportunity.

Ringraziamenti

Questa tesi è il risultato finale di tre anni di duro lavoro, esperienze e opportunità che mi hanno permesso di crescere sia come ricercatrice sia come persona. Questo percorso non sarebbe stato possibile senza i consigli, il supporto e l'incoraggiamento di molte persone, a cui sono profondamente grata.

Innanzitutto, vorrei ringraziare il mio supervisor Alberto Sesana, che mi ha supportata ed aiutata non solo durante il mio dottorato, ma anche durante il mio lavoro di tesi Triennale e Magistrale. La tua passione per l'Astrofisica e la tua dedizione alla ricerca sono sempre state fonte di ispirazione per me. Ringrazio inoltre i miei co-supervisor, Alessia Franchini e Alessandro Lupi, per la passione che mettono nel loro lavoro, per il supporto e i preziosi consigli in ogni fase del mio dottorato.

Ringrazio Maria Charisi e Tamara Bogdanović per aver letto questo manoscrito e aver fornito feedback importanti.

Ringrazio di cuore tutti i dottorandi e ricercatori del gruppo di Astrofisica dell'Università di Milano-Bicocca, con cui ho condiviso la mia quotidianità negli ultimi anni, dai pranzi e pause caffè agli aperitivi e sessioni di D&D. Sono grata di aver fatto parte di un gruppo così coeso e solidale. In particolare, ringrazio i miei compagni d'ufficio, Federica, Francesco e Lorenzo, che hanno reso ogni giorno più piacevole e spensierato. Senza di voi, il mio dottorato non sarebbe stato lo stesso.

Infine, ringrazio i miei genitori e mia sorella Desirèe, il cui supporto è stato fondamentale in questi tre anni intensi, e tutti coloro che si sono presi cura di me lungo l'intero percorso che mi ha condotta a questo traguardo.

Quando ero alle superiori, mentre studiavo per le interrogazioni di sociologia, sognavo di poter fare della mia più grande passione l'oggetto del mio studio e del mio lavoro. Sono profondamente grata di aver avuto questa opportunità.

Bibliography

[1] S.L. Shapiro & S.A. Teukolsky. *Black Holes, White Dwarfs and Neutron Star. The Physics of Compact Object*. Wiley-VCH, 1983.

[2] L. C. Ho J. Kormendy. "Coevolution (Or Not) of Supermassive Black Holes and Host Galaxies". In: *Annual Review of Astronomy and Astrophysics* 51 (2013), pp. 511–623. DOI: 082708-101811.

[3] Onsi Fakhouri, Chung-Pei Ma, and Michael Boylan-Kolchin. "The merger rates and mass assembly histories of dark matter haloes in the two Millennium simulations: Merger rates". In: *Monthly Notices of the Royal Astronomical Society* 406.4 (2010), 2267–2278. ISSN: 0035-8711. DOI: 10.1111/j.1365-2966.2010.16859.x. URL: http://dx.doi.org/10.1111/j.1365-2966.2010.16859.x.

[4] Joseph A O'Leary et al. "<scp>Emerge</scp>: Empirical predictions of galaxy merger rates since z $\sim$ 6". In: *Monthly Notices of the Royal Astronomical Society* (2020). ISSN: 1365-2966. DOI: 10.1093/mnras/staa3746. URL: http://dx.doi.org/10.1093/mnras/staa3746.

[5] M. C. Begelman, R. D. Blandford, and M. J. Rees. "Massive black hole binaries in active galactic nuclei". In: *Nature* 287.5780 (1980), pp. 307–309. DOI: 10.1038/287307a0.

[6] S. Chandrasekhar. "Dynamical Friction. I. General Considerations: the Coefficient of Dynamical Friction." In: *ApJ* 97 (1943), p. 255. DOI: 10.1086/144517.

[7] S. Komossa et al. "Discovery of a Binary Active Galactic Nucleus in the Ultraluminous Infrared Galaxy NGC 6240 Using Chandra". In: *ApJ* 582.1 (2003), pp. L15–L19. DOI: 10.1086/346145. arXiv: astro-ph/0212099 [astro-ph].

[8] Michael Koss et al. "UNDERSTANDING DUAL ACTIVE GALACTIC NUCLEUS ACTIVATION IN THE NEARBY UNIVERSE". In: *The Astrophysical Journal* 746.2 (2012), p. L22. ISSN: 2041-8213. DOI: 10.1088/2041-8205/746/2/l22. URL: http://dx.doi.org/10.1088/2041-8205/746/2/L22.

[9] Yue Shen et al. "BINARY QUASARS AT HIGH REDSHIFT. II. SUB-Mpc CLUSTERING ATz∼ 3-4". In: *The Astrophysical Journal* 719.2 (2010), 1693–1698. ISSN: 1538-4357. DOI: 10.1088/0004-637x/719/2/1693. URL: http://dx.doi.org/10.1088/0004-637X/719/2/1693.

[10] E. P. Farina, R. Falomo, and A. Treves. "A study of six low-redshift quasar pairs: A study of six low redshift QSO pairs". In: *Monthly Notices of the Royal Astronomical Society* 415.4 (2011), 3163–3167. ISSN: 0035-8711. DOI: 10.1111/j.1365-2966.2011.18931.x. URL: http://dx.doi.org/10.1111/j.1365-2966.2011.18931.x.

[11] Pau Amaro-Seoane et al. "Astrophysics with the Laser Interferometer Space Antenna". In: *Living Reviews in Relativity* 26.1, 2 (2023), p. 2. DOI: 10.1007/s41114-022-00041-y. arXiv: 2203.06016 [gr-qc].

[12] Andrés Escala et al. "The Role of Gas in the Merging of Massive Black Holes in Galactic Nuclei. II. Black Hole Merging in a Nuclear Gas Disk". In: *ApJ* 630.1 (2005), pp. 152–166. DOI: 10.1086/431747. arXiv: astro-ph/0406304 [astro-ph].

[13] L. Mayer et al. "Rapid Formation of Supermassive Black Hole Binaries in Galaxy Mergers with Gas". In: *Science* 316.5833 (2007), p. 1874. DOI: 10.1126/science.1141858. arXiv: 0706.1562 [astro-ph].

[14] M. Dotti et al. "Supermassive black hole binaries in gaseous and stellar circumnuclear discs: orbital dynamics and gas accretion". In: *MNRAS* 379.3 (2007), pp. 956–962. DOI: 10.1111/j.1365-2966.2007.12010.x. arXiv: astro-ph/0612505 [astro-ph].

[15] G. Lodato et al. "Black hole mergers: can gas discs solve the 'final parsec' problem?" In: *MNRAS* 398.3 (2009), pp. 1392–1402. DOI: 10.1111/j.1365-2966.2009.15179.x. arXiv: 0906.0737 [astro-ph.CO].

[16] Alberto Sesana, Francesco Haardt, and Piero Madau. "Interaction of Massive Black Hole Binaries with Their Stellar Environment. II. Loss Cone Depletion and Binary Orbital Decay". In: *ApJ* 660.1 (2007), pp. 546–555. DOI: 10.1086/513016. arXiv: astro-ph/0612265 [astro-ph].

[17] Alberto Sesana, Francesco Haardt, and Piero Madau. "Interaction of Massive Black Hole Binaries with Their Stellar Environment. I. Ejection of Hypervelocity Stars". In: *The Astrophysical Journal* 651.1 (2006), 392–400. ISSN: 1538-4357. DOI: 10.1086/507596. URL: http://dx.doi.org/10.1086/507596.

[18] Simone Callegari et al. "Growing Massive Black Hole Pairs in Minor Mergers of Disk Galaxies". In: *Astrophys. J.* 729 (2011), p. 85. DOI: 10.1088/0004-637X/729/2/85. arXiv: 1002.1712 [astro-ph.CO].

[19] Gerald D. Quinlan. "The dynamical evolution of massive black hole binaries I. Hardening in a fixed stellar background". In: *New A* 1.1 (1996), pp. 35–56. DOI: 10.1016/S1384-1076(96)00003-6. arXiv: astro-ph/9601092 [astro-ph].

[20] Alberto Sesana and Fazeel Mahmood Khan. "Scattering experiments meet N-body – I. A practical recipe for the evolution of massive black hole binaries in stellar environments". In: *Monthly Notices of the Royal Astronomical Society: Letters* 454.1 (2015), L66–L70. ISSN: 1745-3925. DOI: 10.1093/mnrasl/slv131. URL: http://dx.doi.org/10.1093/mnrasl/slv131.

[21] Miloš Milosavljević and David Merritt. "Formation of Galactic Nuclei". In: *ApJ* 563.1 (2001), pp. 34–62. DOI: 10.1086/323830. arXiv: astro-ph/0103350 [astro-ph].

[22] F. M. Khan, A. Just, and D. Merritt. "Efficient Merger of Binary Supermassive Black Holes in Merging Galaxies". In: *ApJ* 732, 89 (2011), p. 89. DOI: 10.1088/0004-637X/732/2/89. arXiv: 1103.0272.

[23] Alberto Sesana. "SELF CONSISTENT MODEL FOR THE EVOLUTION OF ECCENTRIC MASSIVE BLACK HOLE BINARIES IN STELLAR ENVIRONMENTS: IMPLICATIONS FOR GRAVITATIONAL WAVE OBSERVATIONS". In: *The Astrophysical Journal* 719.1 (2010), 851–864. ISSN: 1538-4357. DOI: 10.1088/0004-637x/719/1/851. URL: http://dx.doi.org/10.1088/0004-637X/719/1/851.

[24] Alberto Sesana, Alessia Gualandris, and Massimo Dotti. "Massive black hole binary eccentricity in rotating stellar systems". In: *Monthly Notices of the Royal Astronomical Society: Letters* 415.1 (2011), L35–L39. ISSN: 1745-3925. DOI: 10.1111/j.1745-3933.2011.01073.x. URL: http://dx.doi.org/10.1111/j.1745-3933.2011.01073.x.

[25] P. Artymowicz and S. H. Lubow. "Dynamics of binary-disk interaction. 1: Resonances and disk gap sizes". In: *ApJ* 421 (1994), pp. 651–667. DOI: 10.1086/173679.

[26] P. Goldreich and S. Tremaine. "The excitation of density waves at the Lindblad and corotation resonances by an external potential." In: *ApJ* 233 (1979), pp. 857–871. DOI: 10.1086/157448.

[27] D. N. C. Lin and J. Papaloizou. "On the structure of circumbinary accretion disks and the tidal evolution of commensurable satellites." In: *MNRAS* 188 (1979), pp. 191–201. DOI: 10.1093/mnras/188.2.191.

[28] P. Goldreich and S. Tremaine. "Disk-satellite interactions". In: *ApJ* 241 (1980), pp. 425–441. DOI: 10.1086/158356.

[29] Diego J. Muñoz, Ryan Miranda, and Dong Lai. "Hydrodynamics of Circumbinary Accretion: Angular Momentum Transfer and Binary Orbital Evolution". In: *ApJ* 871.1, 84 (2019), p. 84. DOI: 10.3847/1538-4357/aaf867. arXiv: 1810.04676 [astro-ph.HE].

[30] Paul C. Duffell et al. "Circumbinary Disks: Accretion and Torque as a Function of Mass Ratio and Disk Viscosity". In: *ApJ* 901.1, 25 (2020), p. 25. DOI: 10.3847/1538-4357/abab95. arXiv: 1911.05506 [astro-ph.SR].

[31] Christopher Tiede et al. "Gas-driven Inspiral of Binaries in Thin Accretion Disks". In: *ApJ* 900.1, 43 (2020), p. 43. DOI: 10.3847/1538-4357/aba432. arXiv: 2005.09555 [astro-ph.GA].

[32] Magdalena Siwek, Rainer Weinberger, and Lars Hernquist. "Orbital evolution of binaries in circumbinary discs". In: *MNRAS* 522.2 (2023), pp. 2707–2717. DOI: 10.1093/mnras/stad1131. arXiv: 2302.01785 [astro-ph.HE].

[33] R. M. Heath and C. J. Nixon. "On the orbital evolution of binaries with circumbinary discs". In: *A&A* 641, A64 (2020), A64. DOI: 10.1051/0004-6361/202038548. arXiv: 2007.11592 [astro-ph.HE].

[34] Diego J. Muñoz et al. "Circumbinary Accretion from Finite and Infinite Disks". In: *ApJ* 889.2, 114 (2020), p. 114. DOI: 10.3847/1538-4357/ab5d33. arXiv: 1910.04763 [astro-ph.HE].

[35] Alessia Franchini, Alberto Sesana, and Massimo Dotti. "Circumbinary disc self-gravity governing supermassive black hole binary mergers". In: *MNRAS* 507.1 (2021), pp. 1458–1467. DOI: 10.1093/mnras/stab2234. arXiv: 2106.13253 [astro-ph.HE].

[36] Alessia Franchini, Alessandro Lupi, and Alberto Sesana. "Resolving Massive Black Hole Binary Evolution via Adaptive Particle Splitting". In: *ApJ* 929.1, L13 (2022), p. L13. DOI: 10.3847/2041-8213/ac63a2. arXiv: 2201.05619 [astro-ph.HE].

[37] Alessia Franchini et al. "The importance of live binary evolution in numerical simulations of binaries embedded in circumbinary discs". In: *MNRAS* 522.1

(2023), pp. 1569–1574. DOI: 10.1093/mnras/stad1070. arXiv: 2304.03790 [astro-ph.HE].

[38] F. Cocchiararo et al. "Electromagnetic signatures from accreting massive black hole binaries in time domain photometric surveys". In: *A&A* 691, A250 (2024), A250. DOI: 10.1051/0004-6361/202449598. arXiv: 2402.05175 [astro-ph.HE].

[39] P. C. Peters. "Gravitational Radiation and the Motion of Two Point Masses". In: *Physical Review* 136.4B (1964), pp. 1224–1232. DOI: 10.1103/PhysRev.136.B1224.

[40] M. Maggiore. *Gravitational Waves*. Oxford- University Press, 2008.

[41] B. P. Abbott et al. "Observation of Gravitational Waves from a Binary Black Hole Merger". In: *Physical Review Letters* 116.6, 061102 (2016), p. 061102. DOI: 10.1103/PhysRevLett.116.061102. arXiv: 1602.03837 [gr-qc].

[42] B. P. Abbott et al. "GW170817: Observation of Gravitational Waves from a Binary Neutron Star Inspiral". In: *Phys. Rev. Lett.* 119 (16 2017), p. 161101. DOI: 10.1103/PhysRevLett.119.161101. URL: https://link.aps.org/doi/10.1103/PhysRevLett.119.161101.

[43] Monica Colpi and Alberto Sesana. "Gravitational Wave Sources in the Era of Multi-Band Gravitational Wave Astronomy". In: *An Overview of Gravitational Waves*. WORLD SCIENTIFIC, 2017, 43–140. ISBN: 9789813141766. DOI: 10.1142/9789813141766_0002. URL: http://dx.doi.org/10.1142/9789813141766_0002.

[44] Monica Colpi et al. "LISA Definition Study Report". In: *arXiv e-prints*, arXiv:2402.07571 (2024), arXiv:2402.07571. DOI: 10.48550/arXiv.2402.07571. arXiv: 2402.07571 [astro-ph.CO].

[45] A. Sesana et al. "Multimessenger astronomy with pulsar timing and X-ray observations of massive black hole binaries: Multimessenger astronomy with pulsar timing". In: *Monthly Notices of the Royal Astronomical Society* 420.1 (2011), 860–877. ISSN: 0035-8711. DOI: 10.1111/j.1365-2966.2011.20097.x. URL: http://dx.doi.org/10.1111/j.1365-2966.2011.20097.x.

[46] J. Antoniadis et al. "The second data release from the European Pulsar Timing Array III. Search for gravitational wave signals". In: *arXiv e-prints*, arXiv:2306.16214 (2023), arXiv:2306.16214. DOI: 10.48550/arXiv.2306.16214. arXiv: 2306.16214 [astro-ph.HE].

[47] J. Antoniadis et al. “The second data release from the European Pulsar Timing Array I. The dataset and timing analysis”. In: *arXiv e-prints*, arXiv:2306.16224 (2023), arXiv:2306.16224. DOI: 10.48550/arXiv.2306.16224. arXiv: 2306.16224 [astro-ph.HE].

[48] J. Antoniadis et al. “The second data release from the European Pulsar Timing Array II. Customised pulsar noise models for spatially correlated gravitational waves”. In: *arXiv e-prints*, arXiv:2306.16225 (2023), arXiv:2306.16225. DOI: 10.48550/arXiv.2306.16225. arXiv: 2306.16225 [astro-ph.HE].

[49] J. Antoniadis et al. “The second data release from the European Pulsar Timing Array IV. Search for continuous gravitational wave signals”. In: *arXiv e-prints*, arXiv:2306.16226 (2023), arXiv:2306.16226. DOI: 10.48550/arXiv.2306.16226. arXiv: 2306.16226 [astro-ph.HE].

[50] J. Antoniadis et al. “The second data release from the European Pulsar Timing Array: V. Implications for massive black holes, dark matter and the early Universe”. In: *arXiv e-prints*, arXiv:2306.16227 (2023), arXiv:2306.16227. DOI: 10.48550/arXiv.2306.16227. arXiv: 2306.16227 [astro-ph.CO].

[51] Clemente Smarra et al. “The second data release from the European Pulsar Timing Array: VI. Challenging the ultralight dark matter paradigm”. In: *arXiv e-prints*, arXiv:2306.16228 (2023), arXiv:2306.16228. DOI: 10.48550/arXiv.2306.16228. arXiv: 2306.16228 [astro-ph.HE].

[52] Gabriella Agazie et al. “The NANOGrav 15 yr Data Set: Evidence for a Gravitational-wave Background”. In: *ApJ* 951.1, L8 (2023), p. L8. DOI: 10.3847/2041-8213/acdac6. arXiv: 2306.16213 [astro-ph.HE].

[53] Gabriella Agazie et al. “The NANOGrav 15 yr Data Set: Evidence for a Gravitational-wave Background”. In: *ApJ* 951.1, L8 (2023), p. L8. DOI: 10.3847/2041-8213/acdac6. arXiv: 2306.16213 [astro-ph.HE].

[54] Gabriella Agazie et al. “The NANOGrav 15 yr Data Set: Observations and Timing of 68 Millisecond Pulsars”. In: *ApJ* 951.1, L9 (2023), p. L9. DOI: 10.3847/2041-8213/acda9a. arXiv: 2306.16217 [astro-ph.HE].

[55] Gabriella Agazie et al. “The NANOGrav 15 yr Data Set: Detector Characterization and Noise Budget”. In: *ApJ* 951.1, L10 (2023), p. L10. DOI: 10.3847/2041-8213/acda88. arXiv: 2306.16218 [astro-ph.HE].

[56] Adeela Afzal et al. "The NANOGrav 15 yr Data Set: Search for Signals from New Physics". In: *ApJ* 951.1, L11 (2023), p. L11. DOI: 10.3847/2041-8213/acdc91. arXiv: 2306.16219 [astro-ph.HE].

[57] Daniel J. Reardon et al. "Search for an Isotropic Gravitational-wave Background with the Parkes Pulsar Timing Array". In: *ApJ* 951.1, L6 (2023), p. L6. DOI: 10.3847/2041-8213/acdd02. arXiv: 2306.16215 [astro-ph.HE].

[58] Heng Xu et al. "Searching for the Nano-Hertz Stochastic Gravitational Wave Background with the Chinese Pulsar Timing Array Data Release I". In: *Research in Astronomy and Astrophysics* 23.7, 075024 (2023), p. 075024. DOI: 10.1088/1674-4527/acdfa5. arXiv: 2306.16216 [astro-ph.HE].

[59] Kathrin Grunthal et al. "The MeerKAT Pulsar Timing Array: Maps of the gravitational wave sky with the 4.5-yr data release". In: *Monthly Notices of the Royal Astronomical Society* 536.2 (2024), 1501–1517. ISSN: 1365-2966. DOI: 10.1093/mnras/stae2573. URL: http://dx.doi.org/10.1093/mnras/stae2573.

[60] M. Punturo et al. "The Einstein Telescope: a third-generation gravitational wave observatory". In: *Classical and Quantum Gravity* 27.19, 194002 (2010), p. 194002. DOI: 10.1088/0264-9381/27/19/194002.

[61] Matthew Evans et al. *A Horizon Study for Cosmic Explorer: Science, Observatories, and Community*. 2021. arXiv: 2109.09882 [astro-ph.IM]. URL: https://arxiv.org/abs/2109.09882.

[62] Karan Jani et al. *Laser Interferometer Lunar Antenna (LILA): Advancing the U.S. Priorities in Gravitational-wave and Lunar Science*. 2025. arXiv: 2508.11631 [gr-qc]. URL: https://arxiv.org/abs/2508.11631.

[63] Parameswaran Ajith et al. "The Lunar Gravitational-wave Antenna: mission studies and science case". In: *J. Cosmology Astropart. Phys.* 2025.1, 108 (2025), p. 108. DOI: 10.1088/1475-7516/2025/01/108. arXiv: 2404.09181 [gr-qc].

[64] B. D. Farris et al. "Binary Black Hole Accretion from a Circumbinary Disk: Gas Dynamics inside the Central Cavity". In: *ApJ* 783, 134 (2014), p. 134. DOI: 10.1088/0004-637X/783/2/134. arXiv: 1310.0492 [astro-ph.HE].

[65] Dennis B. Bowen et al. "Quasi-periodic Behavior of Mini-disks in Binary Black Holes Approaching Merger". In: *The Astrophysical Journal* 853.1 (2018), p. L17. ISSN: 2041-8213. DOI: 10.3847/2041-8213/aaa756. URL: http://dx.doi.org/10.3847/2041-8213/aaa756.

[66] Stéphane d'Ascoli et al. "Electromagnetic Emission from Supermassive Binary Black Holes Approaching Merger". In: *The Astrophysical Journal* 865.2 (2018), p. 140. ISSN: 1538-4357. DOI: 10.3847/1538-4357/aad8b4. URL: http://dx.doi.org/10.3847/1538-4357/aad8b4.

[67] Constanze Roedig and Alberto Sesana. "Migration of massive black hole binaries in self-gravitating discs: retrograde versus prograde". In: *MNRAS* 439.4 (2014), pp. 3476–3489. DOI: 10.1093/mnras/stu194. arXiv: 1307.6283 [astro-ph.HE].

[68] John Ryan Westernacher-Schneider et al. *Characteristic signatures of accreting binary black holes produced by eccentric minidisks*. 2023. arXiv: 2307.01154 [astro-ph.HE].

[69] P. Artymowicz and S. H. Lubow. "Mass Flow through Gaps in Circumbinary Disks". In: *ApJ* 467 (1996), p. L77. DOI: 10.1086/310200.

[70] Kimitake Hayasaki, Shin Mineshige, and Hiroshi Sudou. "Binary Black Hole Accretion Flows in Merged Galactic Nuclei". In: *Publications of the Astronomical Society of Japan* 59.2 (2007), pp. 427–441. ISSN: 0004-6264. DOI: 10.1093/pasj/59.2.427. eprint: https://academic.oup.com/pasj/article-pdf/59/2/427/18532186/pasj59-0427.pdf. URL: https://doi.org/10.1093/pasj/59.2.427.

[71] Andrew I. MacFadyen and Miloš Milosavljević. "An Eccentric Circumbinary Accretion Disk and the Detection of Binary Massive Black Holes". In: *ApJ* 672.1 (2008), pp. 83–93. DOI: 10.1086/523869. arXiv: astro-ph/0607467 [astro-ph].

[72] C. Roedig et al. "Limiting eccentricity of subparsec massive black hole binaries surrounded by self-gravitating gas discs". In: *MNRAS* 415.4 (2011), pp. 3033–3041. DOI: 10.1111/j.1365-2966.2011.18927.x. arXiv: 1104.3868 [astro-ph.CO].

[73] Ji-Ming Shi et al. "Three-dimensional Magnetohydrodynamic Simulations of Circumbinary Accretion Disks: Disk Structures and Angular Momentum Transport". In: *ApJ* 749.2, 118 (2012), p. 118. DOI: 10.1088/0004-637X/749/2/118. arXiv: 1110.4866 [astro-ph.HE].

[74] John Ryan Westernacher-Schneider et al. "Multiband light curves from eccentric accreting supermassive black hole binaries". In: *Physical Review D* 106.10

(2022). DOI: 10.1103/physrevd.106.103010. URL: https://doi.org/10.1103%2Fphysrevd.106.103010.

[75] J. Cuadra et al. "Massive black hole binary mergers within subparsec scale gas discs". In: *MNRAS* 393.4 (2009), pp. 1423–1432. DOI: 10.1111/j.1365-2966.2008.14147.x. arXiv: 0809.0311 [astro-ph].

[76] Julian H. Krolik. "ESTIMATING THE PROMPT ELECTROMAGNETIC LUMINOSITY OF A BLACK HOLE MERGER". In: *The Astrophysical Journal* 709.2 (2010), 774–779. ISSN: 1538-4357. DOI: 10.1088/0004-637x/709/2/774. URL: http://dx.doi.org/10.1088/0004-637X/709/2/774.

[77] Scott C. Noble et al. "CIRCUMBINARY MAGNETOHYDRODYNAMIC ACCRETION INTO INSPIRALING BINARY BLACK HOLES". In: *The Astrophysical Journal* 755.1 (2012), p. 51. DOI: 10.1088/0004-637X/755/1/51. URL: https://dx.doi.org/10.1088/0004-637X/755/1/51.

[78] Daniel J. D'Orazio, Zoltán Haiman, and Andrew MacFadyen. "Accretion into the central cavity of a circumbinary disc". In: *MNRAS* 436.4 (2013), pp. 2997–3020. DOI: 10.1093/mnras/stt1787. arXiv: 1210.0536 [astro-ph.GA].

[79] Yike Tang, Zoltán Haiman, and Andrew MacFadyen. "The late inspiral of supermassive black hole binaries with circumbinary gas discs in the LISA band". In: *MNRAS* 476.2 (2018), pp. 2249–2257. DOI: 10.1093/mnras/sty423. arXiv: 1801.02266 [astro-ph.HE].

[80] Vishal Tiwari et al. "Radiation Magnetohydrodynamic Simulation of Sub-Eddington Circumbinary Disk around an Equal-mass Massive Black Hole Binary". In: *ApJ* 986.2, 158 (2025), p. 158. DOI: 10.3847/1538-4357/add408. arXiv: 2502.18584 [astro-ph.HE].

[81] Vishal Tiwari et al. *Radiation Magnetohydrodynamic Simulation of sub-Eddington Circumbinary Disk in a 10:1 Massive Black Hole Binary*. 2025. arXiv: 2510.13955 [astro-ph.HE]. URL: https://arxiv.org/abs/2510.13955.

[82] Luke Zoltan Kelley et al. "Massive BH binaries as periodically variable AGN". In: *MNRAS* 485.2 (2019), pp. 1579–1594. DOI: 10.1093/mnras/stz150. arXiv: 1809.02138 [astro-ph.HE].

[83] Daniel J. D'Orazio and Maria Charisi. *Observational Signatures of Supermassive Black Hole Binaries*. 2023. arXiv: 2310.16896 [astro-ph.HE]. URL: https://arxiv.org/abs/2310.16896.

[84] Deniz Soyuer et al. “Searching for gravitational waves via Doppler tracking by future missions to Uranus and Neptune”. English. In: *Monthly Notices of the Royal Astronomical Society* 503.1 (2021), pp. L73–L79. ISSN: 0035-8711. DOI: 10.1093/mnrasl/slab025.

[85] Alberto Sesana et al. “The Gravitational Wave Signal from Massive Black Hole Binaries and Its Contribution to theLISAData Stream”. In: *The Astrophysical Journal* 623.1 (2005), 23–30. ISSN: 1538-4357. DOI: 10.1086/428492. URL: http://dx.doi.org/10.1086/428492.

[86] Pierre Christian and Abraham Loeb. “LISA Detection of Binary Black Holes in the Milky Way Galaxy”. In: *Mon. Not. Roy. Astron. Soc.* 469.1 (2017), pp. 930–937. DOI: 10.1093/mnras/stx910. arXiv: 1701.01736 [astro-ph.HE].

[87] Zoltán Haiman, Bence Kocsis, and Kristen Menou. “THE POPULATION OF VISCOSITY- AND GRAVITATIONAL WAVE-DRIVEN SUPERMASSIVE BLACK HOLE BINARIES AMONG LUMINOUS ACTIVE GALACTIC NUCLEI”. In: *The Astrophysical Journal* 700.2 (2009), 1952–1969. ISSN: 1538-4357. DOI: 10.1088/0004-637x/700/2/1952. URL: http://dx.doi.org/10.1088/0004-637X/700/2/1952.

[88] Daniel J. D’Orazio et al. “A transition in circumbinary accretion discs at a binary mass ratio of 1:25”. In: *MNRAS* 459.3 (2016), pp. 2379–2393. DOI: 10.1093/mnras/stw792. arXiv: 1512.05788 [astro-ph.HE].

[89] Scott C. Noble et al. “Mass-ratio and Magnetic Flux Dependence of Modulated Accretion from Circumbinary Disks”. In: *ApJ* 922.2, 175 (2021), p. 175. DOI: 10.3847/1538-4357/ac2229. arXiv: 2103.12100 [astro-ph.HE].

[90] Maria Charisi et al. “Multimessenger time-domain signatures of supermassive black hole binaries”. In: *MNRAS* 510.4 (2022), pp. 5929–5944. DOI: 10.1093/mnras/stab3713. arXiv: 2110.14661 [astro-ph.HE].

[91] C. M. Gaskell. “Quasars as supermassive binaries”. In: *Liege International Astrophysical Colloquia*. Ed. by Jean-Pierre Swings. Vol. 24. Liege International Astrophysical Colloquia. 1983, pp. 473–477.

[92] Tamara Bogdanović et al. “Modeling of Emission Signatures of Massive Black Hole Binaries. I. Methods”. In: *The Astrophysical Journal Supplement Series* 174.2 (2008), 455–480. ISSN: 1538-4365. DOI: 10.1086/521828. URL: http://dx.doi.org/10.1086/521828.

[93] C. Montuori et al. "Search for sub-parsec massive binary black holes through line diagnosis - II: Observational signatures of sub-pc binary BHs". In: *Monthly Notices of the Royal Astronomical Society* 425.3 (2012), 1633–1639. ISSN: 0035-8711. DOI: 10.1111/j.1365-2966.2012.21530.x. URL: http://dx.doi.org/10.1111/j.1365-2966.2012.21530.x.

[94] Tamara Bogdanović, Michael Eracleous, and Steinn Sigurdsson. "Emission lines as a tool in search for supermassive black hole binaries and recoiling black holes". In: *New Astronomy Reviews* 53.7-10 (2009), pp. 113–120. DOI: 10.1016/j.newar.2009.09.005. URL: https://doi.org/10.1016%2Fj.newar.2009.09.005.

[95] Tamara Bogdanović, Michael Eracleous, and Steinn Sigurdsson. "SDSS J092712.65+294344.0: RECOILING BLACK HOLE OR A SUBPARSEC BINARY CANDIDATE?" In: *The Astrophysical Journal* 697.1 (2009), 288–292. ISSN: 1538-4357. DOI: 10.1088/0004-637x/697/1/288. URL: http://dx.doi.org/10.1088/0004-637X/697/1/288.

[96] M. Dotti et al. "SDSSJ092712.65+294344.0: a candidate massive black hole binary". In: *Monthly Notices of the Royal Astronomical Society: Letters* 398.1 (2009), pp. L73–L77. DOI: 10.1111/j.1745-3933.2009.00714.x. URL: https://doi.org/10.1111%2Fj.1745-3933.2009.00714.x.

[97] Michael Eracleous et al. "A LARGE SYSTEMATIC SEARCH FOR CLOSE SUPERMASSIVE BINARY AND RAPIDLY RECOILING BLACK HOLES". In: *The Astrophysical Journal Supplement Series* 201.2 (2012), p. 23. DOI: 10.1088/0067-0049/201/2/23. URL: https://doi.org/10.1088%2F0067-0049%2F201%2F2%2F23.

[98] M. Charisi et al. "A population of short-period variable quasars from PTF as supermassive black hole binary candidates". In: *MNRAS* 463.2 (2016), pp. 2145–2171. DOI: 10.1093/mnras/stw1838. arXiv: 1604.01020 [astro-ph.GA].

[99] Matthew J. Graham et al. "A possible close supermassive black-hole binary in a quasar with optical periodicity". In: *Nature* 518.7537 (2015), pp. 74–76. DOI: 10.1038/nature14143. arXiv: 1501.01375 [astro-ph.GA].

[100] M. J. Valtonen et al. "A massive binary black-hole system in OJ287 and a test of general relativity". In: *Nature* 452.7189 (2008), pp. 851–853. DOI: 10.1038/nature06896. arXiv: 0809.1280 [astro-ph].

[101] S. N. Zhang et al. "eXTP – enhanced X-ray Timing and Polarimetry Mission". In: *ArXiv e-prints* (2016). arXiv: 1607.08823 [astro-ph.IM].

[102] Fabio Rigamonti et al. "Variability in the supermassive black hole binary candidate SDSS J2320+0024: No evidence of periodic modulation". In: *A&A* (2025). ISSN: 1432-0746. DOI: 10.1051/0004-6361/202555550. URL: http://dx.doi.org/10.1051/0004-6361/202555550.

[103] Maria Charisi et al. *Multi-messenger Analysis of Supermassive Black Hole Binaries: The Joint-likelihood Approach*. 2025. arXiv: 2510.08683 [astro-ph.GA]. URL: https://arxiv.org/abs/2510.08683.

[104] N. I. Shakura and R. A. Sunyaev. "Black holes in binary systems. Observational appearance." In: *A&A* 24 (1973), pp. 337–355.

[105] S. A. Balbus and J. F. Hawley. "A powerful local shear instability in weakly magnetized disks. I - Linear analysis. II - Nonlinear evolution". In: *ApJ* 376 (1991), pp. 214–233. DOI: 10.1086/170270.

[106] B. Paczynski. "Ion viscosity in hot accretion disks." In: *Acta Astron.* 28.3 (1978), pp. 253–274.

[107] G. Lodato and J. E. Pringle. "Warp diffusion in accretion discs: a numerical investigation". In: *MNRAS* 381 (2007), pp. 1287–1300. DOI: 10.1111/j.1365-2966.2007.12332.x. arXiv: 0708.1124.

[108] A. Toomre. "On the gravitational stability of a disk of stars." In: *ApJ* 139 (1964), pp. 1217–1238. DOI: 10.1086/147861.

[109] C. F. Gammie. "Nonlinear Outcome of Gravitational Instability in Cooling, Gaseous Disks". In: *ApJ* 553 (2001), pp. 174–183. DOI: 10.1086/320631. eprint: astro-ph/0101501.

[110] G. Lodato and W. K. M. Rice. "Testing the locality of transport in self-gravitating accretion discs - II. The massive disc case". In: *MNRAS* 358.4 (2005), pp. 1489–1500. DOI: 10.1111/j.1365-2966.2005.08875.x. arXiv: astro-ph/0501638 [astro-ph].

[111] J. E. Pringle. "Accretion discs in astrophysics". In: *ARA&A* 19 (1981), pp. 137–162. DOI: 10.1146/annurev.aa.19.090181.001033.

[112] In: *La Rivista del Nuovo Cimento* Online First (2007), 293–99999. ISSN: 0393697X, 0393697X. DOI: 10.1393/ncr/i2007-10022-x. URL: https://doi.org/10.1393/ncr/i2007-10022-x.

[113] George B. Rybicki and Alan P. Lightman. *Radiative processes in astrophysics*. 1979.

[114] Fred C. Adams, Charles J. Lada, and Frank H. Shu. "The Disks of T Tauri Stars with Flat Infrared Spectra". In: *ApJ* 326 (1988), p. 865. DOI: 10.1086/166144.

[115] David W. Hogg. *Distance measures in cosmology*. 2000. arXiv: astro-ph/9905116 [astro-ph].

[116] David W. Hogg et al. *The K correction*. 2002. arXiv: astro-ph/0210394 [astro-ph].

[117] Brandon C. Kelly, Jill Bechtold, and Aneta Siemiginowska. "Are the Variations in Quasar Optical Flux Driven by Thermal Fluctuations?" In: *ApJ* 698.1 (2009), pp. 895–910. DOI: 10.1088/0004-637X/698/1/895. arXiv: 0903.5315 [astro-ph.CO].

[118] S. Vaughan et al. "False periodicities in quasar time-domain surveys". In: *MNRAS* 461.3 (2016), pp. 3145–3152. DOI: 10.1093/mnras/stw1412. arXiv: 1606.02620 [astro-ph.IM].

[119] F. Duras et al. "Universal bolometric corrections for active galactic nuclei over seven luminosity decades". In: *A&A* 636, A73 (2020), A73. DOI: 10.1051/0004-6361/201936817. arXiv: 2001.09984 [astro-ph.GA].

[120] John A. Regan et al. "Super-Eddington accretion and feedback from the first massive seed black holes". In: *MNRAS* 486.3 (2019), pp. 3892–3906. DOI: 10.1093/mnras/stz1045. arXiv: 1811.04953 [astro-ph.GA].

[121] Paul C. Duffell et al. "The Santa Barbara Binary-disk Code Comparison". In: *ApJ* 970.2, 156 (2024), p. 156. DOI: 10.3847/1538-4357/ad5a7e. arXiv: 2402.13039 [astro-ph.SR].

[122] Volker Springel. "Smoothed Particle Hydrodynamics in Astrophysics". In: *ARA&A* 48 (2010), pp. 391–430. DOI: 10.1146/annurev-astro-081309-130914. arXiv: 1109.2219 [astro-ph.CO].

[123] Philip F. Hopkins. "A new class of accurate, mesh-free hydrodynamic simulation methods". In: *Monthly Notices of the Royal Astronomical Society* 450.1 (2015), 53–110. ISSN: 1365-2966. DOI: 10.1093/mnras/stv195. URL: http://dx.doi.org/10.1093/mnras/stv195.

[124] L. B. Lucy. "A numerical approach to the testing of the fission hypothesis." In: *AJ* 82 (1977), pp. 1013–1024. DOI: 10.1086/112164.

[125] R. A. Gingold and J. J. Monaghan. "Smoothed particle hydrodynamics: theory and application to non-spherical stars." In: *MNRAS* 181 (1977), pp. 375–389. DOI: 10.1093/mnras/181.3.375.

[126] Paul C. Duffell and Andrew I. MacFadyen. "TESS: A RELATIVISTIC HYDRODYNAMICS CODE ON A MOVING VORONOI MESH". In: *The Astrophysical Journal Supplement Series* 197.2 (2011), p. 15. ISSN: 1538-4365. DOI: 10.1088/0067-0049/197/2/15. URL: http://dx.doi.org/10.1088/0067-0049/197/2/15.

[127] Enrico Ragusa, Giuseppe Lodato, and Daniel J. Price. "Suppression of the accretion rate in thin discs around binary black holes". In: *MNRAS* 460.2 (2016), pp. 1243–1253. DOI: 10.1093/mnras/stw1081. arXiv: 1605.01730 [astro-ph.HE].

[128] Ryan Miranda, Diego J. Muñoz, and Dong Lai. "Viscous hydrodynamics simulations of circumbinary accretion discs: variability, quasi-steady state and angular momentum transfer". In: *MNRAS* 466.1 (2017), pp. 1170–1191. DOI: 10.1093/mnras/stw3189. arXiv: 1610.07263 [astro-ph.SR].

[129] Alexander J. Dittmann and Geoffrey Ryan. "Preventing Anomalous Torques in Circumbinary Accretion Simulations". In: *ApJ* 921.1, 71 (2021), p. 71. DOI: 10.3847/1538-4357/ac1bbd. arXiv: 2102.05684 [astro-ph.HE].

[130] Alexander J. Dittmann, Geoffrey Ryan, and M. Coleman Miller. "The Decoupling of Binaries from Their Circumbinary Disks". In: *arXiv e-prints*, arXiv:2303.16204 (2023), arXiv:2303.16204. DOI: 10.48550/arXiv.2303.16204. arXiv: 2303.16204 [astro-ph.HE].

[131] Magdalena Siwek et al. "Preferential Accretion and Circumbinary Disk Precession in Eccentric Binary Systems". In: *arXiv e-prints*, arXiv:2203.02514 (2022), arXiv:2203.02514. arXiv: 2203.02514 [astro-ph.HE].

[132] Christopher Tiede et al. "Suppressed Accretion onto Massive Black Hole Binaries Surrounded by Thin Disks". In: *The Astrophysical Journal* 984.2 (2025), p. 144. ISSN: 1538-4357. DOI: 10.3847/1538-4357/adc727. URL: http://dx.doi.org/10.3847/1538-4357/adc727.

[133] M. R. Bate, I. A. Bonnell, and N. M. Price. "Modelling accretion in protobinary systems". In: *MNRAS* 277 (1995), pp. 362–376. DOI: 10.1093/mnras/277.2.362. eprint: astro-ph/9510149.

[134] C. J. Nixon, A. R. King, and J. E. Pringle. "The final parsec problem: aligning a binary with an external accretion disc". In: *MNRAS* 417 (2011), pp. L66–L69. DOI: 10.1111/j.1745-3933.2011.01121.x. arXiv: 1107.5056.

[135] Enrico Ragusa et al. "The evolution of large cavities and disc eccentricity in circumbinary discs". In: *MNRAS* 499.3 (2020), pp. 3362–3380. DOI: 10.1093/mnras/staa2954. arXiv: 2009.10738 [astro-ph.EP].

[136] Mackenzie S. L. Moody, Ji-Ming Shi, and James M. Stone. "Hydrodynamic Torques in Circumbinary Accretion Disks". In: *ApJ* 875.1, 66 (2019), p. 66. DOI: 10.3847/1538-4357/ab09ee. arXiv: 1903.00008 [astro-ph.HE].

[137] C. Roedig et al. "Evolution of binary black holes in self gravitating discs. Dissecting the torques". In: *A&A* 545, A127 (2012), A127. DOI: 10.1051/0004-6361/201219986. arXiv: 1202.6063 [astro-ph.CO].

[138] Aleksander Sądowski. "Thin accretion discs are stabilized by a strong magnetic field". In: *Monthly Notices of the Royal Astronomical Society* 459.4 (2016), 4397–4407. ISSN: 1365-2966. DOI: 10.1093/mnras/stw913. URL: http://dx.doi.org/10.1093/mnras/stw913.

[139] B. Mishra et al. "Three-dimensional, global, radiative GRMHD simulations of a thermally unstable disc". In: *Monthly Notices of the Royal Astronomical Society* 463.4 (2016), 3437–3448. ISSN: 1365-2966. DOI: 10.1093/mnras/stw2245. URL: http://dx.doi.org/10.1093/mnras/stw2245.

[140] Federico Cattorini and Bruno Giacomazzo. "GRMHD study of accreting massive black hole binaries in astrophysical environment: A review". In: *Astroparticle Physics* 154 (2024), p. 102892. ISSN: 0927-6505. DOI: 10.1016/j.astropartphys.2023.102892. URL: http://dx.doi.org/10.1016/j.astropartphys.2023.102892.

[141] Alessia Franchini et al. "Emission signatures from sub-parsec post-Newtonian binaries embedded in circumbinary discs". In: *A&A* 686, A288 (2024), A288. DOI: 10.1051/0004-6361/202449206. arXiv: 2401.10331 [astro-ph.HE].

[142] Philip J. Armitage and Priyamvada Natarajan. "Accretion during the Merger of Supermassive Black Holes". In: *ApJ* 567.1 (2002), pp. L9–L12. DOI: 10.1086/339770. arXiv: astro-ph/0201318 [astro-ph].

[143] P. Artymowicz et al. "The Effect of an External Disk on the Orbital Elements of a Central Binary". In: *ApJ* 370 (1991), p. L35. DOI: 10.1086/185971.

[144] Jonathan Zrake et al. "Equilibrium Eccentricity of Accreting Binaries". In: *ApJ* 909.1, L13 (2021), p. L13. DOI: 10.3847/2041-8213/abdd1c. arXiv: 2010.09707 [astro-ph.HE].

[145] Daniel J. D'Orazio and Paul C. Duffell. "Orbital Evolution of Equal-mass Eccentric Binaries due to a Gas Disk: Eccentric Inspirals and Circular Outspirals". In: *The Astrophysical Journal Letters* 914.1 (2021), p. L21. ISSN: 2041-8213. DOI: 10.3847/2041-8213/ac0621. URL: http://dx.doi.org/10.3847/2041-8213/ac0621.

[146] Takamitsu Tanaka, Rosalba Perna, and Zoltán. Haiman. "X-ray emission from high-redshift miniquasars: self-regulating the population of massive black holes through global warming". In: *MNRAS* 425.4 (2012), pp. 2974–2987. DOI: 10.1111/j.1365-2966.2012.21539.x. arXiv: 1205.6467 [astro-ph.CO].

[147] Stéphane d'Ascoli et al. "Electromagnetic Emission from Supermassive Binary Black Holes Approaching Merger". In: *ApJ* 865.2, 140 (2018), p. 140. DOI: 10.3847/1538-4357/aad8b4. arXiv: 1806.05697 [astro-ph.HE].

[148] Eduardo M. Gutiérrez et al. "Electromagnetic Signatures from Supermassive Binary Black Holes Approaching Merger". In: *The Astrophysical Journal* 928.2 (2022), p. 137. ISSN: 1538-4357. DOI: 10.3847/1538-4357/ac56de. URL: http://dx.doi.org/10.3847/1538-4357/ac56de.

[149] Luciano Combi et al. "Minidisk Accretion onto Spinning Black Hole Binaries: Quasi-periodicities and Outflows". In: *ApJ* 928.2, 187 (2022), p. 187. DOI: 10.3847/1538-4357/ac532a. arXiv: 2109.01307 [astro-ph.HE].

[150] Luke Major Krauth et al. "Disappearing thermal X-ray emission as a telltale signature of merging massive black hole binaries". In: *arXiv e-prints*, arXiv:2304.02575 (2023), arXiv:2304.02575. DOI: 10.48550/arXiv.2304.02575. arXiv: 2304.02575 [astro-ph.HE].

[151] Alessia Franchini et al. "The behaviour of eccentric sub-pc massive black hole binaries embedded in massive discs". In: *A&A* 688, A174 (2024), A174. DOI: 10.1051/0004-6361/202449402. arXiv: 2402.00938 [astro-ph.HE].

[152] D. J. Price et al. *PHANTOM: Smoothed particle hydrodynamics and magnetohydrodynamics code*. Astrophysics Source Code Library. 2017. ascl: 1709.002.

[153] S. A. Balbus and J. F. Hawley. "A powerful local shear instability in weakly magnetized disks. I - Linear analysis. II - Nonlinear evolution". In: *ApJ* 376 (1991), pp. 214–233. DOI: 10.1086/170270.

[154] G. Lodato and W. K. M. Rice. "Testing the locality of transport in self-gravitating accretion discs". In: *MNRAS* 351 (2004), pp. 630–642. DOI: 10.1111/j.1365-2966.2004.07811.x. eprint: astro-ph/0403185.

[155] G. Lodato. "Self-gravitating accretion discs". In: *Nuovo Cimento Rivista Serie* 30 (2007). DOI: 10.1393/ncr/i2007-10022-x. arXiv: 0801.3848.

[156] LSST Science Collaboration et al. "LSST Science Book, Version 2.0". In: *arXiv e-prints*, arXiv:0912.0201 (2009), arXiv:0912.0201. arXiv: 0912.0201 [astro-ph.IM].

[157] Rudolf Kippenhahn and Alfred Weigert. *Stellar Structure and Evolution*. 1990.

[158] Y. Shvartzvald et al. "ULTRASAT: A Wide-field Time-domain UV Space Telescope". In: *ApJ* 964.1, 74 (2024), p. 74. DOI: 10.3847/1538-4357/ad2704. arXiv: 2304.14482 [astro-ph.IM].

[159] S. R. Kulkarni et al. *Science with the Ultraviolet Explorer (UVEX)*. 2023. arXiv: 2111.15608 [astro-ph.GA].

[160] Juhan Frank, Andrew King, and Derek J. Raine. *Accretion Power in Astrophysics: Third Edition*. 2002.

[161] Yan-Fei Jiang et al. "Global Radiation Magnetohydrodynamic Simulations of sub-Eddington Accretion Disks around Supermassive Black Holes". In: *ApJ* 885.2, 144 (2019), p. 144. DOI: 10.3847/1538-4357/ab4a00. arXiv: 1904.01674 [astro-ph.HE].

[162] Jiahui Huang et al. "Global 3D Radiation Magnetohydrodynamic Simulations of Accretion onto a Stellar-mass Black Hole at Sub- and Near-critical Accretion Rates". In: *The Astrophysical Journal* 945.1 (2023), p. 57. ISSN: 1538-4357. DOI: 10.3847/1538-4357/acb6fc. URL: http://dx.doi.org/10.3847/1538-4357/acb6fc.

[163] Lizhong Zhang et al. *Radiation GRMHD Models of Accretion onto Stellar-Mass Black Holes: I. Survey of Eddington Ratios*. 2025. arXiv: 2506.02289 [astro-ph.HE]. URL: https://arxiv.org/abs/2506.02289.

[164] H. Shiokawa et al. "General Relativistic Hydrodynamic Simulation of Accretion Flow from a Stellar Tidal Disruption". In: *ApJ* 804, 85 (2015), p. 85. DOI: 10.1088/0004-637X/804/2/85. arXiv: 1501.04365 [astro-ph.HE].

[165] Taeho Ryu, Julian Krolik, and Tsvi Piran. "Extremely Relativistic Tidal Disruption Events". In: *The Astrophysical Journal Letters* 946.2 (2023), p. L33.

ISSN: 2041-8213. DOI: 10.3847/2041-8213/acc390. URL: http://dx.doi.org/10.3847/2041-8213/acc390.

[166] A. C. Dunhill, J. Cuadra, and C. Dougados. "Precession and accretion in circumbinary discs: the case of HD 104237". In: *MNRAS* 448.4 (2015), pp. 3545–3554. DOI: 10.1093/mnras/stv284. arXiv: 1411.0687 [astro-ph.SR].

[167] Chengcheng Xin and Zoltan Haiman. *Identifying the electromagnetic counterparts of LISA massive black hole binaries in archival LSST data*. 2024. arXiv: 2403.18751 [astro-ph.HE]. URL: https://arxiv.org/abs/2403.18751.

[168] Chengcheng Xin et al. *Identifying Compact Chirping SMBHBs in LSST using Bayesian Analysis*. 2025. arXiv: 2506.10846 [astro-ph.HE]. URL: https://arxiv.org/abs/2506.10846.

[169] A. Sądowski et al. "Spinning up black holes with super-critical accretion flows". In: *A&A* 532, A41 (2011), A41. DOI: 10.1051/0004-6361/201116702. arXiv: 1102.2456 [astro-ph.HE].

[170] Fabiola Cocchiararo et al. "Radiation pressure role in accreting massive black hole binaries". In: (2025). arXiv: 2508.18349 [astro-ph.HE]. URL: https://arxiv.org/abs/2508.18349.

[171] Alfredo Chiesa et al. "Identifying massive black hole binaries via light curve variability in optical time-domain surveys". In: (2025). arXiv: 2508.21510 [astro-ph.HE]. URL: https://arxiv.org/abs/2508.21510.

[172] M. Dotti et al. "Dual black holes in merger remnants - II. Spin evolution and gravitational recoil". In: *MNRAS* 402.1 (2010), pp. 682–690. DOI: 10.1111/j.1365-2966.2009.15922.x. arXiv: 0910.5729 [astro-ph.HE].

[173] Pablo A. Rosado, Alberto Sesana, and Jonathan Gair. "Expected properties of the first gravitational wave signal detected with pulsar timing arrays". In: *MNRAS* 451.3 (2015), pp. 2417–2433. DOI: 10.1093/mnras/stv1098. arXiv: 1503.04803 [astro-ph.HE].